2D Material Enabled Nonlinear Integrated Photonics

Taylor Fryett

A dissertation
submitted in partial fulfillment of the
requirements for the degree of

Doctor of Philosophy

University of Washington

2019

Reading Committee:

Arka Majumdar, Chair

Lih Lin

Xiaodong Xu

Program Authorized to Offer Degree:
Electrical and Computer Engineering

University of Washington

Abstract

2D Material Enabled Nonlinear Integrated Photonics

Taylor Fryett

Chair of the Supervisory Committee:
Assistant Professor Arka Majumdar
Department of Electrical and Computer Engineering, Physics

The family of 2D materials has been the topic of intense academic study due to the tight out-of-plane electronic confinement that gives rise to pronounced electronic and optical effects. Many of the effects that have made them popular among the material science and physics communities also makes them appealing in an integrated photonics settings where their strong optical and opto-electronic effects may give rise to transformative devices. This dissertation aims to outline the work I have conducted to illustrate the capacity of monolayer transition metal dichalcogenides (TMDs) for nonlinear integrated photonic devices.

I will present work that explores the efficacy of TMDs for nonlinear photonics based on the second-order susceptibility nonlinearity, specifically second-harmonic generation (SHG) devices. A select few of the major contributions to the field of integrated SHG are outlined. These works are then used to frame a theoretic study of TMD based SHG devices, where we predict that patterning the materials will allow for SHG devices with relaxed fabrication tolerances. This is followed by a review of experimental demonstration of cavity enhanced SHG with a silicon micro-resonator and the current progress towards demonstrating the same with silicon nitride micro-resonators.

TABLE OF CONTENTS

LIST OF FIGURES

GLOSSARY

AFM: Atomic force microscopy.

BOX: Buried oxide layer.

CVD: Chemical vapor deposition.

DBR: Distributed Bragg reflector.

DCM: Dichloromethane.

DFG: Difference frequency generation.

FDTD: Finite-difference time-domain.

FSR: Free spectral range

HF: Hydroflouric acid.

ICP: Inductively coupled plasma.

LPCVD: Low pressure chemical vapor deposition.

MX_2: Transition metal dichalcogenide (as referred to by chemical composition).

NIR: Near infrared.

NLO: Nonlinear optics.

OPA: Optical parametric oscillator.

PC: Polycarbonate.

PDMS: Polydimethylsiloxane.

PHC: Photonic crystal.

PHCC: Photonic crystal cavity.

PL: Photoluminescence.

PMMA: Poly(methyl methacrylate).

PVA: Polyvinyl alcohol.

SEM: Scanning electron microscope.

SFG: Sum frequency generation.

SHG: Second-harmonic generation.

SOI: Silicon on insulator.

TMD: Transition metal dichalcogenide.

TPA: Two photon absorption.

QPM: Quasi-phase matched.

WNF: Washington nanofabrication facility.

ACKNOWLEDGMENTS

I would like to thank my advisor, Professor Arka Majumdar, for his patients and guidance. I gratefully acknowledge support from my other committee members, Professors Xiaodong Xu, Kai-Mei Fu, Lih Lin, and Igor Novosselov. To my lab mates with whom I have had many fruitful conversations. Lastly to my family and friends for their support, especially my wife.

DEDICATION

For my dear wife, Cori.

Chapter 1
INTRODUCTION

Integrated photonics started with humble beginnings in the late 1980's with the pioneering work of Soref and Larenzo who first demonstrated on chip waveguiding using silicon [104]. Since then the field has greatly expanded in order to address the rising needs in the telecommunications and data communications sectors. Here, silicon photonics has already established itself as a key technology with recent demonstrations of transcievers reaching the 100 GB/s mark [24]. The resulting increase in accessibility of silicon photonics has led to new and exciting applications outside traditional telecommunications motivations, including biomedical [40] LIDAR [86] applications, and is expected to extend into other application domains. The needs of the current applications are well met by state-of-the-art passive components, and key opto-electronic devices such as lasers, detectors, and modulators. However, future applications may critically depend on another type of integrated photonic device, optically nonlinear devices. While a host of functionality can arise from optical nonlinearities, this dissertation focuses on the frequency conversion that arises from the second order susceptibility nonlinearity ($\chi^{(2)}$), specifically the frequency doubling of photons.

1.1 Motivation for Second-Order Integrated Nonlinear Optics

The frequency conversion capabilities of the $\chi^{(2)}$ nonlinearity has been a subject of intense academic research since the first experimental demonstration of frequency doubling in 1961 [28]. Interest in this phenomenon goes well beyond the desire to understand the physical underpinnings of such frequency conversion, and is largely motivated by the ability to extend light generation to frequencies where there are no suitable emitters. For instance, frequency doubling, also know as second harmonic generation (SHG), is routinely used to generate

532 nm light from frequency doubling the 1064 nm laser light emitted by neodymium-doped yttrium aluminum garnet (Nd:YAG) lasers. $\chi^{(2)}$ based frequency conversion is also the underpinning of optical parametric amplifiers which are frequently used in scientific settings where frequency tunability is of utmost importance.

In the context of integrated photonics there are two primary driving forces behind exploring the $\chi^{(2)}$ based frequency conversion. The first is the exact analog of the classical case mentioned previously, and thus generating new wavelengths might be of importance to future biomedical applications, or other application areas. The other is for use in quantum information science and technology. One of the key components of any quantum information system is the quantum memory. There are several promising candidates such as the negatively charged nitrogen-vacancy center in diamond [25] and the newly reported defects in silicon carbide [67]. However, many of these emitters lay far from the telecommunication bands (~1550 nm) [33]. Being able to efficiently frequency convert these photons to the telecommunications bands will greatly reduce the overall losses, and opens up the possibility of exploiting existing telecommunication infrastructures.

1.2 Background of Second-Order Nonlinear Optics

In general the polarization field can be expressed as a power series of the electric field with coefficients given by specific material properties. Specifically, the polarization field can be written as $P = \epsilon_0 \sum_{n=1}^{\infty} \chi^{(n)} E^n$ [39], where ϵ_0 is the permittivity of free space, $\chi^{(n)}$ is the n^{th} order electric susceptibility, and E^n is the electric field taken to the n^{th} power. The first term in the series is the term most commonly referred to as the polarization field. The higher order terms are frequently neglected, as their effects only become prominent at high intensities. When the first-order term is no longer sufficient, one usually incorporates the next nonzero term. This first order correction depends on the crystal symmetries of the nonlinear material. If the material is non-centrosymmetric then the second order term ($\chi^{(2)}$) is the first nonzero term, otherwise it is the third ($\chi^{(3)}$) term [15]. All higher order terms are typically referred to as higher order harmonics and only play a significant role under fields

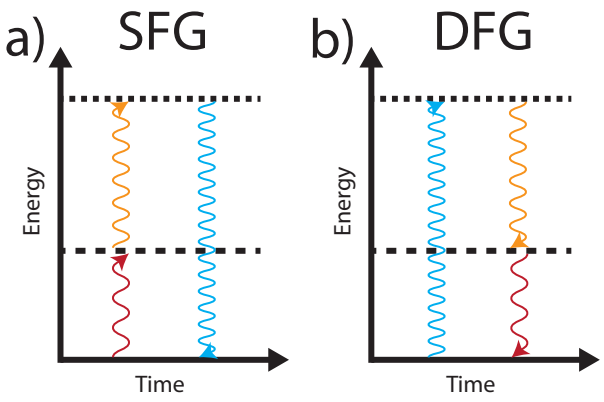

Figure 1.1: A simplistic view of second harmonic frequency (SHG), and difference frequency generation (DFG). The colored wavy lines correspond to individual photons interacting with a $\chi^{(2)}$ material. The zero energy state corresponds to the valence band, while the dashed lines correspond to the virtual states utilized in $\chi^{(2)}$ processes. (a) The SFG process involves two incoming photons (red and orange) that collectively excite an electron into a virtual state from which a photon with the sum of their energies emits (blue). (b) Same as (a), but with reversed roles for the photons.

far more intense than required to observe effects from the $\chi^{(2)}$ or $\chi^{(3)}$ nonlinearities. These higher order terms are typically only explored for the purpose of generating high energy photons.

Before proceeding it is important to have a clear physical and mathematical picture of $\chi^{(2)}$ processes. $\chi^{(2)}$ processes are often referred to as "three wave mixing" as each $\chi^{(2)}$ process involves three photons and a number of virtual states as shown in Figure 1.1, which illustrates the two generalized cases of three wave mixing. For instance, sum frequency generation (SFG), as shown in Fig. 1.1a, shows two incident photons, each successively exciting a photon from the ground state into virtual states. After a short delay the electron decays back into the ground state. Subfigure b shows a similar process, difference frequency generation (DFG), which is the same process in reverse.

We can understand the mathematical picture of $\chi^{(2)}$ frequency generation by studying Maxwell's equations in matter. The portion of polarization field arising from the second

order term can be written as [15]:

$$P_i(\omega_3) = \sum_j \sum_k \chi^{(2)}_{ijk}(\omega_3, \omega_2, \omega_1) E_j(\omega_2) E_k(\omega_1) \tag{1.1}$$

Here we take the subscripts to indicate the component (e.g. x, y, or z) of each field. P_i is the resulting polarization field, $\chi^{(2)}_{ijk}$ is the $\chi^{(2)}$ tensor for the crystal of interest, and E represents the electric field. The $\chi^{(2)}$ tensor dictates which combination of polarizations are mediated in a second-order process. A typical exercise in introductory electromagnetics courses is to start with Maxwell's equations, then derive the wave equation for the electric field:

$$\nabla^2 E = \frac{1}{c^2} \frac{\partial^2 E}{\partial t^2} \tag{1.2}$$

However, if one starts with Maxwell's equations in matter we can arrive at another wave equation:

$$\nabla^2 E = \frac{1}{\epsilon_0 c^2} \frac{\partial^2 D}{\partial t^2} \tag{1.3}$$

where $D = \epsilon_0 E + P$. If we split the polarization fields and displacement fields into their linear and nonlinear components, $P = P^{(1)} + P^{(NL)}$ and $D = \epsilon_0 E + P^{(1)}$, we can write the wave equation in matter as:

$$\nabla^2 E - \frac{1}{\epsilon_0 c^2} \frac{\partial^2 D^{(1)}}{\partial t^2} = \frac{1}{\epsilon_0 c^2} \frac{\partial^2 P^{(NL)}}{\partial t^2} \tag{1.4}$$

Now we can clearly see that the nonlinear polarization terms serve as a source term in the classic wave equation. This provides some insight on the new frequency generation via the polarization nonlinearities.

1.2.1 Implications of Conservation Laws for Second-Order Nonlinear Optics

The crux of working with $\chi^{(2)}$ processes is the need to satisfy both the frequency and phase matching conditions. The first is readily understood as a consequence of the conservation of

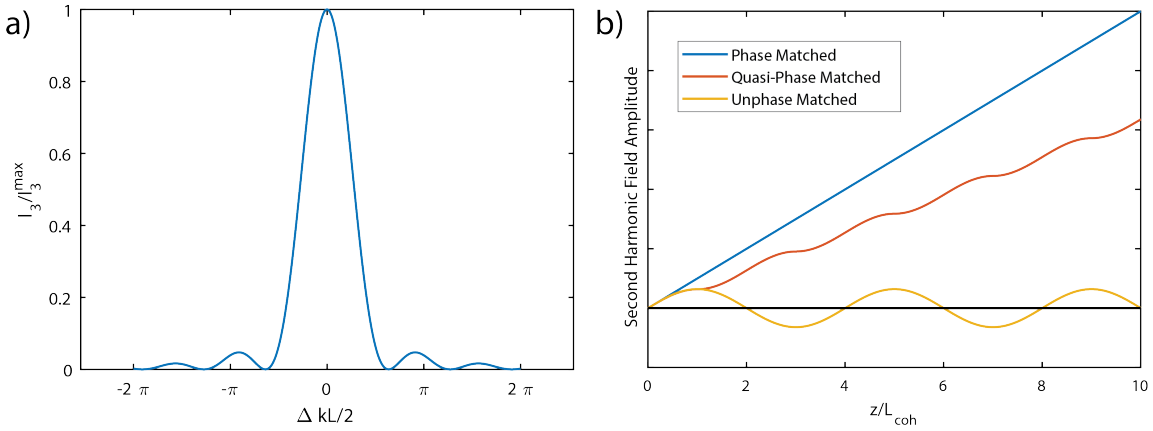

Figure 1.2: Characteristics of phase matching. (a) The percent of maximum efficiency for a SFG process as a function of momentum mismatch and propagation length. Of note is the case where phase matching ($\Delta k = 0$) occurs which corresponds to maximal conversion. (b) Generation of SHG field as a function of propagation distance for the three general cases of phase matching. Without phase matching (yellow trace) the power oscillates back between the harmonic and fundamental wave every coherence length. With perfect phase matching (blue trace) the harmonic field grows linearly with the propagation length. Finally, for quasi-phase matching (red trace) the harmonic wave grows monotonically, albeit sub-linearly.

energy. Explicitly, the frequency matching condition is $\omega_1 + \omega_2 = \omega_3$ for a SFG process. It is easy to see how one can arrive at $\hbar\omega_1 + \hbar\omega_2 = \hbar\omega_3$, which is the explicit equation of energy conservation for this process.

The phase matching condition, a consequence of momentum matching, requires a more lengthy derivation. Consider two propagating plane waves in a $\chi^{(2)}$ medium with wave vectors k_1 and k_2 that are participating in a sum frequency interaction to produce a plane wave with wave vector k_3. By applying Maxwell's equations, we can derive an expression for the intensity of the third wave:

$$I_3 = I_3^{max}\Big[\frac{sin(\Delta kL/2)}{\Delta kL/2}\Big]^2 \tag{1.5}$$

where $\Delta k = k_1 + k_2 - k_3$, I_3 is the intensity of the generated wave, and L is the propagation length. The phase matching condition is given by $\Delta k = 0$ and guarantees I_3 remains at its maximal value.

The phase-matching condition is one of the most difficult conditions of second-order nonlinear optics to satisfy. To obtain phase-matching, one must take great care to make the refractive index the precise values required for the process. For second harmonic generation the problem simplifies to making the refractive index the same at the fundamental and second harmonic frequencies. However, even this is difficult due to dispersion, which tends to force the refractive index at the second harmonic frequency to be higher than that at the fundamental frequency. In bulk crystals this is frequently compensated for by birefringent effects [15, 124]. Even then, ovens are usually employed to carefully control the temperature to ensure the phase matching condition not derailed by temperature fluctuations.

One problem that often arises is the inability for a crystal to satisfy the phase-matching condition. This can happen if the dispersion within the spectral window of interest is too large compared to the birefringent effects within the crystal. In such a case, the power will simply be cyclically exchanged between the fundamental and harmonic modes. Half the length scale over which this usually occurs is called the coherence length defined as:

$$L_{coh} = \frac{\pi}{\Delta k} \tag{1.6}$$

It was realized that one could achieve grater second-order effects in crystals that lack phase-matching if the crystal axis could be flipped after every coherence length [6]. In this way as power from the generated wave began to cycle back into the pump waves the crystal orientation would flip and power would again flow into the generated wave. This technique has become known as quasi-phase-matching (QPM), and has been widely employed for highly efficient second-order processes.

1.3 Integrated Photonics

Integrated photonics is a versatile platform to explore interesting electromagnetic devices due to the wavelength scale confinement. Here we will cover some of the basic operating principles of a few key photonic devices that will appear later in this thesis.

1.3.1 Waveguides

Waveguides were the first integrated photonic devices to be demonstrated [104] and remain one of the central components in integrated photonics. These structures provide confinement at the wavelength scale using total internal reflection (TIR) [1] (Fig. 1.3a), allowing light to be efficiently guided across an entire chip. While there are a number of possible cross-sections including slot and rib waveguides, in this thesis we will largely be concerned with the most basic form, the strip waveguide (Fig. 1.3b). While the refractive indices (n_{core}, n_{clad}, and n_{sub}) tend to be fixed by the choice of platform (e.g. silicon on insulator), the ability to vary the waveguide width (w) and thickness (t) allow for great tunability of the propagation properties of the electromagnetic wave, such as effective refractive index, modal shapes, and dispersion.

[1] Note that TIR does not actually apply for wavelength scale geometries, and the actual confining mechanism is index guiding[49]. However, TIR is commonly used to describe this phenomenon as it is easily accessible and so we will use it here as well.

While the use of Fresnel equations and the picture of TIR allows for a detailed understanding of waveguiding from analytic expressions directly derived from boundary conditions and Maxwell's equations, it is often more practical to evaluate the propagating waves numerically. These numeric methods are computationally cheap and can be easily applied to arbitrary waveguide geometries. These methods separate the solutions to Maxwell's equations into a cross-sectional and propagating component. For instance, the solution for the electric field would take the form: $\mathbf{E}(x,y,z) = \mathbf{E_0}(x,y)e^{-i(\omega t - \beta z)}$. Here, ω is the angular frequency of the light, β is the propagation constant, and $\mathbf{E_0}(x,y)$ is the solution to an eigenvalue problem of the form $\mathbf{A}\mathbf{E_0} = \beta\mathbf{E_0}$, where β is again the propagation constant, and $\mathbf{A}$ is an operator. For instance, in the scalar wave approximation this eigenvalue problem becomes [107]:

$$(\nabla_T^2 + k^2)\mathbf{E_0} = \beta\mathbf{E_0} \tag{1.7}$$

Where $\nabla_\mathbf{T} = \frac{\partial}{\partial x}\hat{\mathbf{x}} + \frac{\partial}{\partial y}\hat{\mathbf{y}}$ and k is the angular wavenumber. In this thesis we have used a fully vectorial solution (whose formulation has been omitted for brevity) as outlined by [126] and as implemented by Lumerical Inc. in their "Mode Solutions" software [2].

Solutions to these eigenvalue problems result in discrete sets of solutions known as eigenmodes. Furthermore, these solutions can be broken into two categories, quasi-transverse-electric and quasi-transverse-magnetic solutions. The quasi- prefix indicates that unlike the solutions for microwave waveguides with metallic boundaries [39], these modes are not completely transverse (there are nonzero components along the propagation direction). We will follow the convention of the field of integrated photonics and denote these modes TE, and TM, respectively. For illustration, let us consider the case where w and t are restricted to nearly half a wavelength. Under such conditions there are only two eigenmodes, one TE and one TM mode. For a silicon nitride strip waveguide surrounded by silicon dioxide with $w = 750\ nm$ and $t = 400\ nm$ at 1550 nm, the resulting intensity profiles for the TE and TM are that shown in Figs. 1.3c, and d, respectively.

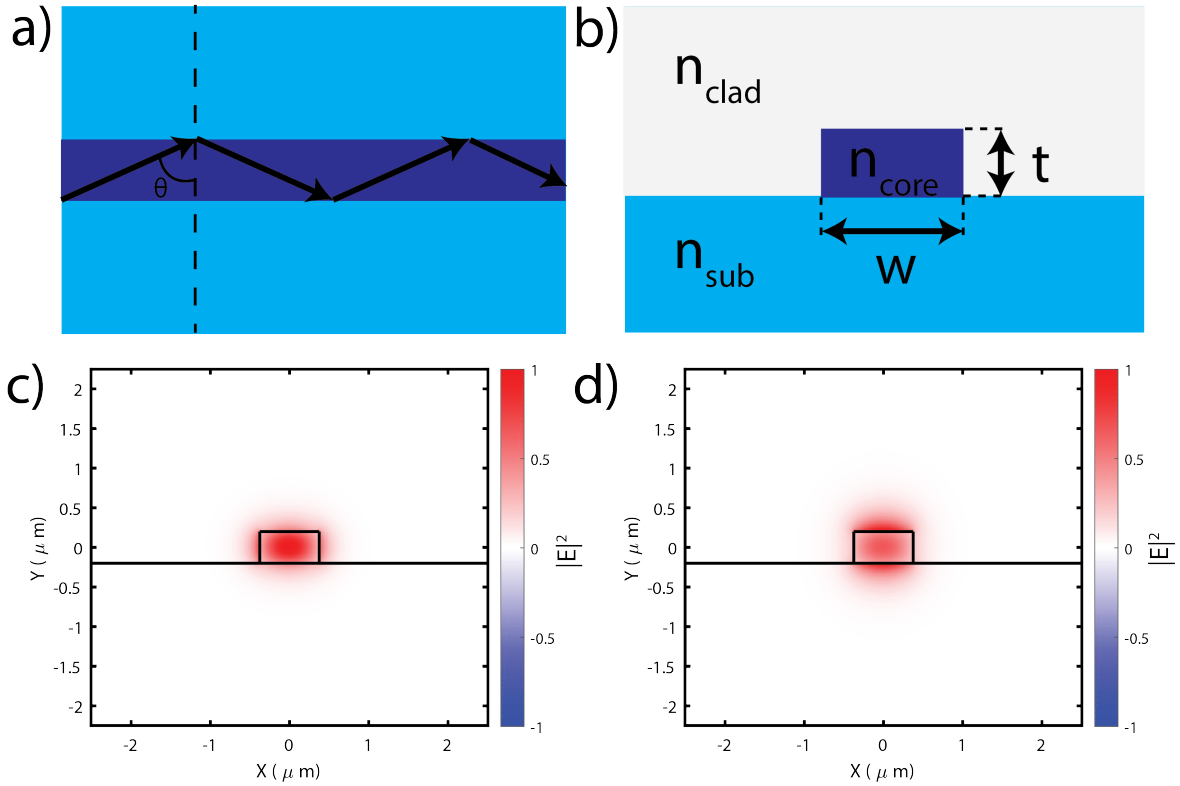

Figure 1.3: Integrated photonic waveguides. (a) Waveguides provide confinement through total internal reflection. This can be visualized by the arrows representing the ray tracing of a beam propagating along the waveguide. By assuming these rays are incident on the waveguide surfaces at an angle θ one can use Snell's law to infer confinement by total internal reflection. (b) Diagram of a strip waveguide. The waveguide core is made of a material with refractive index n_{core}, and with dimensions w, and t. This waveguide sits on a substrate with index n_{sub}, and is encapsulated by a material with index n_{clad}. Here we have shown a single mode silicon nitride waveguide with $w = 750nm$, and $t = 400nm$ with a silicon dioxide substrate and cladding layer. Such a waveguide has a single TE mode, and TM mode whose intensity profiles are shown in (c) and (d), respectively.

1.3.2 Resonators

Resonators serve a central role in integrated photonics as they allow an enhancement of the electric fields by spatially and temporally confining light. Such confinement allows for the enhancement of otherwise weak optical effects such as the thermal-optical effect [5], photo-refractive effect [82], and of central importance to this thesis, the $\chi^{(2)}$ nonlinearity [41]. The spatial confinement of a cavity is denoted by the mode volume, V_m. There are many definitions of V_m, however a commonly used definition defines it as:

$$V_m = \frac{\int \epsilon |\mathbf{E}|^2 dV}{max(\epsilon |\mathbf{E}|^2)} \tag{1.8}$$

The temporal confinement is denoted by the cavity quality factor, Q [49]:

$$Q = \frac{\omega U}{P} \tag{1.9}$$

Where ω is the resonant frequency, U is the total energy stored in the resonator, and P is the power dissipation rate. In steady state this power dissipation rate is the same as the power coupled into the cavity. Power buildup is a central benefit of cavity enhancement and equation 1.9 provides a clear picture of how this relates to the quality factor, but the temporal aspect is not immediately clear although it is another important benefit relating to the quality factor of a resonator. This can be made explicit, as one can also find that the photon lifetime (τ) and the cavity quality factor are directly related to one another [49]:

$$Q = \frac{\tau \omega}{2} \tag{1.10}$$

Finally, it is important to note that the ratio of Q^n/V^m for various positive integer values of n and m is a reoccurring figure of merit in the field of integrated photonics. For instance, the enhancement of an emitter's spontaneous emission rate by a cavity, known as the Purcell effect, is proportional to Q/V [87]. The thermo-optic and photo-refractive devices mentioned previously also experience enhancement proportional to Q/V [82]. However, as we will see,

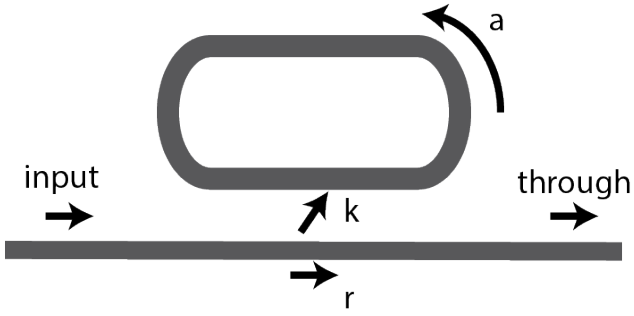

Figure 1.4: Schematic of a racetrack resonator fed by a coupled waveguide. a denotes the round trip loss, k is the coupling strength between the waveguide and racetrack, and r is the coupling strength of the waveguide to itself.

the $\chi^{(2)}$ nonlinearity scales as Q^3/V or Q^2/V^2, depending on the presence or absence of double-resonance [32] [30] [69] [76].

Ring and Racetrack Resonators

Ring and racetrack resonators are some of the most prevalent resonators in use in integrated photonics as they are simple to design and fabricate. This is largely because they are formed by wrapping a waveguide back on itself to form a ring or racetrack like structure. One key difference is that unlike waveguides, these resonators do not support a continuum of different frequencies, but rather a set of discrete frequencies/wavelengths that satisfy the condition:

$$\lambda_{res} = \frac{n_{eff}L}{m}, \quad m = 1, 2, ... \tag{1.11}$$

Where λ_{res} are the resonance wavelengths corresponding to a specific mode, n_{eff} is the effective index of that ring mode, and L is the circumference of the resonator. This condition

implies that only wavelengths that constructively interfere over a round trip are supported as all other wavelengths will destructively interfere, and thus are not supported. The wavelength separation ($\Delta\lambda$), also known as free spectral range (FSR) of these modes are easily calculated:

$$\Delta\lambda = \frac{\lambda^2}{n_g L} \tag{1.12}$$

A final detail to consider is the way in which ring resonators are excited. This is traditionally done by placing a "bus" waveguide in close proximity to the resonator. For our purposes let us consider a racetrack resonator as pictued in Fig. 1.4. Of note are the coupling strength between the ring and bus waveguide, k and r denotes the power transmitted past the resonator. Here, a denotes the round trip loss which is related to the waveguide propagation loss (α) by $a^2 = e^{-\alpha L}$. It can be shown that the power transmitted through the bus waveguide is equal to [14]:

$$T = \frac{a^2 - 2ra\cos(\phi) + r^2}{1 - 2ar\cos(\phi) + (ra)^2} \tag{1.13}$$

Where $\phi = \beta L$ is the round trip phase accumulation. The power that is not transmitted is coupled into the ring resonator, then dissipated by the round trip losses. By inspecting equation 1.13 we can see that all the power from the waveguide is coupled into the ring when $k = a$ as ϕ will be some multiple of 2π on resonance. This condition is referred to as critical coupling.

While a is usually determined by fabrication imperfections and ring circumference, k is readily tunable. When two waveguides are brought close together the eigenmodes of the waveguides are no longer independent, but rather are coupled into a set of "super-modes." Let us consider a set of waveguides with the same geometry as in Fig. 1.3 with a separation of 400 nm. We can find a set of TE polarized modes: one where the light in the two waveguides are in phase and are pulled together (Fig. 1.5a), and another where they are out of phase and repel each other (Fig.1.5b). The interference of these modes cause power to be cyclically exchanged between the waveguides over a distance known as the cross-over length:

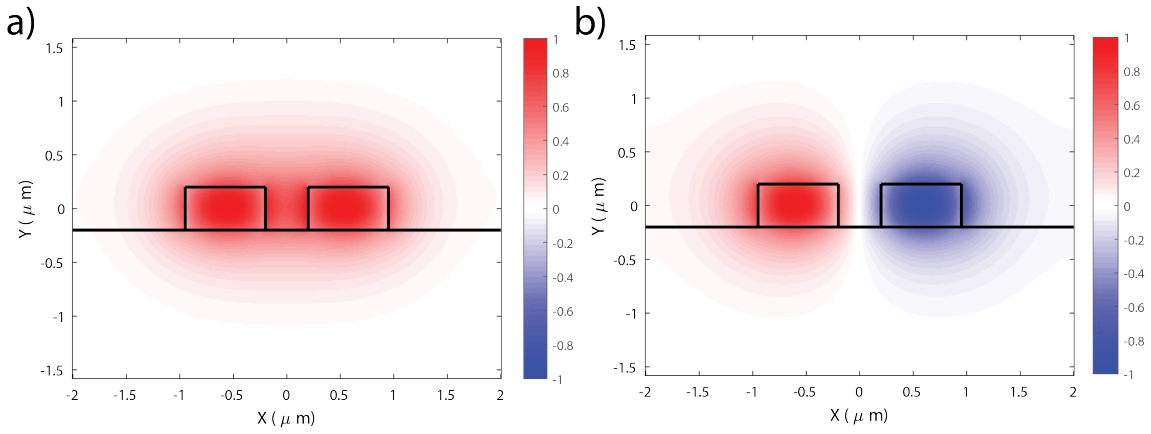

Figure 1.5: TE polarized super-modes of a silicon nitride waveguide coupler. (a) The real part of the E_x for the first and (b) second super-mode. The waveguides are 750 nm wide, 400 nm thick, separated by 400 nm with and encapsulated with silicon dioxide.

$$L_{cross} = \frac{\lambda}{2\Delta n} \tag{1.14}$$

where Δn is the difference in the effective indices for the two super-modes. This difference can be made larger by bringing the waveguides closer together, and therefore by virtue critical coupling in ring resonators tends to be found by varying the coupling gap until the associated coupling strength matches the round trip losses.

Photonic Crystals

Another commonly used resonator design is that of a photonic crystal cavity (PhCC). Photonic crystals (PhCs) have captured the imagination of scientists for several decades. They were first proposed by Lord Rayleigh in 1887 [90] but interest in the topic started in vigor in 1987 by Yablonovitch [123] and John [50]. These authors realized that light can be selectively guided by or reflected by periodic media depending on the relationship between the periodicity and the wavelength of light.

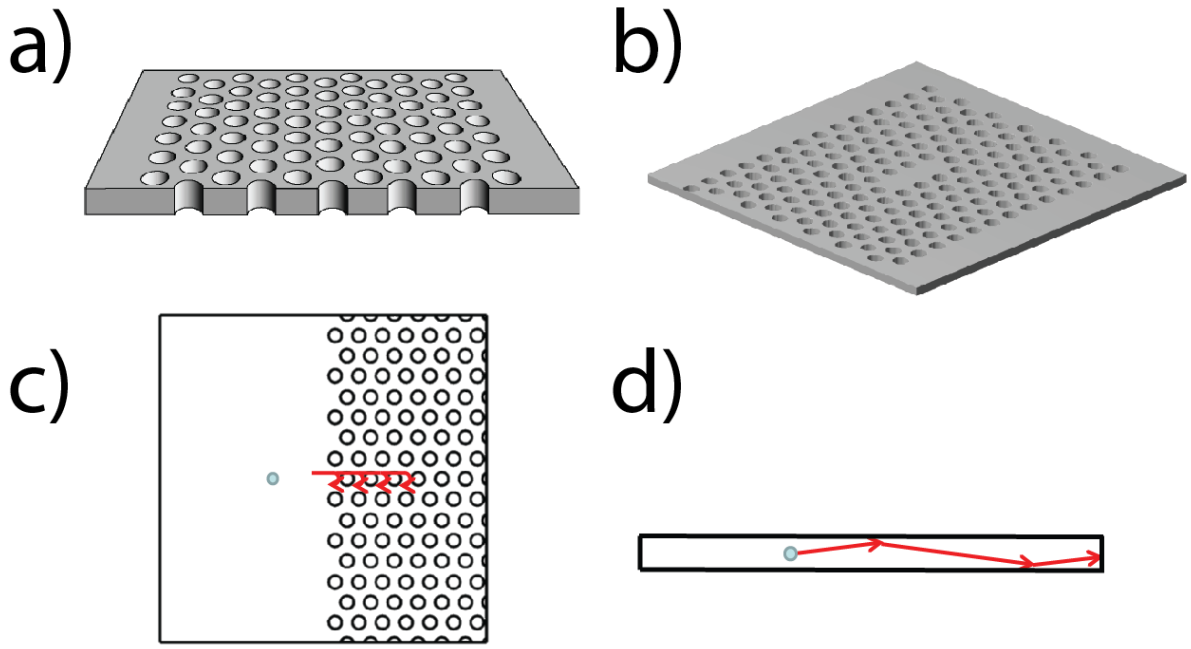

Figure 1.6: Basic photonic crystal operating principles. (a) Schematic of a photonic crystal, in essence a dielectric slab with a periodic array of holes. (b) A photonic crystal cavity created by removing three of the holes. (c) In plane confinement in photonic crystals is accomplished through distributed Bragg reflection. (d) Out of plane confinement is accomplished with TIR.

PhCs come in a variety of symmetries, but for brevity we will focus on "photonic crystal slabs" as they will appear later in this text (Fig. 1.6a). As the name suggests these PhCs are comprised of a thin dielectric slab, usually with a thickness on the order of half a wavelength ($\frac{\lambda}{2n}$), and are patterned with a periodic array of holes. The relationship between the size and periodicity of these holes to the size of a wavelength in the slab determines of the light can pass through or be reflected. The light confinement mechanism in the slab is known as distributed Bragg reflection (DBR) (Fig. 1.6c). Using such a DBR structure provides the in plane control needed to build more sophisticated structures such as photonic crystal waveguides and cavities. Out of plane confinement is provided by TIR just as it is for waveguides (Fig. 1.6d).

The exact frequencies that are guided in photonics crystals are found by solving for the eigenmodes of the crystal. Every photonic crystal is comprised of a unit cell (Fig. 1.7a purple outline) that is identical under translations of the unit vectors (Fig. 1.7a arrows labeled a_1 and a_2). In momentum space, more widely referred to as reciprocal space, our hexagonal lattice transforms into another hexagonal lattice (Fig. 1.7 b). If we were to find the eigenmodes for the entire unit cell of the reciprocal lattice we would need a fully three dimensional plot to see the results. The situation becomes much worse for the case where one has a three dimensional reciprocal lattice (here we have ignored the third dimension as there is only translational symmetry in two dimensions), one would require far more complex plotting schemes. It was realized that the symmetries of these reciprocal lattices result in redundant information, so one could retain all the repentant information by considering only a subsection that contained unique information. This is known as the irreducible Brillouin zone (IBZ) (Fig. 1.7b blue triangle). Furthermore, this simplifies plotting the solutions as they can all be represented by a one dimensional plot, regardless of the crystal symmetry by only plotting the solutions along the edges of the IBZ. For the case of a hexagonal lattice, this means plotting the solutions from the Γ point, to the M point, to the K point, and then back to the Γ point (Fig. 1.7b). The following eigenproblem is then solved at each point along the edge of the IBZ [51]:

$$(\nabla + i\mathbf{k}) \times \frac{1}{\epsilon}(\nabla + i\mathbf{k}) \times \mathbf{H} = (\omega/c)^2\mathbf{H} \tag{1.15}$$

For illustration let us consider a silicon photonic crystal with periodicity of 398 nm, and a radius of 116 nm in a slab 220 nm thick. The resulting band diagram is shown in Fig. 1.7c. The red lines correspond to TE polarized modes and the blue lines correspond to TM polarized modes (only the first nine of each are shown). The grey area is known as the light cone and corresponds to momentum-frequency pairs that couple into free space. These bands are the only pairs of momentum and frequencies that are able to pass through the photonic crystal, all other frequencies are reflected. For instance, the field profile of the first TE band at the K point is shown in Fig. 1.7d (H_z component).

Now that we understand which modes are allowed to propagate through the crystals and those that are not, we can revisit the idea of forming cavities. Photonic crystal cavities (PhCCs) can be formed by creating any sort of defect within the crystal, resulting in light with frequencies that fall between the bands (in a region known as band-gaps) are trapped in the defect region. A widely used defect is the L3 (Fig. 1.6b) where three holes are removed in a line. This is largely due to years of work that have shown L3 cavities are able to achieve incredible Q/V ratios [58] [78]. While we have only reviewed the design of hexagonal photonic crystals, the same analysis applies to all photonic crystals.

1.4 Past Work in Integrated Nonlinear Optics

Integrated photonics provides an interesting platform to explore nonlinear optics due to the wavelength scale geometries. For instance, as we saw in section 1.3.1 we can control the dispersion in waveguides by varying their cross-sections. This extra dispersion allows for a material independent method of phase-matching that is not present in traditional SHG systems that utilize bulk crystals.

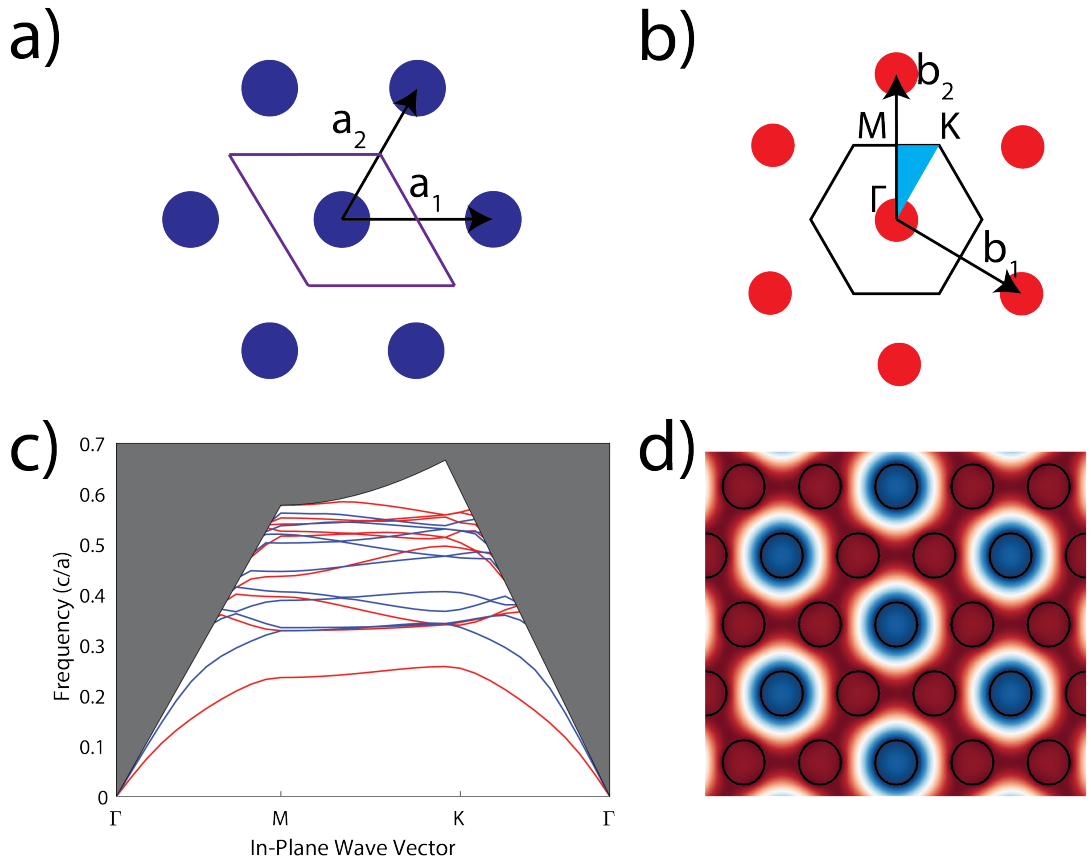

Figure 1.7: Bandstructures of photonic crystals. (a) The hexagonal lattice we will be considering. Here we have labeled the lattice vectors a_1 and a_2. (b) The reciprocal lattice of that shown in (a), which itself is a hexagonal lattice. The reciprocal lattice vectors are given by b_1 and b_2. The symmetries of the lattice of the lattice result in symmetries in the bands. The area without redundancies is known as the irreducible Brillouin zone (IBZ) and is highlighted in light blue. The corners of the IBZ are labeled Γ, M, and K. (c) Band diagram of a silicon photonic slab with a hexagonal hole structure. Only the first nine TE (red) and TM (blue) modes. The light cone is shaded in grey. Slab thickness of 220 nm, periodicity of 398 nm, and a radius of 116 nm. (d) H_z field profile of the first TE band at the K point. The holes are outlined in black for clarity.

1.4.1 Second Harmonic Generation in Aluminum Nitride Waveguides

This geometric dispersion is how phase matching has been achieved in an aluminum nitride on silicon platform [85]. The authors designed the height of the waveguide to allow single mode operation at 1550 nm. Next they varied the width of the waveguide and monitored the effective refractive index of the fundamental mode at 1550 nm and the higher order modes at 775 nm. At a waveguide with a width of just over 1 μm they found the effective indices of the TE_{00} mode at 1550 nm matched the effective index of the TE_{20} at 775 nm. A power series on the waveguides revealed the quadratic scaling of the SHG with respect to the input pump power. This is exactly what we would expect from the linear increase in SHG electric field amplitude associated with phase matching as we saw in Fig. 1.2b. A wavelength sweep on these same waveguides revealed a narrow band of phase matching. This is consistent with what we saw in Fig. 1.2a, with the understanding that a small change in wavelength corresponds to small change in momentum matching. This is what we should expect as changing the wavelength changes the ratio of light that travels in the waveguide core versus in the cladding layer, changing the effective index of the mode.

Because of the strong scaling with the power at the fundamental wavelength, a natural way to increase efficiency and output power is to use a ring resonator formed of a phase matched waveguide. In this way power at both the fundamental and harmonic frequencies will build up inside the ring. This simple method of designing a nonlinear resonator has resulted in some of the highest reported conversion efficiencies in an integrated platform [41]. Though the design is simple it is generally well understood that the mode matching condition is heavily reliant on precise fabrication of the waveguide width.

While we have presented the work in aluminum nitride, it is worth noting that the method of using geometric dispersion is a well established technique within the field that has been extended to a number of material systems. For instance, these same principles have been extended to the surface nonlinearities of silicon nitride [61], as well as more traditional nonlinear media such as gallium arsenide [19].

1.4.2 Theory of Second-Order Nonlinearity within Micro-Resonators

The use of phase matching has guided our understanding of efficient SHG configurations for not only the bulk systems, but also for the case of waveguides and ring resonators. In fact, it was nearly effortless to extend the notion into the integrated photonic setting, as we were simply manipulating index in both cases. However, this idea does not extend as well to standing wave resonators. In order to gain clarity for these cases, a generalized understanding of $\chi^{(2)}$ processes becomes important. The solution to this problem was presented by Burgess et al. [17] with their idea of a nonlinear overlap. This was accomplished by abstracting out the notion of specific electric field distributions, which allowed an expression for the conversion rate between frequencies for any $\chi^{(2)}$ process, which has the following form:

$$\beta = \frac{1}{4} \frac{\iiint dV \epsilon_0 \sum_{ijk} \chi^{(2)}_{ijk} E^*_{1i} (E^*_{2j} E_{3k} + E^*_{2k} E_{3j})}{\sqrt{\iiint \epsilon |E_1|^2 dV} \sqrt{\iiint \epsilon |E_2|^2 dV} \sqrt{\iiint \epsilon |E_3|^2 dV}} \tag{1.16}$$

Here, the numeric subscripts indicate which of the three fields we are considering, while the letter subscripts refer to the polarization. It is worth noting that β has units of $J^{-1/2}$ and $|\beta|^2$ is proportional to the conversion efficiency obtained by the cavity in question at low pump powers [16]. This nonlinear overlap is consistent with the notion of phase matching and has become an indispensable tool for the design and analysis of ultra-compact frequency conversion devices.

1.4.3 SHG in Nanobeam Cavities

The use of β is particularly attractive when compact frequency conversion devices are desired. For instance, it has found use in designing photonic crystals for SHG enhancement [16] [94]. For instance the work by Buckley et al. explored designs of nanobeams in gallium arsenide (GaAs) that have resonances separated by an octave [16]. Here, the matter of achieving efficient frequency conversion requires additional consideration beyond what the previous uses of phase matching provided, but which the nonlinear overlap readily provides.

Another point where these ultra-compact frequency conversion devices differ from the waveguide based approach is in the nontrivial task of ensuring resonances at the fundamental and harmonic wavelengths. In waveguide systems this requires minimal work, as the fundamental wave simply needs to be above the frequency cutoff for the chosen geometry (e.g. waveguide thickness), and the harmonic mode will naturally be supported. The same is not true for photonic crystal structures, as one must also ensure there are bands near both frequencies. Nanobeams are particularly well suited for this task, as they more readily confine bands beneath the light cone compared to the traditional slab photonic crystals [16]. In addition, the bands must be of a compatible symmetry such that β integrates out to a nonzero number. The authors presented a suitable design that manages to satisfy the frequency overlap momentum matching, and retain high quality factors. However, due to the challenging nature of the device fabrication, the experimental demonstration of such a device is anticipated but yet to be reported.

1.5 Present State of Compact SHG Devices

The field of developing ultra-compact SHG devices is still very active. This is primarily due to the challenge of designing resonant structures that (1) have modes at the fundamental and harmonic frequencies, (2) have large quality factors, and (3) have large values of β. There have been a number of interesting proposed designs for these nanocavity enhanced SHG [63] [12] [95] [16] [94], but a common factor is in the difficulty in both the design and fabrication of these devices. For instance, a sensitivity analysis of a GaAs microdisk resonator presented by Kuo et al. showed that an error of the radius on the order of 5 nm degrades the performance of the device by over an order of magnitude [55]. The work presented in this thesis aims to develop a platform to provide a $\chi^{(2)}$ platform that is scalable and has relaxed fabrication tolerances by utilizing the nonlinearity of 2D materials coupled to linear resonators.

1.6 Transition Metal Dichalcogenides Monolayers

The discovery of graphene (Fig. 1.8b) in 2004 [80] marks one of the most important scientific achievements of the last few decades. This discovery was the beginning of a vast search for other atomically thin materials. Soon after the discovery of graphene came the discovery of the transition metal dichalcogenides [71], a family of atomically thin semiconductors. Like graphene, these materials have a hexagonal lattice, but rather than a single atom thick they measure three atoms thick (Fig. 1.8a). These materials have the chemical form of MX_2, where M is either Mo or W, and X is either S, or Se. The atomically thin vertical electronic confinement endues graphene with a number of remarkable traits, including excitons that are stable at room temperature [42] [21]. However, there are two other properties of these materials that are of utmost importance to this work.

The first of these is the van der Waals bonding of 2D materials. This feature has been critical for the further exploration of all members of the 2D material family. Thanks to this useful property 2D materials can be stacked onto one another to form hetero-structures [93] [120] [37]. For instance, TMDs are frequently sandwhiched between flakes of hexagonal boron nitride (hBN). Hexagonal boron nitride is an excellent insulator with a bandgap of nearly 6 eV [119], and has been most useful as a gate dielectric in TMD based LED structures [120] [97], and is also very effective as a passivation layer that significantly reduces the inhomogenous broadening of TMD excitons [4]. However, in this work this property is most useful as it allows these materials to be transferred onto arbitrary substrates. This ease of integration provides a stark contrast to the usual methods required to bond media together, namely wafer bonding or epitaxial growth, both of which are notoriously difficult and substrate dependent.

Secondly, these materials have an appreciable $\chi^{(2)}$ nonlinearity. Far from the exciton resonances these materials have susceptibilities in the 10's of pm/V [101], which is comparable to common nonlinear media such as lithium niobate [98]. However, on and near the exciton these values reach an extraordinary levels of several nm/V [54] [48]. Furthermore, the D^{3h}

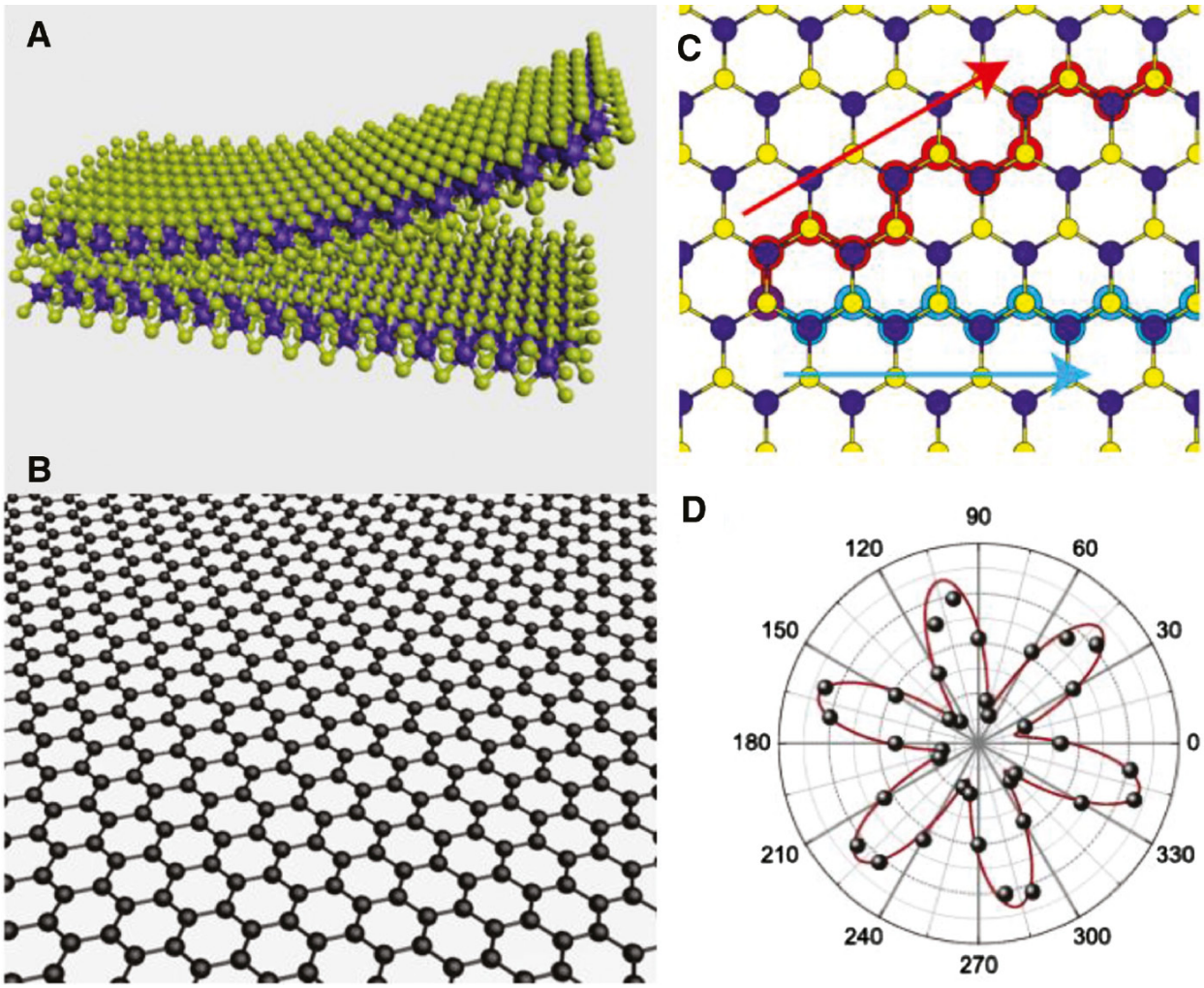

Figure 1.8: (a) TMDs are atomically thin, measuring only three atoms thick. Multilayers are bound by van der Waals forces, and thus can be pealed apart. (b) Graphene, the first 2D material also shares a hexagonal lattice structure. (c) TMDs have two axes, the arm-chair axis (red), and the zig-zag axis (blue). (d) Polarization resolved SHG of TMDs reveal a hallmark six-fold pattern that reflects the underlying crystal symmetry.

symmetry of these materials endow their SHG radiation with a characteristic 6-fold pattern in polarization resolved SHG (Fig. 1.8d) [101].

These traits make TMDs very appealing for integration with cavities to enhance their nonlinearities. However, there are relatively few studies showing SHG enhancement using dielectric structures. There have been a few notable works including enhancement of a MoS_2 monolayer by a DBR cavity [23], and enhancement of $GaSe$ by a silicon PhCC [34]. For a more complete review please refer to our paper [110].

1.7 Document Organization

The rest of the work is organized as follows: In chapter 2, I will cover the theoretic framework used to analyze and improve the nonlinearity of TMD based integrated SHG devices. Further analysis of the nonlinearity of highly nonlinear SHG devices, specifically prediction of bistability, is covered in Chapter 3. Chapter 4 presents the experimental progress in integrated SHG devices that utilize TMDs, followed by Chapter 5 which presents our work on a silicon nitride platform for hybrid photonics. Chapter 6 shows our latest attempts at utilizing this platform for cavity enhanced SHG, with several suggestions for future work. Finally, we will conclude with an outlook in Chapter 7.

Chapter 2

THEORETIC MOTIVATION FOR PATTERNED LAYERED NONLINEAR OPTICS

As illustrated by previous works in integrated nonlinear optics, the combination of momentum and frequency matching in addition to maximizing the nonlinear overlap integral is a daunting task. Traditionally, the cavity is made of the nonlinear material itself. This implies that the optimization process for all three optimization problems are tightly coupled and in practice, optimizing one condition has negative effects on the other two. However, the extreme thinness and the van der Waals bonding of TMDs provides a way to circumvent such an unruly optimization problem. Specifically, we will use the assumption that when placed on a photonic device, say a waveguide, the 2D material will minimally perturb the optical mode. In fact, we will take this assumption to the limit of no perturbation at all. By constructing the photonic circuitry out of materials that lack the second order nonlinearity, we will be able to separate the problems of creating a doubly resonant cavity with high quality factors and that of maximizing the overlap integral.

This scheme should work for any photonic platform with sufficiently high index of refraction or thin enough nonlinear material, such that our assumptions hold true. As we are interested in SHG with a fundamental wavelength of 1.55 μm we require a wide bandgap material for our photonics, eliminating silicon as the substrate of choice. Instead we will opt for silicon nitride as it is also a CMOS compatible material with excellent optical properties, but has a wide bandgap. With a refractive index of nearly 2 for much of the NIR and visible, SiN can retain TIR even when surrounded by silicon dioxide, making for an excellent photonic material platform. A schematic of our proposed platform is depicted in Fig. 2.1.

The work presented here provides evidence that the nonlinearity of evanescently coupled

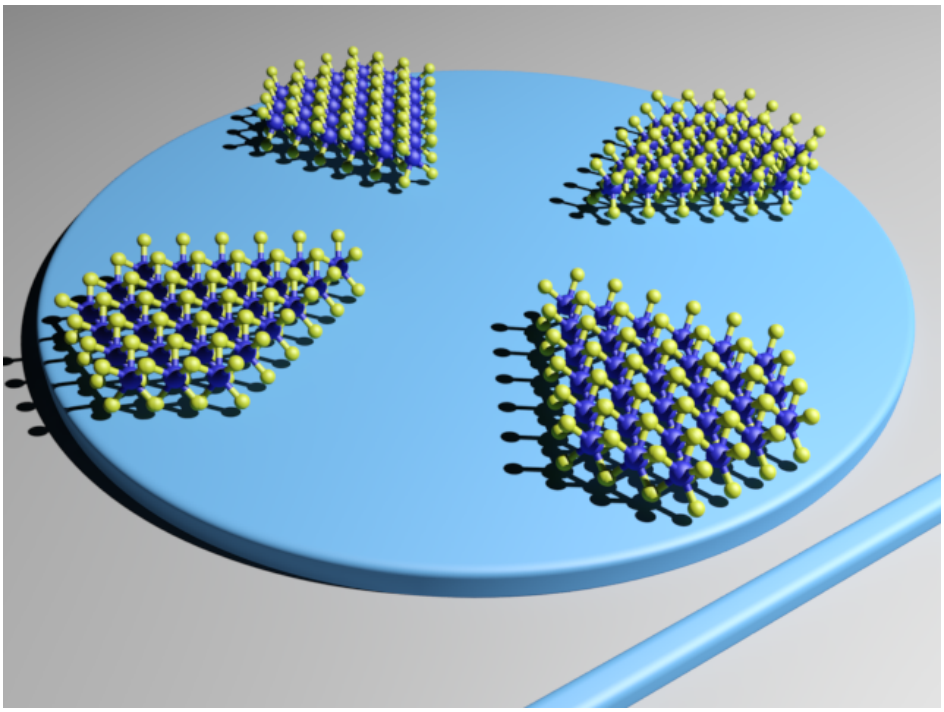

Figure 2.1: A schematic of our proposed hybrid integrated nonlinear optics platform. Our platform utilizes the passivity and scalability of silicon nitride (shown in dark blue) on silicon dioxide (in gray), and the nonlinearity of MX_2s. [32].

2D materials can provide a suitably large nonlinearity, and perhaps more importantly, that patterning the 2D material can recover a non-zero nonlinear overlap in resonators that are not phase-matched.

2.1 Patterned nonlinear optics in waveguides

We started our analysis in a simple waveguide system. As in the past [85] [41], we started with a waveguide of fixed height and varied the width until a mode at the harmonic frequency matched the effective index of the fundamental mode at the fundamental frequency. In our case, we started with 330 nm silicon nitride on thermal oxide. By varying the width we found that we can achieve the mode matching condition at a waveguide width of roughly 1.1 μm (Fig. 2.2a). At this width we found the TE_{00} mode at 1550 nm has the same effective index as the TE_{20} mode at 775 nm (mode profiles shown in the insets of Fig. 2.2a). The final points that need consideration are those regarding the 2D material. We will assume that the zig-zag axis of the 2D material is along the y-direction, that is, perpendicular to the propagation direction and to the normal of the wafer surface. In this way we can achieve maximal alignment of the field polarizations with the susceptibility of the material. Since the optimization of the nonlinear overlap only requires consideration of field and crystal symmetries, we will save the consideration of the actual nonlinear values for later. From these assumptions and mode profiles we can calculate the nonlinear overlap using equation 1.16. For illustration we have shown the nonlinear overlap as if the nonlinear material was everywhere in Fig. 2.2b. We only need to consider the nonlinear overlap where the 2D material will lie, which is illustrated with a red dashed line. The 1D plot of the nonlinear overlap is shown in the inset. Here we can see that the simple phase-matched waveguide already presents an opportunity to optimize the nonlinear overlap integral by patterning the TMDs to only include the "positive", or "negative" terms. If we choose to keep the "negative" term (etch away the material on the sides of the resonator), we see an enhancement by a factor of 3.2, while if we pattern it in the opposite manner we see an enhancement by a factor of 1.8. Note, we have also assumed that the material does not extend past the edges

of the waveguides, as the material would wrap and conform to the waveguide edges. This would cause the material to be misaligned with the dominant electric fields (due to their 2D nature these materials do not have $\chi^{(2)}$ components normal to their surface).

2.2 Patterned nonlinear optics in large ring resonators

For a more complete understanding of our system, we will begin by deriving an expression for β specific to our hybrid platform. Here we will start with the most general form of β [17]:

$$\beta = \frac{1}{4}\frac{\int dV \epsilon_0 \sum_{ijk} \chi^{(2)}_{ijk} E^*_{1i}(E^*_{2j}E_{3k} + E^*_{2k}E_{3j})}{\sqrt{\int \epsilon |E_1|^2 dV}\sqrt{\int \epsilon |E_2|^2 dV}\sqrt{\int \epsilon |E_3|^2 dV}} \tag{2.1}$$

We can see that the three interacting waves are denoted by the numeric subscripts and that the polarizations are given by the alphabetic subscripts. As we are considering a degenerate case (specifically, SHG), we can combine some of the terms.

$$\beta = \frac{1}{2}\frac{\int dV \epsilon_0 \sum_{ijk} \chi^{(2)}_{ijk} E^*_{fi}E^*_{fj}E_{hk}}{\int \epsilon |E_f|^2 dV \sqrt{\int \epsilon |E_h|^2 dV}} \tag{2.2}$$

Where we have replaced the numeric subscripts with f and h, which denote the fundamental and harmonic wave, respectively. Since we are in a waveguide system we know that our electric fields are those of a simple traveling wave and can be written as $E = A(r,z)e^{-i(kr\theta - wt)}$. Here $A(r,z)$ is the cross sectional mode profile. We also must take care to note that $k = \frac{\lambda}{2\pi n_{eff}}$ where n_{eff} is the effective index of the waveguide mode rather than n, the material refractive index. Since the modulus square of this exponential term is always unity we can simplify our denominator to:

$$\int \epsilon |A_f|^2 dV \sqrt{\int \epsilon |A_h|^2 dV} \tag{2.3}$$

With the assumption that TMDS are our nonlinear media, we can make some simplifications to the numerator as well. Specifically, we know these materials belong to the $P6_3/mmc$

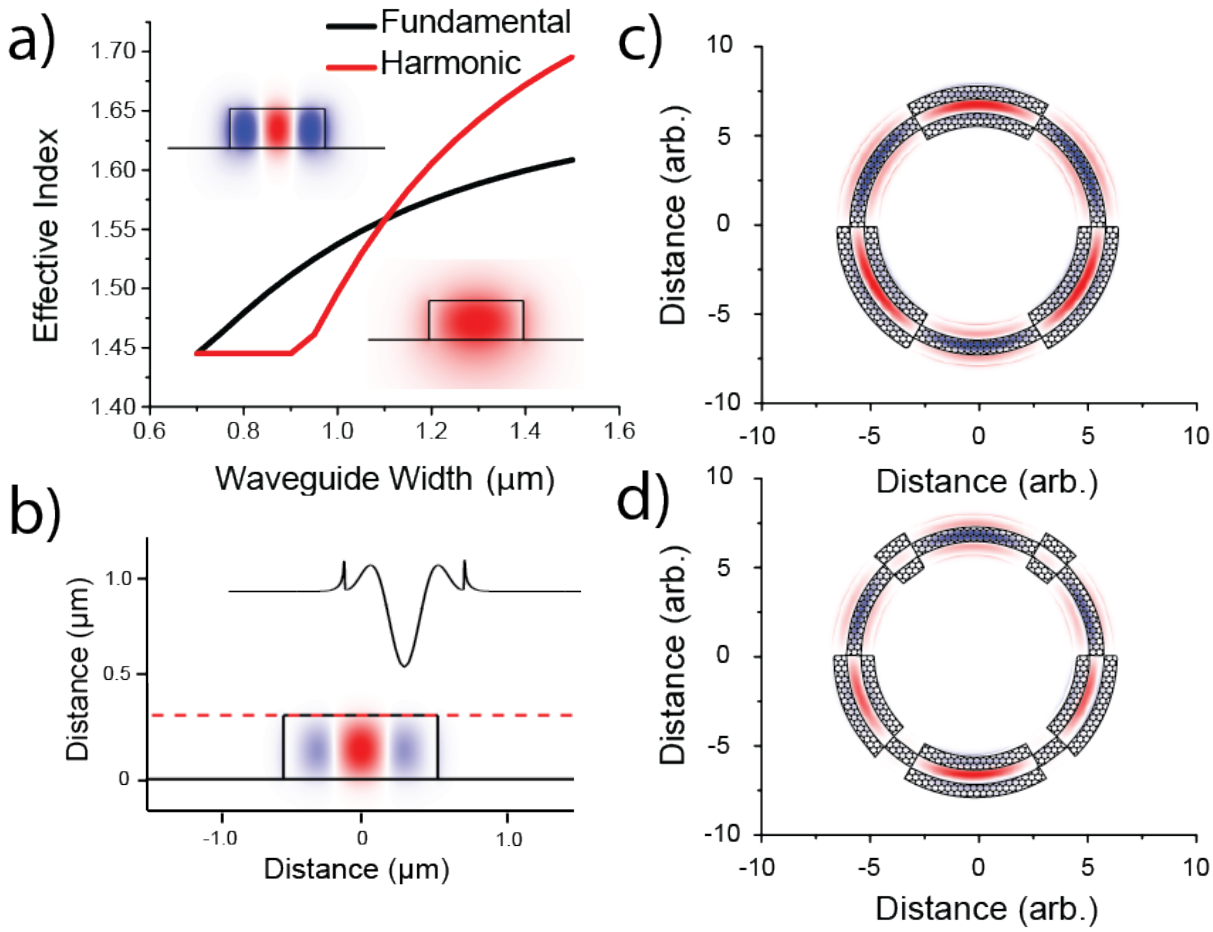

Figure 2.2: Modal analysis and patterning schemes for a TMD-silicon nitride hybrid nonlinear system. (a) By varying the width of the silicon nitride waveguide we were able to find that the TE00 mode at 1550 nm (mode profile shown in the lower right inset) had the same effective index as the TE20 mode at 775 nm (mode profile shown in the upper left inset). (b) By momentarily assuming there is nonlinear media everywhere we can visualize the nonlinear overlap to gain a better understanding of its structure. However, a horizontal slice where the material is (shown in the inset), is a more realistic depiction of the nonlinear overlap. (c) Optimal patterning in a QPM ring. The TMD is indicated by the hexagonal grid overlayed on top of the nonlinear overlap, whose sixfold structure is indicative of the QPM nature of this ring (as it reflects the TMD crystal structure). (b) The optimal patterning for an arbitrary set of mode mismatching ($\Delta m = 2$). [32].

crystal symmetry and thus the nonzero elements are $d_{yyy} = -d_{yxx} = -d_{xxy} = -d_{xyx}$ [48]. The summand in the numerator can then be expand to:

$$\sum_{ijk} \chi^{(2)}_{ijk} \vec{E}^*_{fi} \vec{E}^*_{fj} \vec{E}_{hk} = \chi^{(2)}[-2E^*_{fx}E^*_{fy}E_{hx} - \ E^{*2}_{fx}E_{hy} + \ E^{*2}_{fy}E_{hy}] \tag{2.4}$$

Where $\chi^{(2)}$ represents the magnitude of the four equivalent elements in the full susceptibility tensor. This can be simplified with the understanding that the enclosing integral is taken only over regions with nonlinear material. As these materials have sub-nanometer thickness [125], we can approximate that the fields do not change significantly over their vertical extent and that we can replace the volume integral with a surface integral multiplied by the material thickness, d. To visually distinguish these fields at the surface from the full mode profile, $A(r, z)$, we will refer to them as $L(r)$. Note the lack of time dependence. This is because the time dependent terms cancel out with one another as $\omega_h = 2\omega_f$ by definition (of SHG) and energy conservation. This is particularly noteworthy as rings are, in general, traveling wave resonators (of course you can always excite standing waves in rings with the proper pump conditions), but the nonlinear overlap itself is not a function of time. Thus, the numerator can be rewritten as:

$$d\epsilon_0\chi^{(2)} \iint_{NL} r dr d\theta L^{*2}_{fr} L_{hr}[-\sin(3\theta)]e^{-i\Delta m\theta} \tag{2.5}$$

Here we have converted to cylindrical coordinates, and the NL subscript indicates that the integral is to be only taken over the regions with nonlinear material (as we have taken $\chi^{(2)}$ out of the integral). This has allowed for the sum of different electric field components to combine into the single $sin(3\theta)$ term. This term reflects the symmetry of the underlying crystal structure. We know ring resonators only support modes with $kR\theta = m$ where m is a nonzero, positive integer and R is the ring radius, and k is the angular wavenumber. Therefore, we have used $\Delta m = |2\Delta m_f - \Delta m_h|$ to indicated the mode mismatch. As we will be considering rings whose radius is much larger than the waveguide width, we will approximate that the value of r remains constant over the radial integral. Thus, we can find

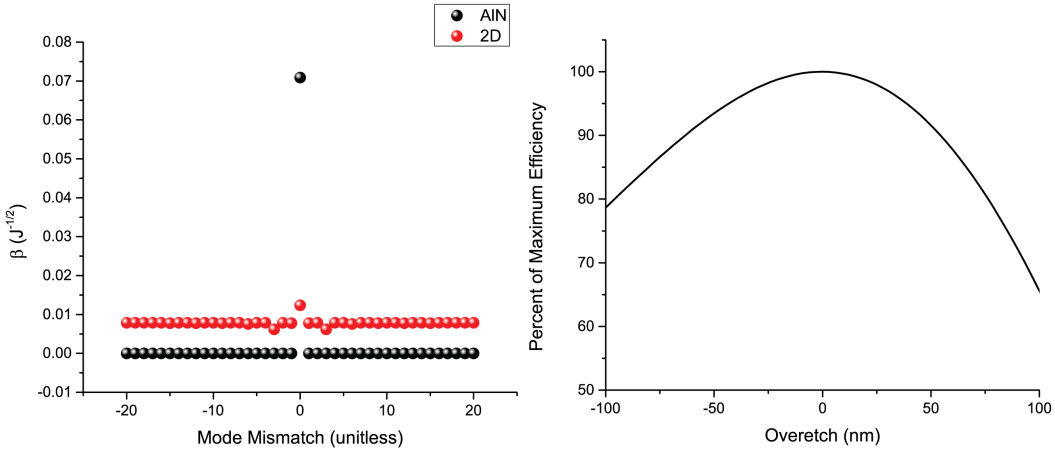

Figure 2.3: The flexibility of a patterned TMD SHG platform. (a) The nonlinear overlap integral for the two material platforms: the patterend 2D material platform and the AlN platform. The AlN is highly nonlinear for phase matched devices, but has very low nonlinearity for any mode mode mismatch. The 2D material platform on the other hand has a low nonlinearity, but consistently so regardless of mode mismatch. (b) We retain large percentages of the maximal nonlinear overlap for large over or under etching.

our final expression for β:

$$\beta = \frac{\chi^{(2)} d\epsilon_0}{2\sqrt{R\left(2\pi\right)^2}} \frac{\int\int L_{fr}^{*2} L_{hr} dr e^{i\Delta m\theta} \sin(3\theta) d\theta}{\iint \epsilon \left|A_f\right|^2 da \sqrt{\iint \epsilon \left|A_h\right|^2 da}} \tag{2.6}$$

The geometries we have found for phase-matched rings in our hybrid platform are comparable to those reported for aluminum nitride [121], providing an interesting point of comparison between the two platforms. Specifically, we compared the valulohyly,ewqaes of β that were achievable in each platform, for a ring of radius 100 μm. The work by the Hong-Tang group uses polycrystaline AlN that only has the out of plane crystal axis aligned with each other [122]. This means that the $\chi^{(2)}$ tensor only has a single non-zero element, which is taken to be $\chi^{(2)}_{zzz} = 5\ pm/V$ in accordance with previously measured values [85]. Likewise, the values of the $\chi^{(2)}$ tensor of TMDs are well tabulated and we have taken $\chi^{(2)}_{yyy} = 60\ pm/V$, which matches values measured for WSe_2 at 1550 nm [101]. In doing so we found that

$\beta_{AlN} = 0.09\ J^{-1/2}$ and $\beta_{2D} = 0.009\ J^{-1/2}$. This order of magnitude difference is due to the small overall nonlinearity provided by the TMDs, originating from its incredibly small volume. Another issue is that unlike the AlN platform our platform suffers from the additional disadvantage of having to evanescently couple to the nonlinear material, unlike the AlN platform where the resonator is composed of the nonlinear material itself. However, our platform was not designed to achieve the most nonlinear cavities, but rather the nonlinear cavities that are more flexible and forgiving to fabrication errors. For example, in the case of mode mismatch, β for the AlN ring identically falls to zero, while the patterned 2D rings β remains at $0.008\ J^{-1/2}$ or higher, depending on the amount of momentum mismatch (Fig. 2.3a). Beyond being a flexible platform that can account for fabrication errors in the construction of the resonators, it is also forgiving in the patterning of the TMDs. This is illustrated in Fig. 2.3 b which shows the overlap decrease as a function of over or under-etching of the material. Here we considered patterning for the central overlap lobe, shown in the inset of Fig. 2.2b. Our analysis shows that our patterning scheme allows for the 2D material to be over-etched by as much as 60 nm and suffer only an additional 10% loss in nonlinear overlap, attesting to the flexibility of our platform.

2.3 Patterned nonlinear optics in small disk resonators

This hybrid system becomes particularly appealing for small mode volume devices where it becomes more difficult to design cavities with large overlap. To analyze this case, we designed small mode volume disk resonators. Specifically, we analyzed a disk resonator made of gallium phosphide (GaP) 200 nm thick and roughly 3 micrometers in diameter. With these dimensions we found that the disk resonator was QPM. We then calculated the nonlinear overlaps for the GaP disk itself and for a patterned monolayer placed on top, while ignoring the contributions of the GaP. We found that $\beta_{GaP} = 4.734\ J^{-1/2}$ and $\beta_{2D} = 0.570\ J^{-1/2}$, which is consistent with our comparison of large ring resonators of SiN and AlN. We then considered the nonlinear overlap between non-quasi-phase-matched modes. Here, we again found that the patterned 2D platform was able to retain significant overlap whereas the

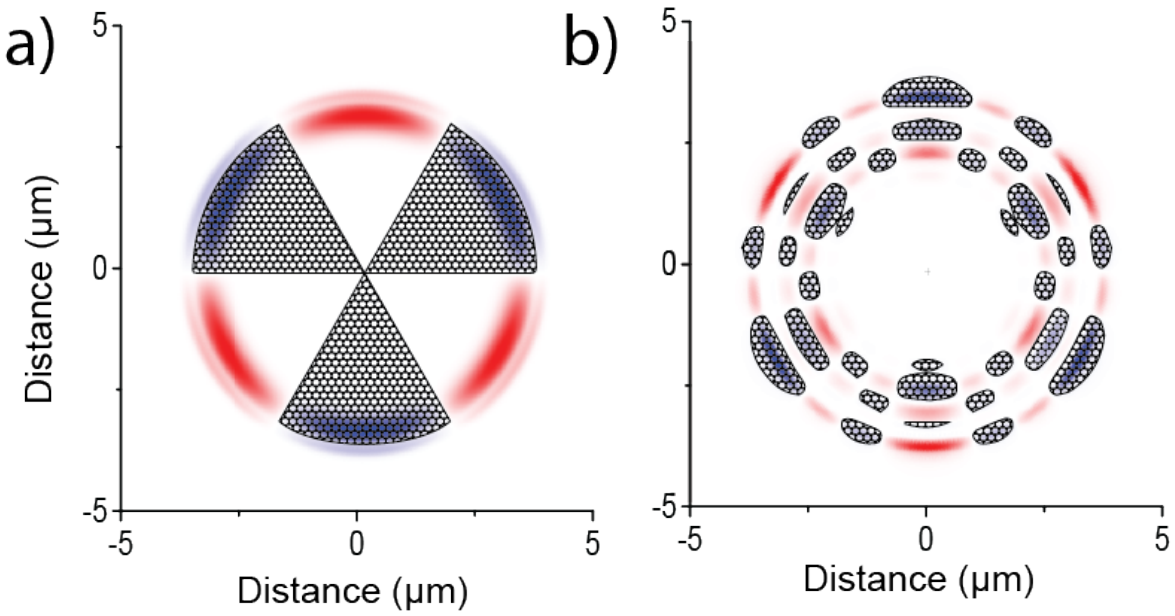

Figure 2.4: Nonlinear 2D material clad disk resonators: The nonlinear overlap integrand for a microdisk resonator integrated with 2D materials on top. The patterned hexagonal regions correspond the optimal patterns for the 2D material for (a) harmonic and fundamental modes with radial mode index $\rho = 1$, and $m_h = 2 \times m_f = 30$, and (b) $\rho_f = 1$, $\rho_h = 4$ with $m_f = 15$, and $m_h = 40$.

overlap for the GaP disk tended to zero. To further demonstrate the flexibility of this system, we extended our analysis to arbitrary silicon nitride disk resonators (Figure 2.4a,b). We chose a SiN thickness of 350 nm and a radius of approximately 3 μm. Here we can find that there are modes near 1550 nm with $m_f = 15$ and 775 nm with $m_h = 40$ (Fig. 2.4a). By properly patterning this disk we can find that β can be as large as 0.1626 $J^{-1/2}$. In fact by varying the radius of the disk it can be shown that more complicated modes can be put into a frequency overlap, and that proper material patterning can readily recover β there as well (Fig. 2.4b). Also, we note that the nonlinearity of these disks is much larger than that of the rings due to the smaller mode volumes of these disks.

2.4 Conclusion

By analyzing several cases, we were able to show that our proposed hybrid nonlinear platform poses significant merit. Although we found that our system has about an order of magnitude smaller nonlinear overlap compared to well optimized cavities made entirely of nonlinear material, we found that our hybrid system was far more robust when subjected to suboptimal mode symmetries. While we only analyzed whispering gallery mode resonators our approach applies equally well to standing wave resonators such as photonic crystal cavities. Furthermore, while we have thus far only considered patterning evanescently coupled TMDs, we can envision this technique being extended to other thin evanescently coupled nonlinear materials. This would be particularly well suited for emergent materials such as barium titanate which has an incredible susceptibility of $r_{42} = 923\ pm/V$ [3].

Chapter 3

BISTABILITY IN HIGHLY NONLINEAR CAVITY SYSTEMS

While frequency conversion is a useful technology in of itself, it is well known that it can also give rise to optical bistability. In fact, bistable photonic devices have been a long standing goal of the NLO community, as they would allow photonics to serve as a computing platform and not just a communications platform. To this end, we analyzed the performance metrics needed for an ideal SHG device to demonstrate bistability at the tens of photons level. As we are working with the assumption that we will be using an ideal cavity, our mental picture should be something similar to that in Fig. 3.1a. Specifically, we will forget the notion of exact mode profiles and simply assume a resonance at the fundamental frequency labeled mode a, and one at the second harmonic frequency, which we will label mode b. For illustration, we imagine that such a cavity would be a micro-cavity, perhaps a standard L3 cavity made of a nonlinear material such as $GaAs$ as depicted in Fig. 3.1c. Another option is where the cavity is made of a linear material where a nonlinear medium, such as a TMD, could be latter added on top as depicted in Fig. 3.1d.

3.1 Modeling of Bistability

A system consisting of two optical resonances mediated by a SHG interaction can be described by the Hamiltonian [70]:

$$\widehat{H}_s = \hbar\omega_a a^\dagger a + \hbar\omega_b b^\dagger b + \hbar g_{nl}[b(a^\dagger)^2 + b^\dagger a^2]. \tag{3.1}$$

Where g_{nl} is the coupling strength between the fundamental mode (at frequency ω_a), and the harmonic mode (at frequency ω_b). Here a and b represent the annihilation operators, and $\hbar$ is Planck's constant. The coupling coefficient can be expressed as [70]:

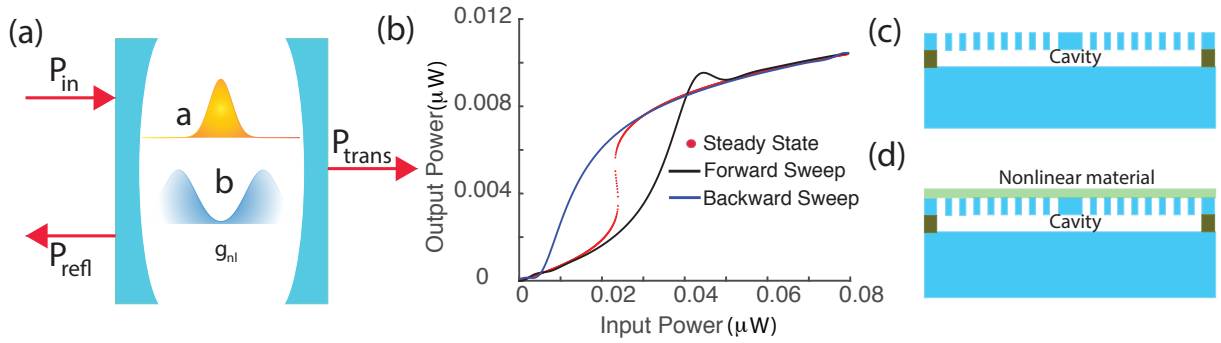

Figure 3.1: Schematics of a bistable nonlinear cavity system. (a) Our cavity system can be abstracted to a simple resonator with modes a and b that correspond to the fundamental and harmonic frequencies. We will assume such a cavity in our model so that we can forget the exact mode profiles and focus on the abstractions such as quality factor, input power, etc. (b) Bistable behavior of the cavity. The parameters for the simulation are: $g_{nl}/2\pi = 20$ GHz; $\kappa_{ta}/2\pi = \kappa_{ra}/2\pi = 3$ GHz and $\Delta_a/\kappa_a = 8$. Absorptive losses are ignored. (c) A potential cavity system where the cavity is made from the nonlinear matieral and (d) where the nonlinear material covers a linear cavity.

$$g_{nl} = D\epsilon_0\left(\frac{\omega_a}{2\epsilon_0}\right)\sqrt{\frac{\hbar\omega_b}{2\epsilon_0}}\int d\mathbf{r}\frac{\chi^{(2)}(\mathbf{r})}{[\epsilon(\mathbf{r})]^{3/2}}\alpha_a^2(\mathbf{r})\alpha_b(\mathbf{r}). \tag{3.2}$$

Where D is a degeneracy term that describes the number of terms in the $\chi^{(2)}$ tensor that participate in the interaction. α_a and α_b are the normalized electric field distributions (i.e. $\int |\alpha_{a,b}|^2 dr = 1$). Finally, ϵ and ϵ_0 refer to the permittivity and permittivity of free space, respectively. If we assume $D = 2$, and $\omega_b = 2\omega_a$, and there is a perfect overlap between the fundamental and harmonic modes we can find that:

$$\hbar g_{nl} = \epsilon_0\left(\frac{\hbar\omega_a}{\epsilon_0\epsilon_r}\right)^{3/2}\frac{\chi^{(2)}}{\sqrt{V_m}} \tag{3.3}$$

Where V_m refers to the effective mode volume of the device and is related to the normalized field distributions by: $1/\sqrt{V_m} = \int_{NL}\alpha^3(r)dr$. The subscripts on the integral indicate that it is to be taken over the volume occupied by the nonlinear material. Thus, the choice to construct the cavity out of a nonlinear material (as in Fig. 3.1c) or evanescently couple to the nonlinear material (as in Fig. 3.1d) has direct implications for the interaction strength.

While equation 3.1 provides a complete description of a closed system of a doubly resonant SHG cavity system, it does not provide a way to understand a lossy or externally driven system. To add the ability to externally drive our system with a laser we need to add an extra term: $\sqrt{2\kappa_{ra}}E(e^{-i\omega_l t}a + e^{i\omega_l t}a^\dagger)$. The laser frequency is taken to be ω_l and pumped at a rate κ_{ra} with an electric field amplitude E. This is somewhat simplified by realizing the laser frequency is much larger than the dynamics of our system, and so we can rewrite this as [35]:

$$H_{rot} = \hbar\Delta_a a^\dagger a + \hbar\Delta_b b^\dagger b + \hbar g_{nl}[b(a^\dagger)^2 + b^\dagger a^2] + E(a^\dagger + a). \tag{3.4}$$

In this formulation $\Delta_{a,b}$ are the detuning of the cavity modes from the driving laser frequency. To model the losses in the system, we need to use Linblad formalism. This requires us to now use density matrices, ρ, and to rewrite our master equation as:

$$\frac{d\rho}{dt} = -i[H_{rot}, \rho] + \sum_{i=a,b} \kappa_i[2A_i\rho A_i^\dagger - A_i^\dagger A_i\rho - \rho A_i^\dagger A_i]. \tag{3.5}$$

Here A_i is the annihilation operator for the selected mode (either a or b). In this model we will assume three different loss channels: reflection, transmission, and absorption. We have modeled each of these channels with an associated decay rate, namely, κ_r, κ_t and κ_a, respectively. The total loss of the system can then be written as $\kappa = \kappa_r + \kappa_t + \kappa_a$. We can arrive at the system's mean-field equations by using equations 3.4 and 3.5 along with the relation: $\frac{d\langle A_i\rangle}{dt} = Tr[A_i\frac{d\rho}{dt}]$.

$$\frac{d\langle a\rangle}{dt} = i\Delta_a\langle a\rangle - (\kappa_{ra} + \kappa_{ta} + \kappa_{la})\langle a\rangle - 2ig_{nl}\langle ba^\dagger\rangle + i\sqrt{2\kappa_{ra}}E, \tag{3.6}$$

$$\frac{d\langle b\rangle}{dt} = i\Delta_b\langle b\rangle - (\kappa_{rb} + \kappa_{tb} + \kappa_{lb})\langle b\rangle - ig_{nl}\langle a^2\rangle. \tag{3.7}$$

We have simplified the expressions by representing the expectation value of A_i by $\langle A_i\rangle$. At steady state we find:

$$\langle b\rangle = \frac{ig_{nl}\langle a\rangle^2}{i\Delta_b - (\kappa_{rb} + \kappa_{tb} + \kappa_{lb})}$$

Using this we can write the equation for $\langle a \rangle$ as:

$$i\Delta_a\langle a\rangle - (\kappa_{ra}+\kappa_{ta}+\kappa_{la})\langle a\rangle + \frac{2g_{nl}^2}{i\Delta_b-(\kappa_{rb}+\kappa_{tb}+\kappa_{lb})}\langle a\rangle^\dagger\langle a\rangle^2 + i\sqrt{2\kappa_{ra}}E = 0$$

Now if we take note that the intra-cavity photon number is given by $N_c = \langle a^\dagger a\rangle$, we can see that $P_{trans} = 2\kappa_{ta}\langle a^\dagger a\rangle$. Thus, our expression can be rewritten as:

$$i\Delta_a\langle a\rangle - \kappa_a\langle a\rangle + \frac{2g_{nl}^2}{i\Delta_b-\kappa_b}\frac{P_{trans}}{2\kappa_{ta}}\langle a\rangle + i\sqrt{2\kappa_{ra}}E = 0$$

We also note that $P_{in} = E^2$. Once we substitute this in we can finally arrive at an expression relating the transmitted power to the input power. To simplify our expression we will also define a parameter η as $\eta = g_{nl}^2/2\kappa_{ta}$. We will also assume that the quality factors of the two resonances are equal which means that $2\kappa_a = \kappa_b$. Finally, as long as $\omega_b = 2\omega_a$ it can be shown that in the rotating frame $\Delta_b = 2\Delta_a$ [70]. This means that $2(i\Delta_a - \kappa_a) = i\Delta_b - \kappa_b$, therefore:

$$\eta^2 P_{trans}^3 + 2\eta(\kappa_a^2-\Delta_a^2)P_{trans}^2 + (\Delta_a^2+\kappa_a^2)^2 P_{trans} = 4\kappa_{ta}\kappa_{ra}(\Delta_a^2+\kappa_a^2)P_{in},$$

The critical points are given by:

$$\frac{dP_{in}}{dP_{trans}} = 3\eta^2 P_{trans}^2 + 4\eta(\kappa_a^2-\Delta_a^2)P_{trans} + (\kappa_a^2+\Delta_a^2)^2 = 0$$

The system is bistable as long as $16\eta^2(\kappa_a^2-\Delta_a^2)^2 - 12\eta^2(\kappa_a^2+\Delta_a^2)^2 = 4\eta^2(\kappa_a^4+\Delta_a^4-14\kappa_a^2\Delta_a^2) > 0$. This condition can be simplified to the criteria: $|\Delta_a| < (2+\sqrt{3})\kappa_a$. The critical points are given by:

$$P_{trans}^{cr} = \frac{2(\Delta_a^2-\kappa_a^2) \pm \sqrt{\kappa_a^4+\Delta_a^4-14\kappa_a^2\Delta_a^2}}{3\eta} \tag{3.8}$$

These critical points are involved and provide little intuition. To qualitatively understand the system behavior, we assume lossless cavity with $\kappa_{ta} = \kappa_{ra} = \kappa_a/2$ and $\Delta_a >> \kappa_a$ and simplify the equation as:

$$\eta^2 P_{trans}^3 - 2\eta\Delta_a^2 P_{trans}^2 + \Delta_a^4 P_{trans} = \kappa_a^2\Delta_a^2 P_{in} \tag{3.9}$$

Here the critical points are the roots of:

$$3\eta^2 P_{trans}^2 - 4\eta\Delta_a^2 P_{trans} + \Delta_a^4 = 0$$

One thing that is interesting to observe is that the existence of bistability does not depend on the nonlinear coupling g_{nl}. This can be seen by inspecting equation 3.8 which indicates that g_{nl} only impacts the critical biasing point and the output power swing. It is also worth noting that these steady state equations give solutions with accurate values for the bias point and the output power swing, but fail to predict the hysteresis one sees in bistable systems. Fig. 3.1b shows how the solutions to the steady state equations compare to those of the numerically evaluated differential equations. Optical bistability is usually observed under large laser detuning such that $\Delta_a >> \kappa_a$. Under such detuning we can find that the critical points are at $P_{trans} = \Delta_a^2/\eta$ and $\Delta_a^2/3\eta$ corresponding to the input powers $P_{in} = 0$ and $4\Delta_a^4/27\eta\kappa_a^2$. The non-trivial solution gives an output power swing that scales with $\sim \kappa_a^2/\Delta_a^2$. One can also notice that the biasing point of the bistable system scales with $\sim \kappa_a^3/g_{nl}^2$ which in turn scales with $\sim V_m/Q^3$. This scaling places favor on high quality factor cavities over the usual V_m/Q scaling as seen in other bistable architectures such as those based on carrier injection or the thermo-optic effect [83]. It is also worth noting that this same scaling with Q has been reported for quantum limited frequency conversion efficiencies in triply (or doubly for degenerate cases like SHG) cavity systems [17].

3.2 Performance Analysis

With adequate models in hand and a general understanding of the device scaling we now look to understand the performance of the bistable device. Here we will consider the device under a constant photonic bias, P_{bias}. Our input signal is a small sinusoid at frequency Ω and with amplitude P_{amp}, atop the input bias, which in turn results in a periodic output as depicted in Fig. 3.2a. We first analyzed the gain, G, of our switch, which we define as the ratio of the amplitude of the output signal to the amplitude of the input signal. To this end, we have taken $\Delta_a/\kappa_a = 8$ and $\Omega/2\pi = 500$ MHz. The results of studying G as a function of P_{bias}

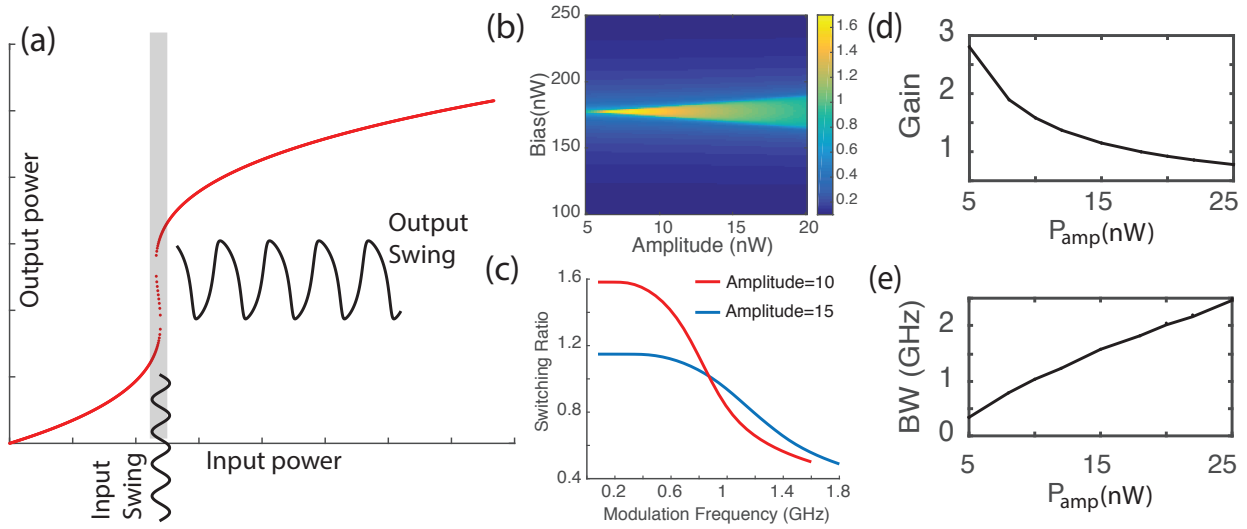

Figure 3.2: Performance of the bistable devices. (a) The steady state solution to our system showing its bistable nature. (b) The ratio of the input to output power as a function of amplitude and bias. (c) The frequency response demonstrating the bandwidth of system for two selected amplitudes. (d) Gain, defined as the switching ratio at a low frequency, (e) Bandwidth, defined at the 3 dB point, is plotted as a function of the P_{amp}. The parameters for the simulation are: $g_{nl}/2\pi = 20$ GHz; $\kappa_{ta}/2\pi = \kappa_{ra}/2\pi = 3$ GHz and $\Delta_a/\kappa_a = 8$.

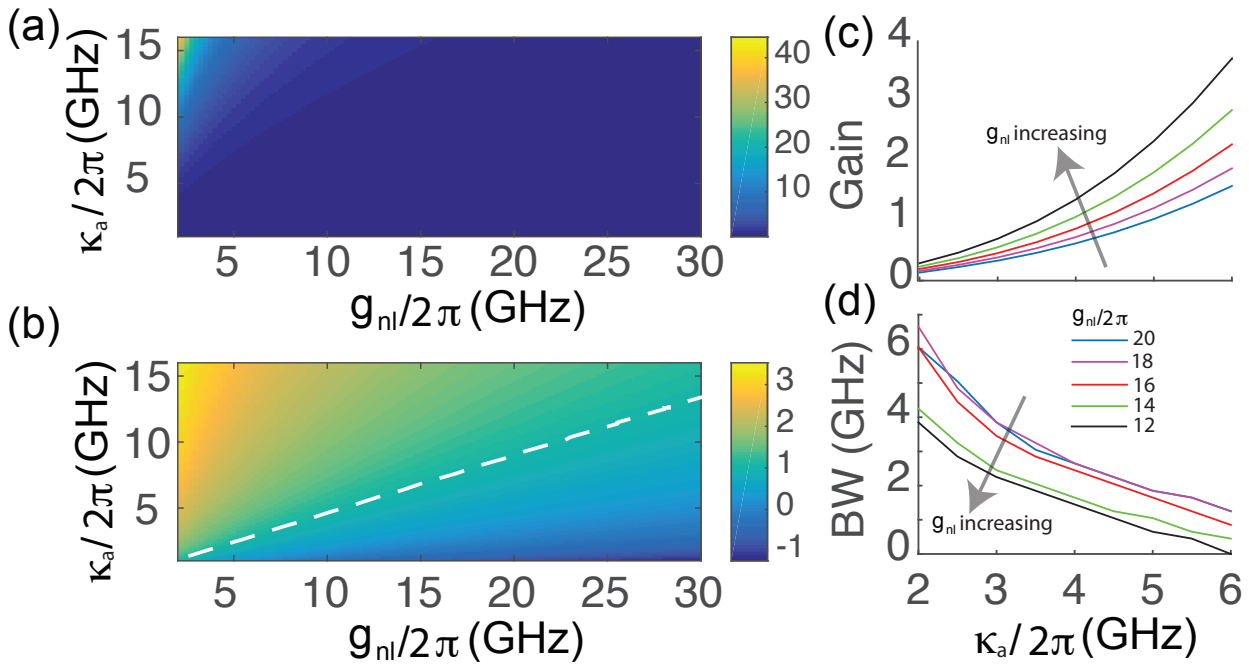

Figure 3.3: (a) The bias point P_{bias} as a function of the total linewidth $2\kappa_a$ and nonlinear interaction strength g_{nl}. (b) $log_{10}(N)$, N being the intra-cavity photon number plotted as a function of κ_a and g_{nl}. (c) Gain as a function of κ_a for different g_{nl}. (d) Bandwidth as a function of κ for different g_{nl}.

and P_{amp} are shown in Fig. 3.3b. There is a clear trend where G increases with decreasing P_{amp}. This is a consequence of the bistable nature of the device, as its output can only go between its two stable states. Thus, once the input signal has the amplitude needed to fully switch between the two states, further increasing the input signal results in decreasing gain. While it may be tempting to find the minimum P_{amp} required to fully switch between the two states in order to maximize gain, it is essential to avoid critical biasing [77]. That is, a good design will have a P_{amp} such that there is a range of P_{bias} that results in acceptable gain. If this is not the case then a small variation in P_{bias} will lead to the switch not fully switching between its two states, this in turn will reduce gain and distort the output signal. This need for a larger P_{amp} is also shown in Fig. 3.2b as the region of P_{bias} with appreciable gain decreases with decreasing P_{amp}.

Another important aspect of the bistable device is its frequency dependence. Of note is the modulation bandwidth of our device. We found that P_{amp} also plays a role in the bandwidth of the system. We have plotted the gain of the system for two different values of P_{amp} in Fig. 3.2c. For both cases, we find a bandwidth of near 1 GHz. Again, we notice that a larger P_{amp} results in reduced gain. Fig. 3.2d provides a more quantitive description of this behavior, showing that beyond a P_{amp} of approximately 20 nW the gain of the system drops below unity. Similarly the trend of increasing bandwidth as a function of P_{amp} is shown in Fig. 3.2e. The trends in the gain and the bandwidth of the system can be explained qualitatively by the gain-bandwidth product.

Until now, we have focused primarily on how external parameters influence the bistable system. A more complete understanding of the system entails exploring the effects of cavity loss and nonlinear coupling strength. First we explored the P_{bias} required to observe bistability as a function of the cavity loss rate and the nonlinear coupling strength as depicted in Fig. 3.3a. We then calculated what the intracavity photon number was for the same set of parameters as shown in Fig. 3.3b. The results here are as expected: having a high quality factor (low κ_a) and high nonlinearity (g_{nl}) is required to push the intra-cavity photon number to the single photon limit (below the dashed white line). We then explored how these parameters affect the gain and bandwidth of our bistable system. We find a clear trend of increasing gain with increasing κ_a (Fig. 3.3c). This can be explained by our previous expressions that show the gain increases proportionally to κ_a^2. As previously described, we should, and do, observe (Fig. 3.3d) a marked decrease of the bandwidth with increasing κ_a due to the gain-bandwidth product. This last portion is slightly surprising, as most bistable systems show significant bandwidth limitations due to the intra-cavity photon lifetime, and thus would show the opposite trend. The dependences for both the bandwidth and the gain on g_{nl} are indicated by the different colored line plots within each figure, along with an associated arrow indicating the dependence on increasing g_{nl}. Unsurprisingly, higher values of g_{nl} will cause higher gain and thus, lower bandwidth. This is typical of any system with a fixed gain-bandwidth product.

Since we are interested in the 10's of photons regime, we have plotted an extra dashed line in Fig. 3.3a to indicate what parameter sets grant us bistability in the few photon regime. We found that having a nonlinear interaction strength of $g_{nl}/2\pi = 20$ GHz, and loss rate $\kappa_a/2\pi = 10$ GHz is sufficient. For a wavelength of $\lambda = 1.55\ \mu m$ this entails a quality factor around 20,000, which is practical for dielectric cavities. In order to satisfy such a large coupling strength would require a mode volume on the order of a cubic wavelength ($V_m \approx (\lambda/n)^3$ where n is the refractive index of the cavity). It would also necessitate a $\chi^{(2)} \approx 5\ nm/V$, which is far larger than the susceptibilities available in traditional nonlinear materials such as GaAs. There is some hope that new materials such as topilogical insulators [116], or perovskites [114] might be able to provide such a nonlinearity. A more approachable solution would be to utilize a much higher quality cavity in order to loosen the requirements on the material nonlinearity. For instance, if we assume a cavity with a quality factor of nearly 200,000 we can then utilize a nonlinear coupling strength of only $g_{nl}/2\pi = 1$ GHz to reach the tens of photons level. Such a high quality factor is very difficult to achieve in a III-V platform but is well below the state of the art in silicon and other CMOS materials [100] [111].

3.3 Conclusion

We have presented a semiclassical derivation describing the bistability of $\chi^{(2)}$ cavity systems starting from the governing Hamiltonian. We were then able to show that such a nonlinear cavity can serve as an all-optical switch with bandwidths near 1 GHz with gain above unity. Our derivations also showed that bistability in these systems scale very strongly with the cavity quality factor, especially in comparison to other all-optical bistable cavity systems. Furthermore, we were able to show that with state of the art quality factors coupled with the ultra-high nonlinearities present in emergent material systems, we can achieve bistability in the few photon regime.

Chapter 4

SILICON CAVITY ENHANCED SHG FROM A TMD MONOLAYER

The previous chapters have laid out formalisms to understand and motivate experimental demonstrations of TMD based SHG devices. In this chapter we will cover the first experimental demonstration of SHG enhancement from the interaction of a wavelength scale dielectric cavity with a monolayer TMD flake. From previous chapters, we know that in doubly resonant systems the threshold of bistability and critical power for quantum limited frequency conversion scale as $V_m/(Q_f^2 Q_h)$ where Q_f and Q_h are the quality factors at the fundamental and harmonic frequencies, respectively. This scaling is based off the interplay between photons at the two resonances that are mediated by a nonlinear coupling term. For the case of a singly resonant system, the output power instead scales as $(Q/V_m)^2$ [76]. For this reason we chose to use a silicon photonic crystal cavity of the L3 variety, as they have been shown to have exceptional Q/V_m factors [100] [7]. In addition, there were plenty of high quality designs and well established etching recipes that allowed for expedient exploration of cavity enhanced SHG in a silicon photonic platform. Another advantage to using such a small mode volume is that a single exfoliated monolayer would cover the whole cavity. Exfoliated monolayers have edge lengths of only a few μm, and thus small mode volume devices are preferable.

4.1 Design of a wavelength scale dielectric cavity in silicon

The prominence of the silicon on insulator (SOI) photonics has lead to an abundance of high quality designs for large Q/V_m resonators. Here we used 220 nm silicon on oxide (SOI) wafer. Our L3 photonic crystal cavity had a periodicity (a) of 398 nm and a radius (r) of

116 nm. As previously reported by other authors, we adjusted the position by a value da and the radius of the holes by a value of dr nearest and in-line with the defect in order to maximize the quality factor of the resonator. Optimization was carried out by a particle swarm algorithm and resulted in $dx = 0.15a$ and $dr = 0.01a$. Modifying the holes at the ends of the linear defect is known to increase the quality factor as this can help reduce coupling to radiation modes [113].

4.2 Cavity Fabrication

The fabrication of the cavity followed standard microfabrication techniques. We started with a chip of 220 nm SOI (obtained from Soitec), which was prepped for lithography by baking on a hotplate at 300° C for 3 minutes in order to drive off excess wafer. We then spun 250 nm of ZEP 520A from Zeon Corp. Excess solvent in the ZEP was evaporated by another bake at 300° C for another 3 minutes. The resist was then exposed by a 100 kV JEOL JBX6300FS electron beam lithography system with a base dose of 125 $\mu C/cm^2$. The resist was then developed in Amyl Acetate for 2 minutes, along with gentle agitation to ensure the exposed resist was developed. The pattern was then transfered onto the silicon photonic layer by etching in an Oxford inductively coupled plasma (ICP) dry etcher with Chlorine based chemistry. The resist that was left over was then removed with sonication in dichloromethane (DCM). Finally, the silicon membrane was released by use of 1:10 buffered oxide etchant (BOE).

4.3 2D material preparation and transfer processes

In this thesis we have exclusively used exfoliated samples due to their high quality compared to the CVD grown materials. The primary advantage of the latter is the large area, up to the wafer scale [60]. Aside from the aforementioned quality difference, the polycrystaline nature of these monolayers make their use in SHG devices difficult, as differing crystal orientations can diminish the resulting SHG signal.

Samples are prepared by mechanical exfoliation, also known as the “Scotch Tape Method.”

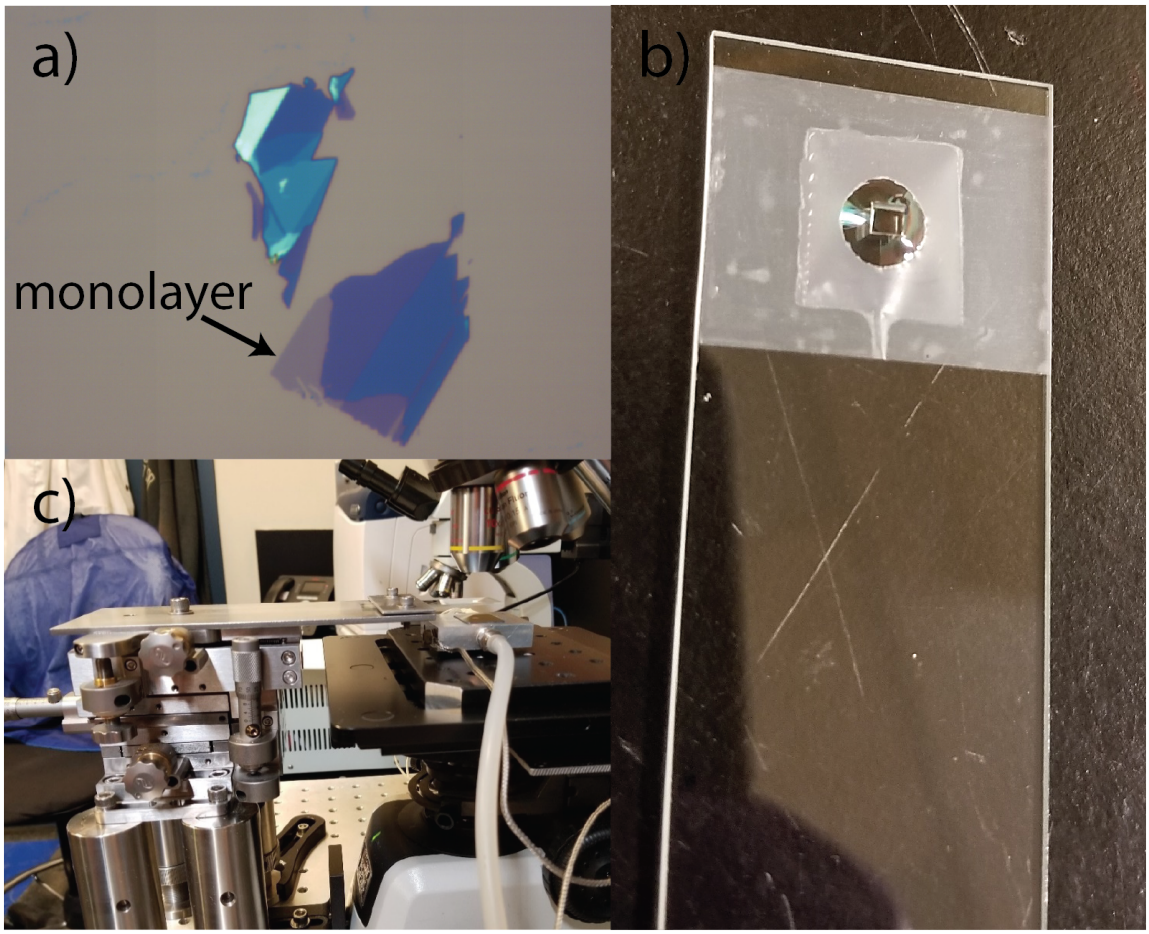

Figure 4.1: TMD transfer process. (a) Optical micrograph of exfoliated flakes. The arrow and "monolayer" label point to a monolayer of WSe_2 which appears light pink. Multilayer pieces are darker and are more blue in hue. In the limit of "bulk" samples the flakes begin to brighten and turn white as is the portion in the upper left corner. (b) Example transfer stamp. Here you can see the small square of PDMS on a glass slide with a thin layer of PC draped over it and held in place by a piece of Scotch tape with a hole in it. (c) Our 2D material transfer station. On the left is the five-axis stage that controls the position of the stamp. The stamp is held below a microscope to aid in alignment. Attached to the microscope stage is a temperature controlled vacuum stage that holds the sample in place and is used to vary the sample temperature.

A small piece of bulk crystal is placed on a piece of Scotch tape which is repeatedly pressed together in order to thin and redistribute the bulk material throughout the tape [81]. Unfortunately, there is a wide variety of available tapes, each providing a different level of exfoliation quality and degree of residue, which can only be determined through extensive experimentation. The tape is then pressed against a silicon wafer with either 95 nm or 285 nm thermal oxide layer. These two oxide thicknesses are optimal for searching for exfoliated 2D materials under a microscope, as they produce the largest contrast due to interference effects [13]. Individual monolayers can then be identified by their color and contrast with the substrate with the aid of a microscope (Fig. 4.1a). Verification of the monolayer nature can be confirmed with either photoluminescence (PL) [105] [60] [125] or atomic force microscopy (AFM) [81]. The latter also has the benefit of more reliably identifying how clean the material is, which is important for electron transport in heterostructures and coupling to photonic structures.

Once an appropriate flake is identified it can be moved onto an arbitrary substrate via a "dry transfer" method [117]. This name has historic origins. Namely, previous methods involved coating the monolayer with a thin film of PMMA and then removing a sacrificial layer of polyvinyl alcohol (PVA) or silicon dioxide with hydroflouric acid (HF), leaving a floating membrane with the flake that can be transfered onto any substrate using a "perfect loop" secured from Ted Pella. The main issue with these techniques is that the film is free standing and thus is hard to place with the micron, or better, accuracy required to make sophisticated structures consistently. In contrast, the dry transfer technique does not require a sacrificial layer and the polymer used to transfer materials , polycarbonate (PC), remains affixed to a PDMS stamp (Fig. 4.3b). The rigidity of the PDMS backing and the adhesion of the PC allows for heterostructures to be built up on a single stamp, then collectively deposited on any substrate, greatly enhancing the capability of researchers to build complex devices [37]. Alignment to 2D material samples and to the final device is accomplished by a combination of a multi-axis stage and a micromanipulator positioned with the sample and the stamp underneath a microscope (Fig. 4.3c). The stage in the microscope has been retrofitted

with a thermally isolated heating stage that is fitted with a resistive heating element and a thermocouple that are fed into a temperature controller. By raising the temperature of the stage, one can improve the adhesion of the PC to the monolayers. In addition, when releasing the samples onto the final device the stage is simply heated by the glass transition temperature of the PC film, which melts and releases it from the stamp. The layer of PC left on the chip is removed by placing the sample in chloroform overnight. Care must be taken with this last step as agitation can lead to material fly-off where the 2D material is also removed and the whole process must start again.

For our study of cavity enhancement, we decided to use WSe_2. This was primarily motivated by our desire to use a cavity with a resonance near the center of the telecommunications band at 1550 nm. This naturally implied the harmonic light would be centered near 775 nm. The $\chi^{(2)}$ value at any given wavelength is dependent on the proximity of the fundamental and harmonic frequencies to electronic resonances within the material [15]. In fact, resonances near the second harmonic frequency are known to greatly increase the SHG efficiency [101]. As WSe_2 has a room temperature band-gap close to 775 nm, it was an obvious choice. A scanning electron microscope (SEM) of our final device is displayed in Fig. 4.2a.

4.4 Linear Characterization of the Bare and 2D Material Clad PhC

In order to select a promising cavity, we measured our chip just after fabrication. Specifically, we used a cross polarization reflectivity setup (Fig. 4.3a) as previously reported [26]. As the name suggests, the light incident on the cavity is horizontally polarized and the vertically polarized light is collected. By placing the cavity at a 45° angle we are able to observe clear cavity reflection. This measurement is in essence using the L3 cavity as another intermediate polarizer, as the cavity modes are highly polarized, allowing for a reduced background and thus a high signal to noise ratios in reflectivity.

The selection criteria for the cavity were that the fundamental mode should have a high quality factor, and be resonant near 1550 nm. The cavity we chose had a fundamental mode with a quality factor just below 10,000 and a central wavelength of 1557 nm. After

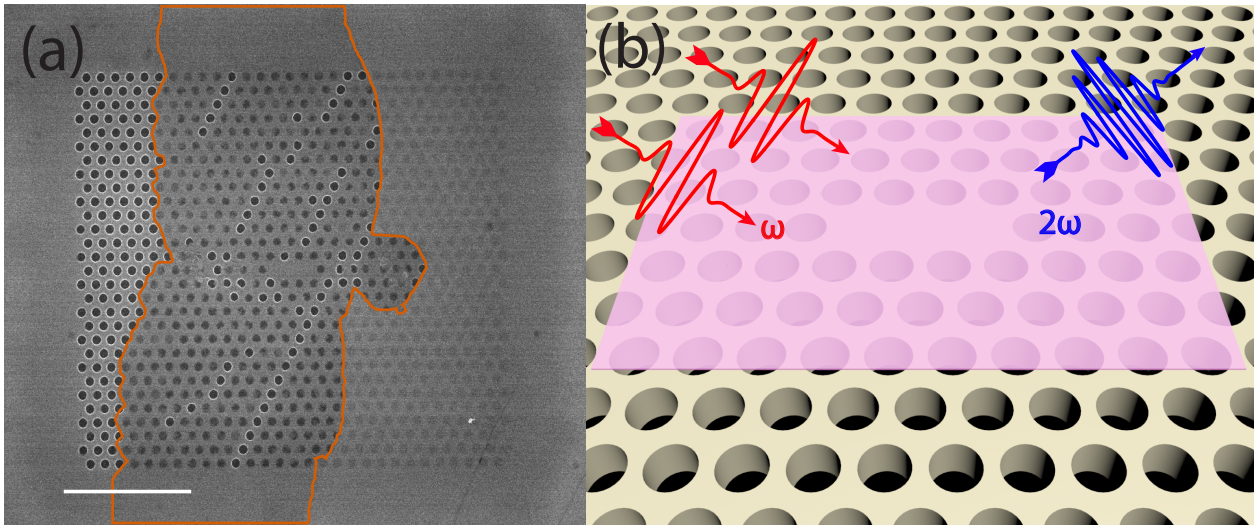

Figure 4.2: WSe_2 on a silicon photonic crystal cavity. (a) An SEM of the final device. Here we have outlined the monolayer WSe_2 in orange for clarity. The left portion of the crystal is bare and thus looks clear, while the mono- (center), and bi-layer (right) WSe_2 make the crystal look fuzzy. (b) A schematic of our experiment.

we transfered the monolayer WSe_2, we remeasured the cavity and found that we could no longer see the fundamental mode. In fact, prior to our transfer we were able to see several higher order modes with quality factors in the thousands (~2,000 - 3,000), but after transfer we were only able to find two modes with quality factors in the hundreds (~700 - 800) (Fig. 4.4). The large change in quality factor, and the apparent large wavelength shift of the cavity modes made it impossible to determine which modes were left and which were no longer visible. One issue is that we have found that PhC are much harder to probe once they have been capped with TMDs. A potential work around is to use the silicon defect PL to probe the cavity modes [102] [66], but this typically requires large powers due to the weak PL of silicon defects – far larger than would be required to destroy the WSe_2. To estimate the effect of integrating WSe_2 onto the PhCC we modeled the system with a finite-difference time-domain (FDTD) solver as implemented by Lumerical [1]. We simulated a 0.7 nm thick WSe_2 monolayer on top of the cavity. We used a non-uniform mesh, with the mesh size being 0.2 nm in the 2D material region and 40 nm in the photonic crystal. To improve the

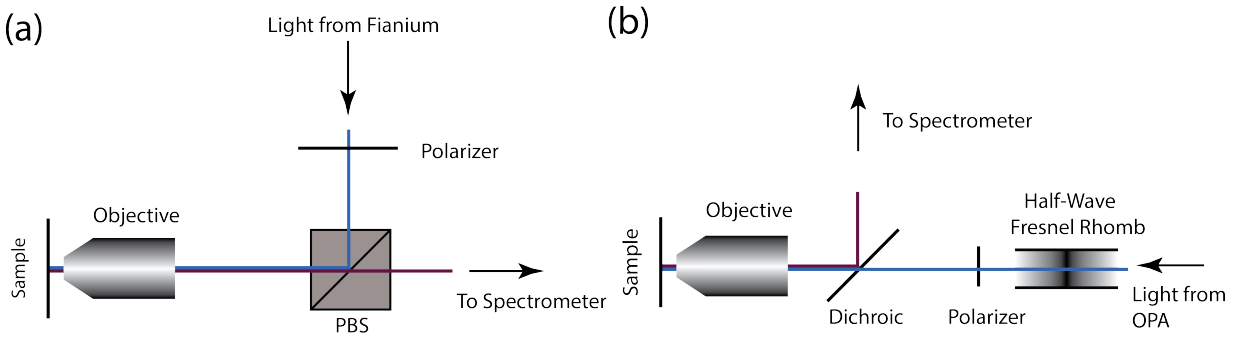

Figure 4.3: Optical measurement setups. (a) A schematic of the cross-polarized reflectivity setup used to measure the PhCC resonances. Note the polarizer in front of the polarizing beam splitter (PBS) which improves the degree of polarization incident on the sample. The light is focused down onto the sample which placed at a 45° angle with respect to the incident polarization. (b) The schematic for our SHG measurements. The light from the OPA was converted into circularly polarized light using a half-wave Fresnel rhomb. The light was then linearly polarized using a polarizer on a computer controlled rotation stage. The light was then focused onto the sample with an objective and redirected to the spectrometer by a dichroic.

simulation accuracy we used dielectric volume averaging for mesh refinement. The refractive index of the WSe_2 monolayer was taken to be n=4+0.1i near 1550 nm in accordance with previous measurements [65]. The quality factors were simulated to be 150,000 for the pristine cavity and 7,000 when clad with WSe_2. The additional degradation was likely due to strain induced on the floating membrane during the transfer and excess residue left on the cavity after the transfer.

4.5 Silicon PhC Enhanced SHG

To generate the SHG, we pumped the photonic crystal cavity with an optical parametric amplifier (OPA, Coherent OPA 9800) tuned to generate light near 1500 nm. The OPA was fed by a pump laser with a pulse width near 200 fs and with a repetition rate of 250 kHz. The light incident on the cavity was linearly polarized by a computer controlled polarizer (Fig. 4.3b). The light going into the polarizer was circularly polarized by a quarter-wave

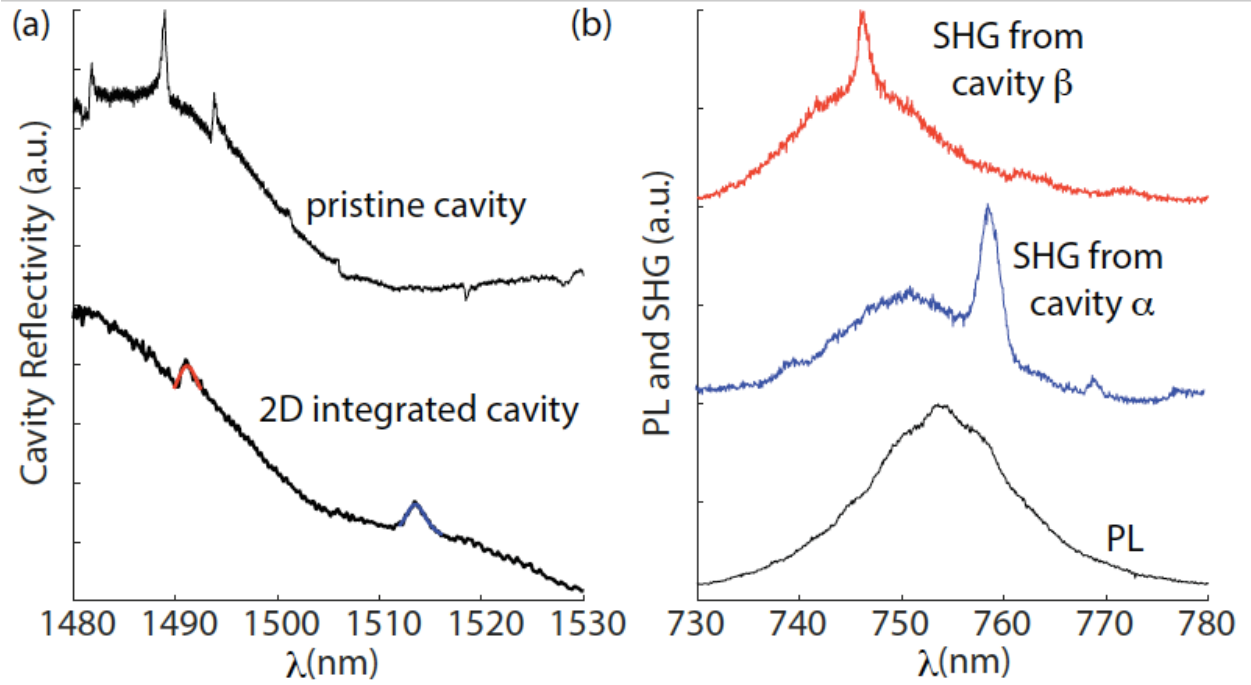

Figure 4.4: Analysis of cavity modes. (a) The cavity quality factors observed through cross reflectivity measurements showed significant degredation after the monolayer WSe_2 was transfered. (b) We were then able to observe each of the modes observed in reflectivity in the SHG signal. Due to the coincidence of the SHG energy with the band-gap of the material we performed additional studies to ensure that the effect we were seeing was not two-photon absorption induced PL.

Fresnel rhomb to ensure the rotation of the polarization did not induce a change in the incident power.

Bright light was observed near 750 nm when the sample was pumped. We took several steps to ensure that this radiation was SHG originating from our WSe_2 flake. First we ensured that the signal only appears when exciting the monolayer, which was used to check that the WSe_2 was the origin of the observed light. It is well known that material interfaces give rise to surface nonlinearities [15] that have previously been used in SHG devices [61]. We found no appreciable light near 750 nm coming from the silicon-air interface when we pumped away from the monolayer. While it is possible that the interfaces on either side of the monolayer could be contributing to the observed light, we did not investigate this as a possibility as other authors have found those effects to be negligible [48]. Polarization resolved SHG of TMDs result in a signature six-fold pattern that is often used to prove the origins of the SHG [101]. We were unable to use such techniques here due to the linear polarization of the cavity modes.Finally, we had to check that the observed signal was indeed SHG and not two-photon absorption (TPA) induced PL. To this end we tuned the OPA and noticed that the frequency of light shifted in response, eliminating TPA PL as a potential source. This is illustrated in Fig. 4.4b where we can see a clear shift in central wavelength between the background SHG (top and middle plot) compared to the central wavelength of the PL spectrum where the WSe_2 was excited with a HeNe laser.

With a certain confidence that we were observing SHG, we moved on to investigate the two Lorentzian peaks in the SHG spectra in Fig. 4.4b. By fitting the curves (Fig. 4.5a), we were able to find that the central wavelengths of these two peaks were at ~745 nm and ~758 nm, which is exactly half of the wavelengths of the two peaks found in the reflection measurements, which were at ~1490 nm and ~1515 nm, respectively. Here we will take to calling the mode at ~1515 nm as mode "α" and the mode at ~1490 nm as mode "β". We also observed that the linewidth of the cavities α and β in SHG were half of those found in reflection, as expected for cavity enhanced SHG. To confirm that these features were coming from cavity enhancement we studied the polarization dependence (Fig. 4.5b). We found

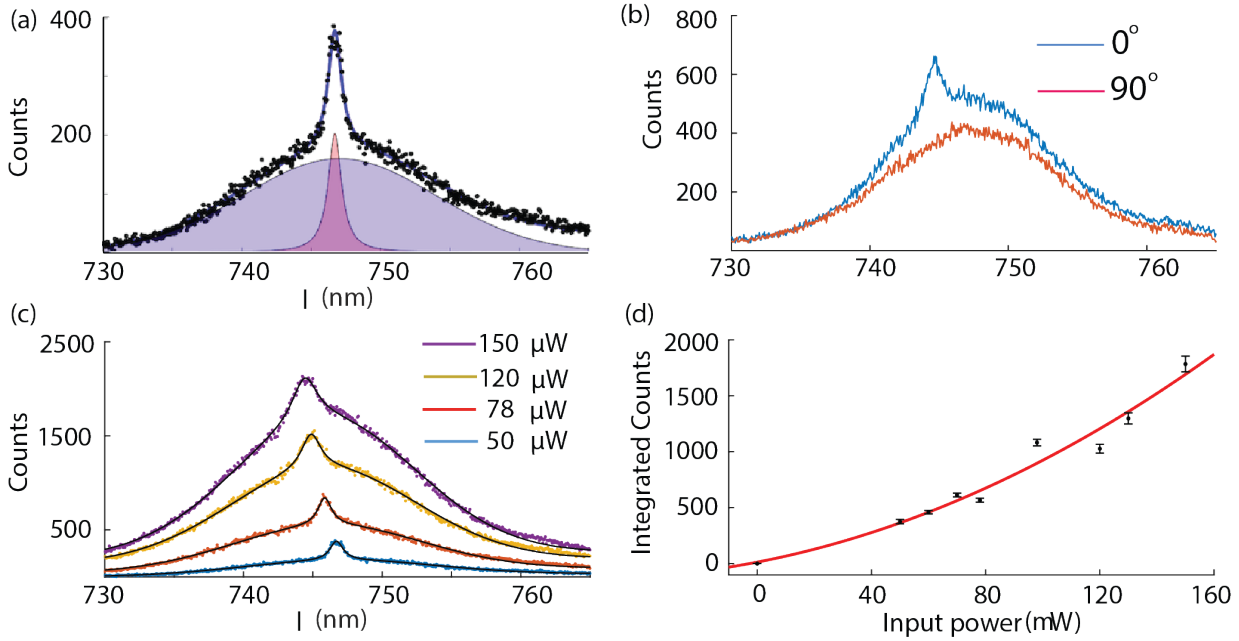

Figure 4.5: Investigation of cavity enhanced SHG. (a) Cavity contributions were separated by fitting a linear combination of Lorentzian and Guassian terms. (b) The cavity enhanced SHG is heavily linearly polarized along the cavity polarization axis. (c) We conducted a power series and confirmed that the (d) cavity enhancements scaled quadratically as expected of SHG.

the Lorentzian shaped SHG signal to be very polarization sensitive, disappearing when the incident polarization was orthogonal to the cavity polarization.

Finally, we performed a power series on the the cavity modes shown. The results for cavity β are shown in Figs. 4.5c and d. Similar results were found for cavity α, so we will not discuss them here to avoid redundancy. We then extracted the cavity enhancements as outline previously, and showed that the cavity enhanced SHG scaled quadratically, as expected (Fig. 4.5d).

We further analyzed this data to extract the cavity enhancement factor. We first estimated what percentage of the incident light coupled to the cavity mode. We took the spot size of the incident beam to be approximately 5 μm on radius. Using the simulated intensity profile of cavity mode β, we were able to find the total modal overlap and thus, the coupling

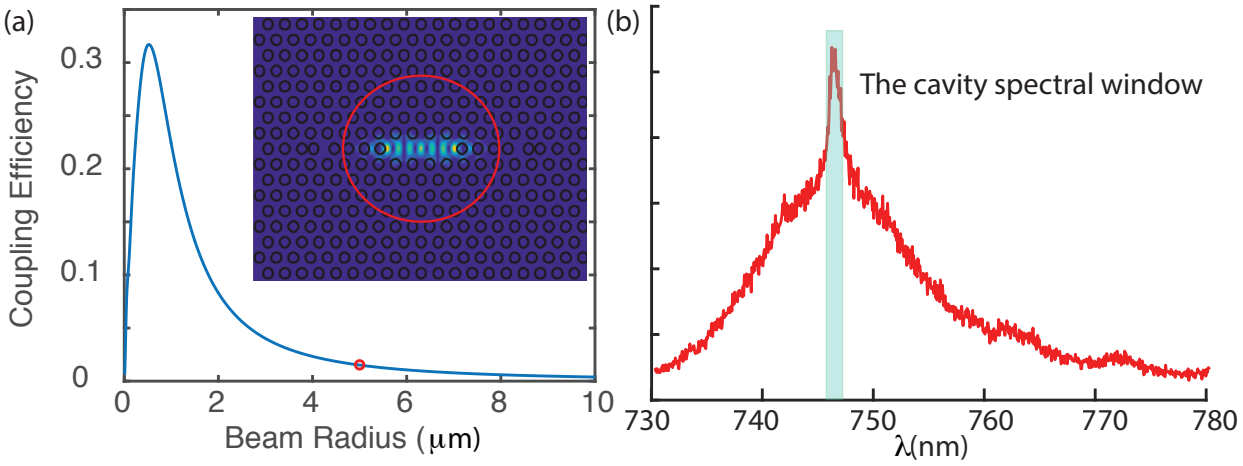

Figure 4.6: Calculating the total cavity enhancement. (a) Calculation of the coupling efficiency of the input beam to the PhC. We found that our beam spot was approximately 5 μm on the radius giving a coupling efficiency of 1%. The inset shows a plot of the cavity intensity profile for mode β with the red circle indicating the size of the input beam. (b) In order to calculate the total cavity enhancement we also calculated the ratio of light inside the Lorentzian compared to the Gaussian background over the cavity spectral window as indicated by the blue highlight.

efficiency (Fig. 4.6a). As the background SHG is much broader than the cavity linewidth, we also had to select out the cavity contribution compared to the background. To quantify the cavity enhancement we took the power under the the Lorentzian curve within our cavity spectral window, taken to be the cavity full width half maximum. By combining these factors and comparing them to the Gaussian background within the same spectral window, we found that our cavity had an enhancement factor of nearly 400. This is over an order of magnitude larger than the previous report of cavity enhanced SHG in a distributed Bragg reflector (DBR) cavity [23], which we attribute to our lower mode volumes and higher quality factors.

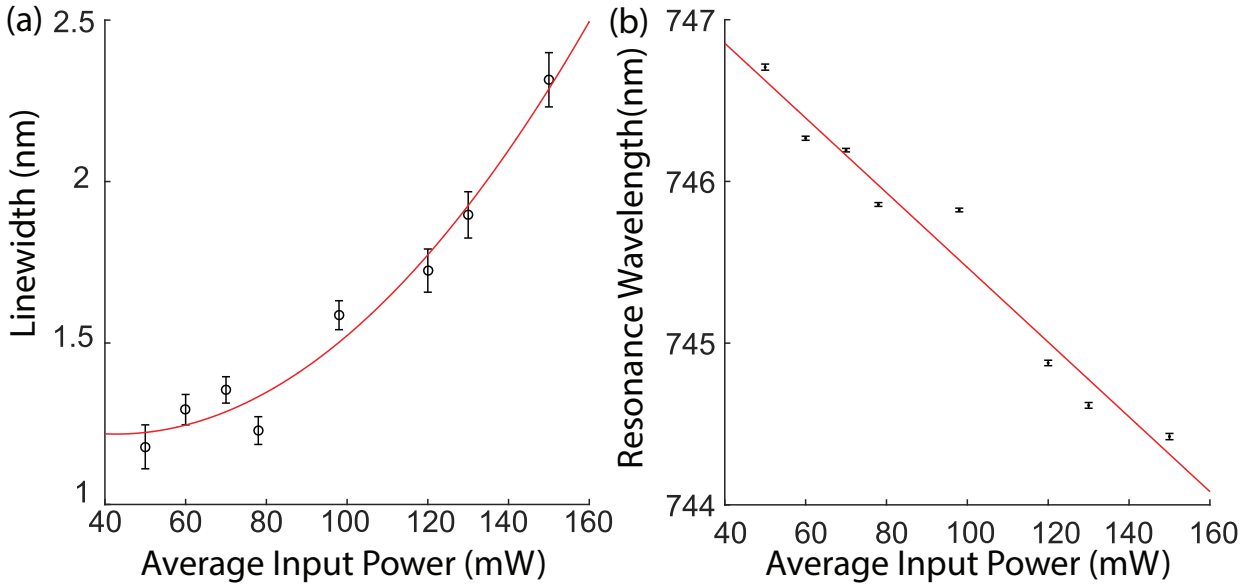

Figure 4.7: Effects of TPA generated free carriers on cavity mode β's (a) linewidth, and (b) central wavelength.

4.6 Free Carrier Effects in the Silicon PhC

Cursory inspection of the power dependence in Fig. 4.5c will reveal an trend of increasing linewidth and blue shifting with higher incident power. By fitting this data we have extracted the change in linewidth and resonance wavelength and plotted the results in Fig. 4.7a and b, respectively. We attribute these effects to TPA of our excitation beam in the silicon slab. To qualitatively explain these behaviors, we will look at the phenomenological equations for the change in refractive index (n) and absorption (α) for silicon at 1550 nm as a function of a change in electron (ΔN) and hole (ΔP) density [91]:

$$\begin{aligned} \Delta n_{1550\ nm} &= -8.8 \times 10^{-22}\Delta N - 8.5 \times 10^{-18}\Delta P^{0.8} \\ \Delta \alpha_{1550\ nm} &= 6 \times 10^{18}\Delta N + 4 \times 10^{-18}\Delta P\ [cm^{-1}] \end{aligned} \tag{4.1}$$

We can see that as the free carrier concentrations are increased, we would expect a decrease in refractive index, which would lead to a blue-shift in cavity resonance and an

increase in absorption, which would lead to cavity broadening. As TPA scales quadratically with power, we would expect a quadratic increase in free carrier density. Since there is a linear (or very close to) relationship between the change in refractive index/absorption with change in free carrier density we would expect there to be an overall quadratic relationship between input power and cavity shift as well as cavity broadening. From Fig. 4.7a we can see the latter holds well. However, the former (depicted in Fig. 4.7b) shows a decrease in resonance wavelength, as expected, but the trend is linear rather than quadratic. We expect that the TPA was creating excess heat, which caused a red-shift that counteracted the blue-shift caused by the free carrier effect.

4.7 Conclusion

We demonstrated the enhancement of SHG from a monolayer flake of WSe_2 coupled to a wavelength scale resonator. Due to the moderate quality factors and low mode volumes, we were able to demonstrate a 400-fold enhancement of the SHG. More importantly this study shows that WSe_2 is an interesting material for future studies of SHG enhancement via dielectric resonators.

Chapter 5

DEVELOPMENT OF A SILICON NITRIDE PLATFORM

While our experiment on cavity enhanced SHG from a silicon photonic crystal cavity demonstrated the efficacy of our hybrid photonic platform, the experiment had a number of flaws. The most obvious of these is that our photonic platform was in silicon, which strongly absorbs the SHG light. Fortunately, we have another alternative, even within the CMOS compatible materials: silicon nitride. Unlike silicon, silicon nitride is an insulator with a wide bandgap of nearly 5 eV [47], making it transparent in both the near infrared (NIR). Furthermore, silicon nitride has a refractive index of ~2 across the visible and NIR regions [68], compared to silicon dioxide with a refractive index of ~1.5 across the same range [73]. This allows silicon nitride to serve as a photonic layer even when on or encapsulated by silicon dioxide.

Another pitfall of our system was that the PhC was on a suspended membrane. Floating membranes present a serious challenge for hybrid integrated photonics. The foremost is the mechanical instability they cause. These membranes are easily destroyed by external pressures, such as those used when transferring material onto a cavity. Fig. 5.1a shows a micrograph of gallium phosphide (GaP) cavities that were used to explore cavity coupling to the excitons and single defects in WSe_2. There are readily visible broken membranes in devices such as device R5C1 (the device in the upper left corner), which have a dark discoloration. Such devices have cracked membranes, resulting in portions of the cavity which sag, and thus appear darkened. In fact, this frailty was used in our cavity enhanced LED paper [64] as we were able to break the cavity off of the substrate and transfer it onto a WSe_2 LED by the same transfer process used to transfer the materials themselves. Other issues with floating membranes include cavity detuning via strain induced from termperature

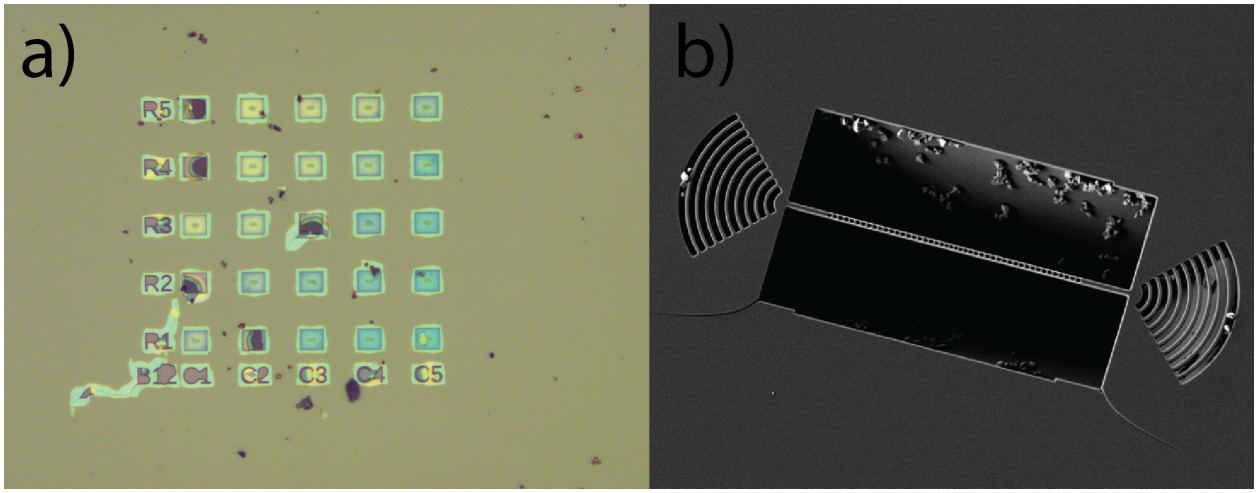

Figure 5.1: Two common photonic crystal designs. (a) Floating L3 cavities in GaP. The lighter shade of orange is where the cavities

shifts or transfer processes, which can make spectral alignment with the defects or excitons difficult.

An underlying problem with moving to a silicon nitride platform is that while we can solve the first problem, there were no good solutions to the second. The available demonstrations of 2D PhC cavities were both floating and of relatively high mode volume and low quality factor (~100s to ~1,000s) [10] [74] [9]. The underlying problem is with the low refractive index of silicon nitride, which is common to other photonic platforms such as silicon dioxide or polymer PhCs [10] [53] [75]. The common solution to achieve higher quality factors is to instead use nanobeam cavities, which allow one to achieve much higher quality factors in both simulation and experiments [52] [22]. However, these nanobeams are also floating and usually look like the nanobeam shown in Fig. 5.1b. With such cavities, not only do we have the aforementioned problems of mechanical stability, but we also have potential issues with monolayers wrapping around the beam and onto themselves or floating off during PC removal. Our solution was to design a nanobeam cavity that worked when surrounded by silicon dioxide [29].

5.1 Design

In order to form a cavity, we first needed to design a unit cell with bands below the light cone. This was accomplished with the use of MIT Photonic Bands [51] software suite, which was used to simulate the bandstructures of our unit cell. The main goal, and the primary difficulty, was to find such a design that used a silicon nitride (n~2) nanobeam on a silicon dioxide (n~1.5) substrate. From a design perspective, this meant we could have the silicon nitride on silicon dioxide or silicon nitride surrounded by silicon dioxide. As asymmetry imposes extra difficulty with confining bands, we opted for the latter. Most nanobeam designs revolve around circular holes, but here we used elliptical holes. This was primarily due to the inability to push bands below the light cone with circular holes. The extra degree of freedom allowed for confining bands below the light cone and is in-line with previous reports that have simulated designs for silicon nitride on silicon dioxide nanobeam [84]. By optimizing the period, major and minor radii, and the beam width, we were able to confine two bands (Fig. 5.2a). The lower energy band is a dielectric band and the higher energy band is an air mode band. In our final design we had a beam thickness of 330 nm, a beam width of 450 nm, and a period of 233 nm. The major and minor diameters of the elliptical holes were 300 nm and 100 nm, respectively.

With a suitable band structure in hand, we turned to creating the defect to form a cavity. We elected to use a linear tapering of both the major radius and the period (Fig. 5.2 b) in the central portion of the nanobeam. Using a particle swarm optimization scheme, we found that a cavity length of 115 nm, an inner period of 222 nm, and an inner major radius of 140 nm gave the highest quality factor. With 40 Bragg periods on each side, we found a maximal quality factor of $Q \approx 100,000$ and a mode volume of $V_m \approx 2.5(\frac{\lambda}{n})^3$, which could not be improved by adding further Bragg sections. A plot of the confined mode is depicted in the lower portion of Fig. 5.2 b. This large number of Bragg periods was reduced to 20 per side in order to reduce the footprint of the cavity, allowing the entire structure to fall within the field of view of our microscope. This limited the quality factor to ~15,000.

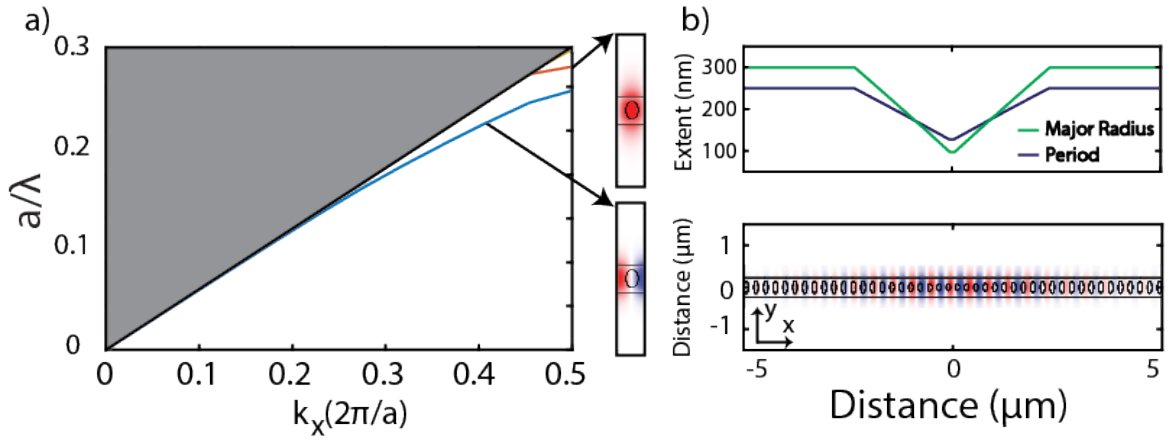

Figure 5.2: Design of the encapsulated silicon nitride nanobeam. (a) By using elliptical holes two band, and air-mode and dieletric-mode as shown in the insets, were confined. (b) We then used a linear tapering scheme on the major radius and the periodicity to form our cavity.

5.2 Fabrication

We started with a wafer with 330 nm of stoichiometric silicon nitride on 4 μm of BOX on a silicon handle obtained through Rogue Valley Microdevices. The silicon nitride was grown via low pressure chemical vapor deposition (LPCVD). The thickness and refractive index of the silicon nitride were measured by ellipsometry to ensure they conformed to our design. The chips were initially cleaned in a barrel asher with oxygen plasma excited with an RF power of 150 W for a duration of 5 minutes. We found this step to be critical for resist adhesion to the substrate. 400 nm of ZEP 520A from Zeon Corp was then spun on the chips. This was done within 30 minutes of ashing to prevent the SiN surface from absorbing too much water vapor, which in turn reduces ZEP adhesion. The ZEP was then coated with a thin Pt/Au film with a SEM sputtering system in order to avoid charging effects while writing. The resist was then exposed by a 100 kV JEOL JBX6300FS electron beam lithography system with a base dose of 125 $\mu C/cm^2$. The charging layer was removed by submerging the gold etchant for one minute. The resist was then developed in amyl acetate

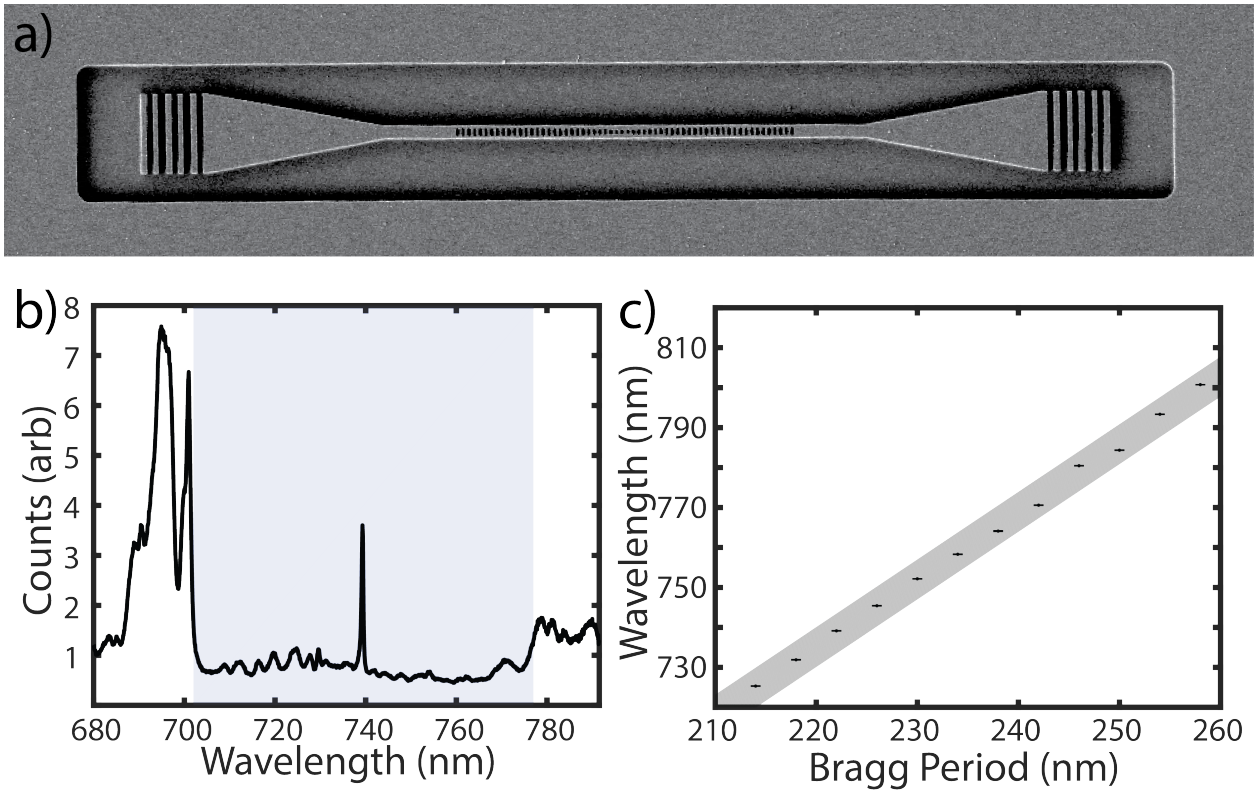

Figure 5.3: Measurement of fabricated cavities. (a) SEM of the fabricated cavity with a pair of grating couplers on either side. (b) An example transmission spectra as measured through the grating couplers. (c) We observed linear scaling of the cavity wavelength as a function of the periodicity.

for three minutes with gentle agitation. The pattern was transfered onto the SiN by a RIE etch in CHF_3/O_2 chemistry. Finally, the excess resist was removed with sonication in a DCM bath.

5.3 Characterization

After fabrication, we were able to confirm cavity resonances through a number of means. We first ensured that the fabricated devices were of similar dimensions to the design parameters through the use of a SEM (Fig. 5.3a). Next we looked for a transmission spectrum that resembled the expected spectrum: a narrow peak in the center of a low transmission region.

We spun a thick layer of PMMA on the chip for the cladding layer. This is preferable to using a silicon dioxide cladding, as PMMA has a refractive index similar to silicon dioxide [11], but can easily be removed without risk to the nanobeam. This allows for several cycles of material transfer and measurements with a single chip. The nanobeam was addressed through the attached grating couplers, one of which was pumped with a supercontinuum source (Fianium WhiteLase Micro) in the same setup we used to measure the photonic crystals (Fig. 4.3a). Light from the other grating was collected and sent to a spectrometer ((Princeton Instruments PIXIS CCD with an IsoPlane SCT-320 Imaging Spectrograph), which showed narrow linewidth features in the middle of a low transmission region, as expected (Fig. 5.3b). The finest grating used in our experiment is 1200 mm^1 blazed for 750 nm with an estimated resolution of ~0.06 nm. We did not have a tunable laser to measure the transmission of the nanobeams. Instead, we normalized the transmission of the cavity spectra to that of a bare waveguide.Finally, by comparing several spectra from nanobeams with increasing periodicity we were able to observe the linear scaling expected of resonances (Fig. 5.3c). The quality factor of these resonances were between 1,500-7,000. We attribute the one order of magnitude decrease in quality factor due to fabrication imperfections.

We then studied the effects of transferring a monolayer of WSe_2 onto our cavities. Having measured our cavities, we picked two for further study, one with a resonance in the spectral range of the defects found in WSe_2, named device 1, and another within the excitonic wavelength range, named device 2. We first stripped the encapsulating PMMA from atop our cavities using DCM. We then used the dry transfer techniques outlined in section 4.3 to transfer monolayer WSe_2 onto each cavity. To avoid the perils of the 2D material from lifting off, we kept the PC layer that was transfered with the monolayers. To ensure proper encapsulation we then spun an additional layer of PMMA. Comparison of the transmission spectra for device 1 and 2 before (Fig. 5.4c,d) and after (Fig. 5.4e,f) revealed that an additional mode appeared for both devices. We were able to replicate this appearance in FDTD simulations by encapsulating the cavities with a material with refractive index of 1.57, the refractive index of PC [108]. This was further confirmed with a study done with another

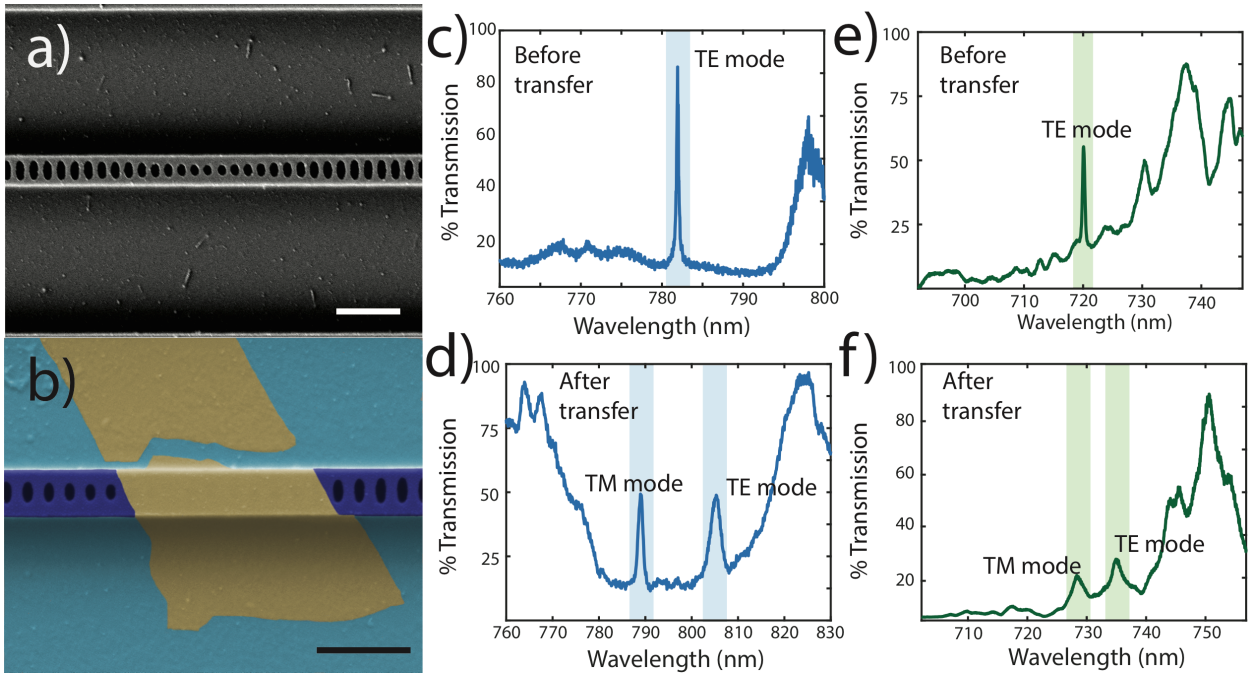

Figure 5.4: Effects of transferring monolayer WSe_2 onto the silicon nitride nanobeams. (a) SEM of a nanobeam before and (b) after transfer. We have colorized the SEM for clarity. The light blue is the silicon dioxide substrate, dark blue the nanobeam, and the monolayer is gold colored. Transmission spectrum of the first nanobeam, named device 1 before (c) and after (d) the transfer, and similarly for device 2 (e), and (f), respectively.

set of identical nanobeams. These nanobeams were coated and measured with PMMA, then stripped, coated with PC, and remeasured. Several cycles of this showed this new mode was solely the result of the higher refractive index of PC (Fig. 5.8). Our simulations also showed that the original mode is the lower energy mode and is TE polarized, while the new mode is of higher energy and is TM polarized (Figs. 5.5, 5.6, and 5.7).

5.4 Cavity Enhanced PL

Finally, we demonstrated the ability to use these photonic structures to couple to the photoluminescence of the monolayer WSe_2. We directly excited the monolayers from the top using a 532 nm continuous-wave laser while the samples were cooled to 80 K. By using a

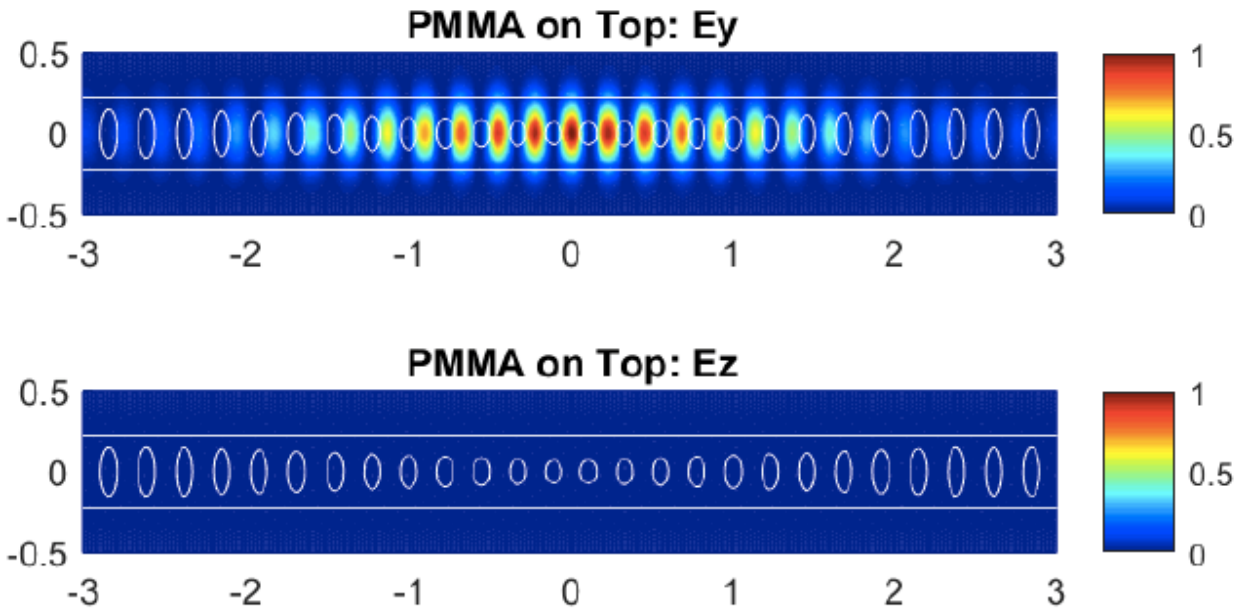

Figure 5.5: The field profile of the fundamental, and only mode when the encapsulated nanobeam has PMMA cladding.

confocal microscope setup, we were able to isolate the light coupled out by the grating couplers. We were able to observe Lorentzian lineshapes in both devices 1 and 2 (Fig. 5.9 a,b) with linewidths and central wavlengths matching the modes found in transmission (Fig. 5.4 d,f). As expected, the PL from device 2 only coupled to the TE mode, as the exciton has an in-plane dipole moment [99]. However, the PL coupled mode in device 2 was the TM polarized mode. The defects in WSe_2 are also known to have an in-plane dipole moment [43]. Here the wrapping of the monolayer onto the sides of the nanobeam likely allowed the defect dipole to align itself with the cavity mode, facilitating the coupling between them. By fitting a Lorentzian curve to the cavity peaks in the PL spectrum, we find Q-factors of 830 and 320 for device 1 and 2 respectively. These linewidths agree with the linewidths observed in transmission.

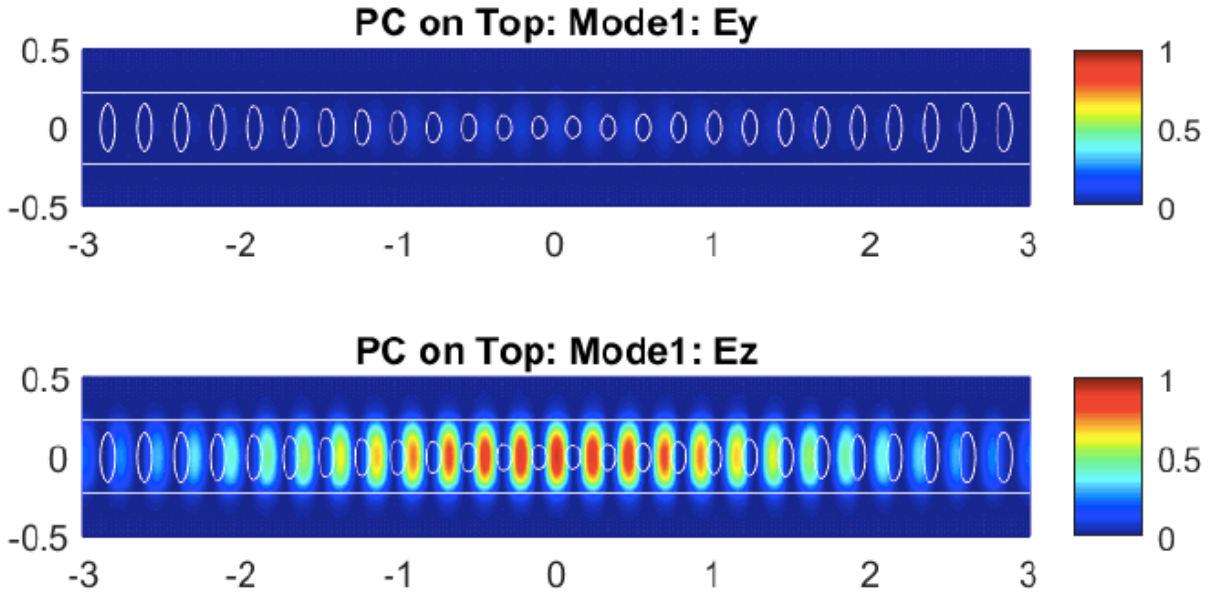

Figure 5.6: The field profile of the higher energy mode when the encapsulated nanobeam has PC cladding.

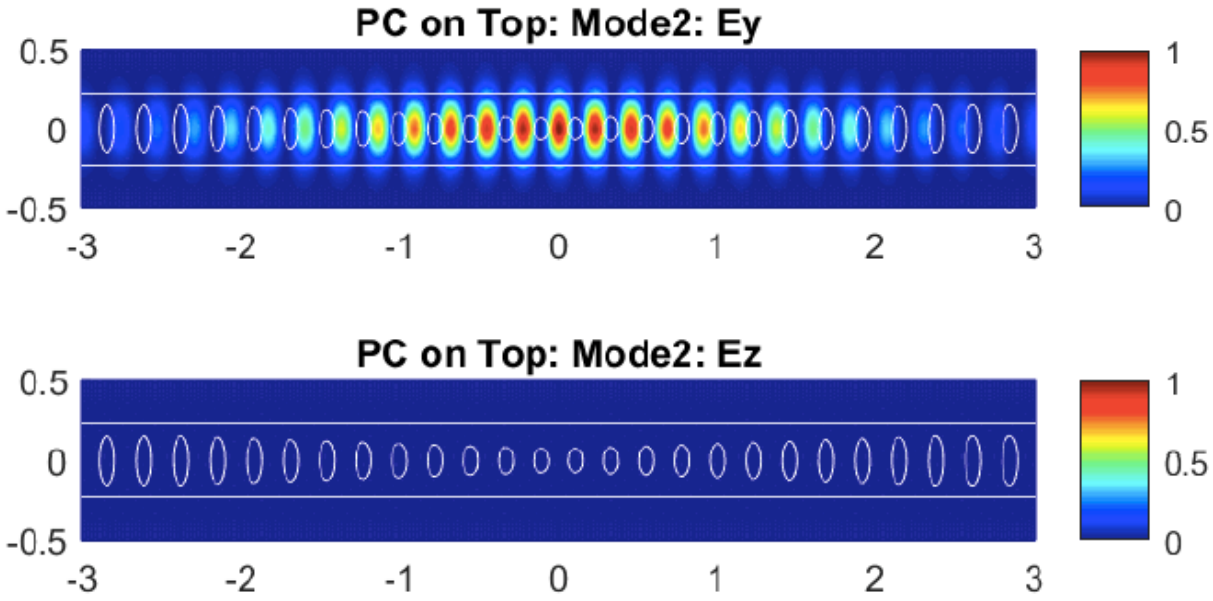

Figure 5.7: The field profile of the fundamental mode when the encapsulated nanobeam has PC cladding.

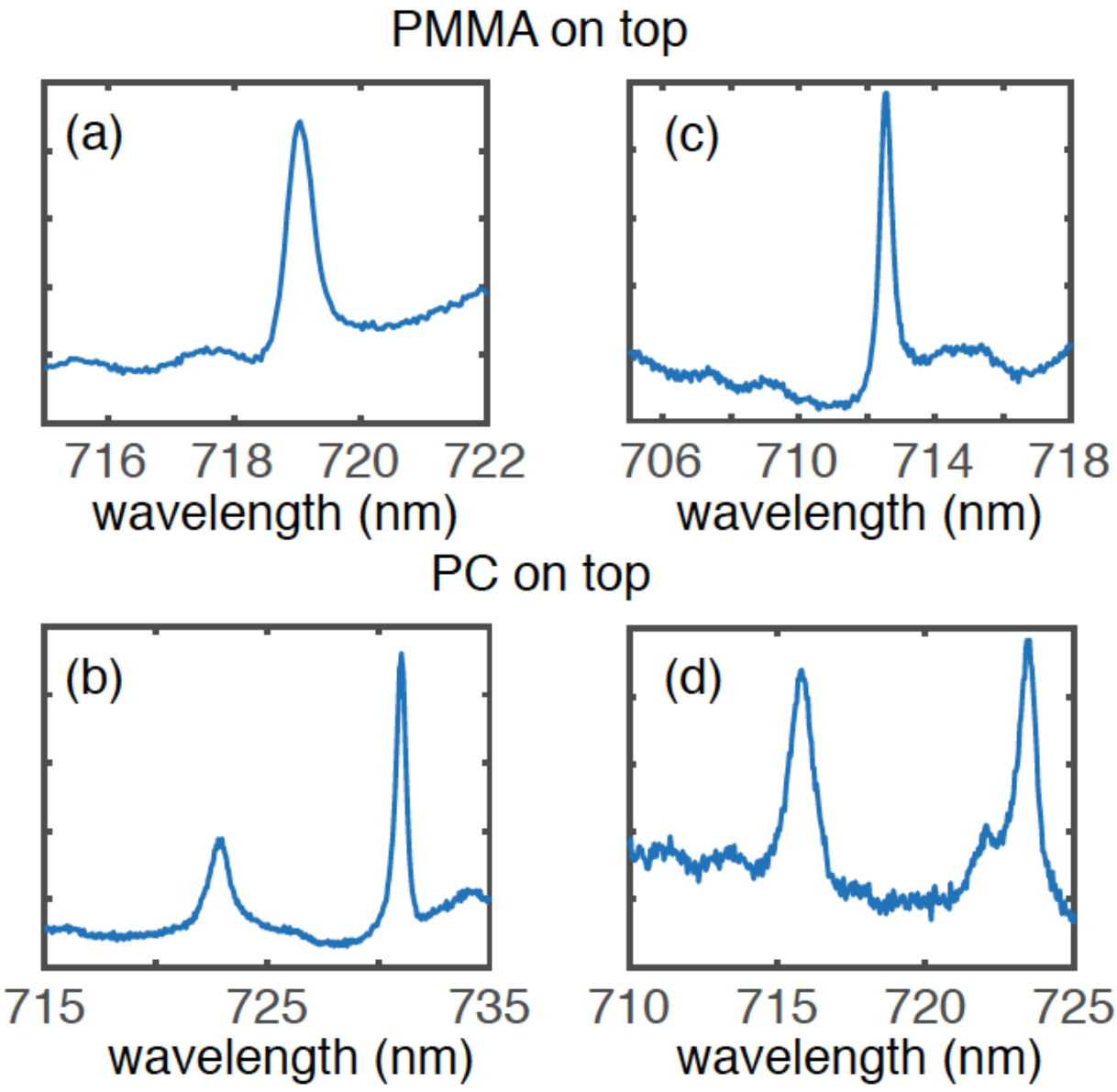

Figure 5.8: Investigation of the effects of cladding material on the spectra of fabricated devices. (a) and (c) show two separate devices similar to the ones shown in Fig. 5.4. The spectra are with PMMA cladding. (b) and (d) show the same cavities as (a) and (c), respectively, but with PC cladding.

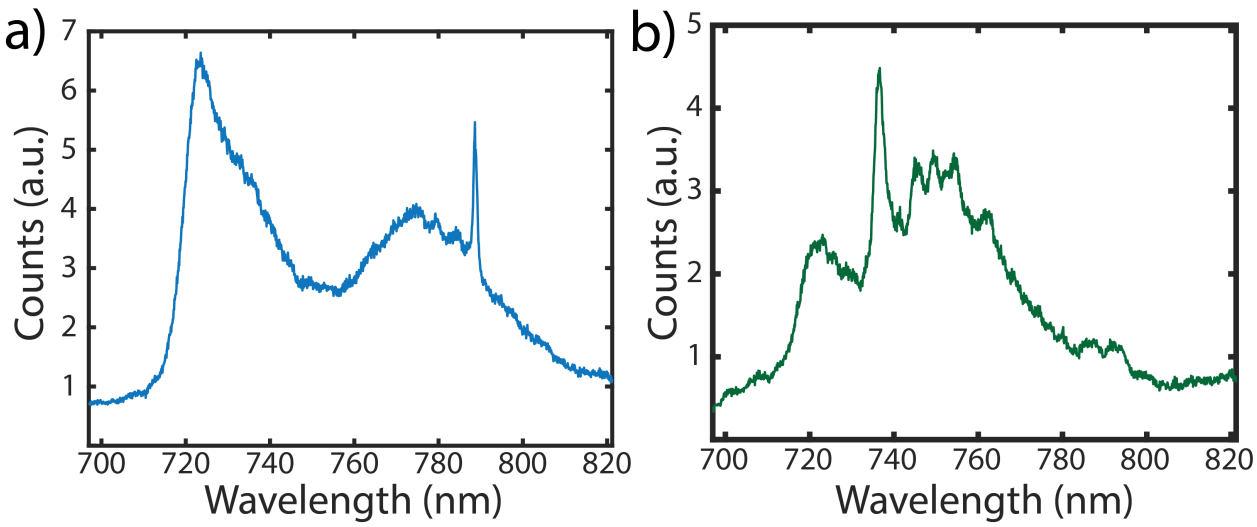

Figure 5.9: Photoluminescence of devices (a) 1 and (b) 2.

5.5 Nanobeams in the Telecommunications Band

Another important wavelength for 2D materials and photonics is the telecommunication band (near 1550 nm). By scaling our design for 750 nm to telecommunication wavelengths we found a suitable design for SiN encapsulated nanobeam resonator. Our devices show excellent rejection of light within the band-gap of the photonic crystal with the exception of a lone cavity peak (Figure 5.10). By fitting a Lorentzian function to the cavity peak we find that a typical device has a quality factor around 10,000.

5.6 Conclusion

This was the first demonstration of an encapsulated silicon nitride nanobeam to the best of our knowledge and represents an important step towards a 2D material hybrid platform. We have demonstrated that these nanobeams are capable of coupling to and enhancing the emission from TMDs.

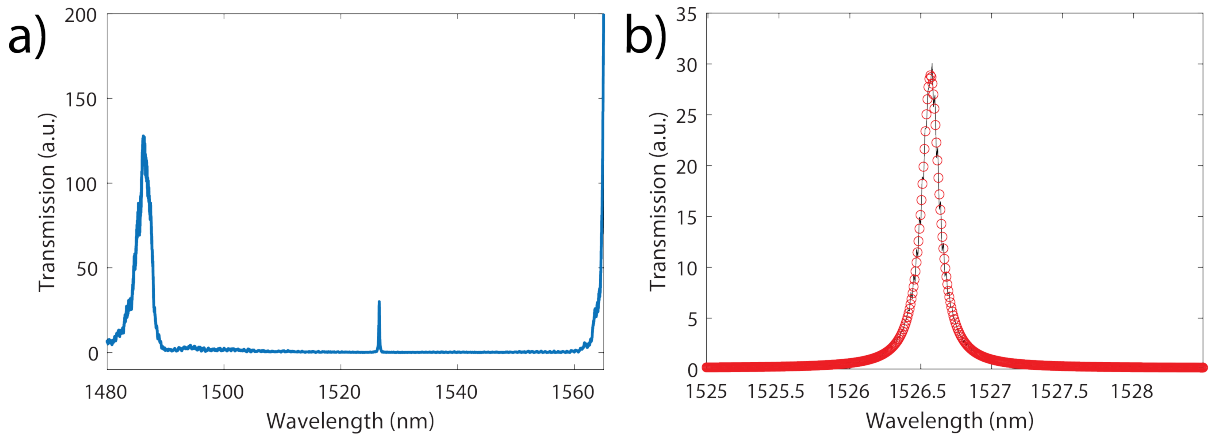

Figure 5.10: IR nanobeam cavity. (a) Transmission spectra across the entire tunable laser range. (b) Close up of the cavity mode.

Chapter 6

TOWARDS SIN RESONATOR ENHANCED SHG

6.1 SiN Nanobeam SHG Platform

With silicon nitride nanobeams in hand we began to explore SHG enhancement by coupling them to TMDs. To date we have yet to demonstrate SHG from this system, but we will describe our previous attempts and indicate key places for improvement.

6.1.1 Initial Experiments

The aforementioned design and demonstrations (Chapter 5) led to a publication in ACS Photonics [29]. However, after many attempts at coupling WSe_2 to the encapsulated nanobeams, it became apparent that the material perturbed the cavity mode too much, resulting in degraded quality factors and frequently destroying the resonance altogether. This is primarily due to the monolayers covering several holes as is seen in Fig. 5.4b. The holes that are covered can no longer be filled with PMMA, causing significant deviations from the design, as verified by FDTD simulations. To solve this we designed an on-substrate nanobeam – one that does not need to be underetched, but does not require a cladding layer either. The design largely follows as previously outlined in Section 5.1. The final result used a beam that was 220 nm thick and 838 nm wide. The Bragg region had 30 periods of ellipsoids at a period of 251 nm. These ellipsoids had a major radius of 130 nm and a minor radius of 43 nm. The cavity was formed by quadratically tapering the major radius up to 191 nm and the period to 231 nm over a course of 10 periods. This led to a cavity with a quality factor of 250,000, and a mode volume of $\approx 1\ (\frac{\lambda}{n})^3$.

TMDs were then transfered onto the nanobeams. Coupling was confirmed through cavity coupled PL. These nanobeams were designed to have resonances near 800 nm to allow for

cavity coupled PL experiments. We have found that these materials do not always couple to PhCCs they are placed on, including PhCCs in other material systems such as GaP. The reason for this is still a topic of current research. However, cavity coupled PL gives a definitive indication of cavity coupling. As these nanobeams had resonances around near 800 nm, we were unable to use the same femto-second laser as we used in the work presented in Chapter 4. Instead we used a pico-second ti:sapphire laser with a 80 MHz repetition rate, resulting in lower peak powers for the same average pump power. We carried out our experiment in two parts: the first where we pumped the grating couplers and collected from the top of the nanobeam, and the second where we pumped and collected from the top of the nanobeams. Neither resulted in appreciable cavity enhanced SHG.

6.1.2 Mitigating Material Damage

One of the prominent difficulties was the relatively low damage threshold of these materials. We found that this threshold was approximately 40 $mW/\mu m^2$. At these powers the SHG generated by the monolayer was barely above the noise floor of our spectrometer. To further understand this we estimated the amount of power at the harmonic wavelength. At these low pump powers the resulting SHG wave with a maximum intensity of a few nW[1]. While such powers enable collection of spectra from the bare monolayer, the additional losses associated with cavity coupling to free space (e.g. grating coupler efficiency and nanobeam to waveguide coupling efficiency) caused the output power from the nanobeam to be undetectably small. Moving forward this low damage threshold will have to be addressed. The easiest solution is to go back to using a femto-second laser with a pulse-picker (to achieve sub-MHz repetition rates). However, our goal is to push towards continuous-wave SHG, in which case the material damage threshold will have to be addressed more directly. For instance, it may be beneficial to cap these TMDs with a thin alumina film in order to help with thermal conductivity and to prevent oxidation.

---

[1]See Appendix A for details on this calculation.

6.1.3 Improving Pump and Collection Efficiency

Our SiN platform to date has entirely been reliant on grating couplers to couple light into and out of our resonators. These grating couplers tended to be limited in maximal efficiency due to the normal incidence and the low refractive index of silicon nitride. Improving the collection and pump efficiency will also be important moving forward. Here I propose the use of edge coupling as it has been shown to be extremely efficient and broadband [96] [46]. We have made significant progress towards this end, having developed a fully functioning edge coupling setup (Fig. 6.1a). Using this setup we have been able to successfully measure a variety of SiN devices (Fig. 6.1b). To date we have needed to use a silicon dioxide hard mask to protect our photonic layer during the deep reactive ion etching (DRIE) of the silicon handle to make room for the lensed fibers. This hard mask must be removed before transferring monolayer TMDs onto the resonators. Removing this mask has proven to be difficult as the SiN and the underlying oxide are also susceptible to etching during its removal. The silicon dioxide hard mask was deposited using plasma enhanced chemical vapor deposition (PECVD). The recipe we used was chosen because it produces low density silicon dioxide that has a much faster etch rate in hydroflouric acid than the silicon nitride and thermal silicon dioxide on our chips. However, during its removal we still observed waveguide liftoff due to the undercutting of the waveguides. This can be avoided by switching to a DRIE that allows for non-silicon based hardmasks, which can be etched without risk to the underlying photonic platform.

6.1.4 Further Improvements to SiN Nanobeam Design

A final improvement will be to the design of the resonator itself. Specifically, improving the coupling between the feeding waveguide and the nanobeam. The design in this thesis has largely followed the convention of the field in that the focus of designing a resonator is in achieving large Q and small V for achieving large cavity enhancement [49]. Unfortunately, this typically results in resonators that are poorly coupled to the feeding waveguide. This

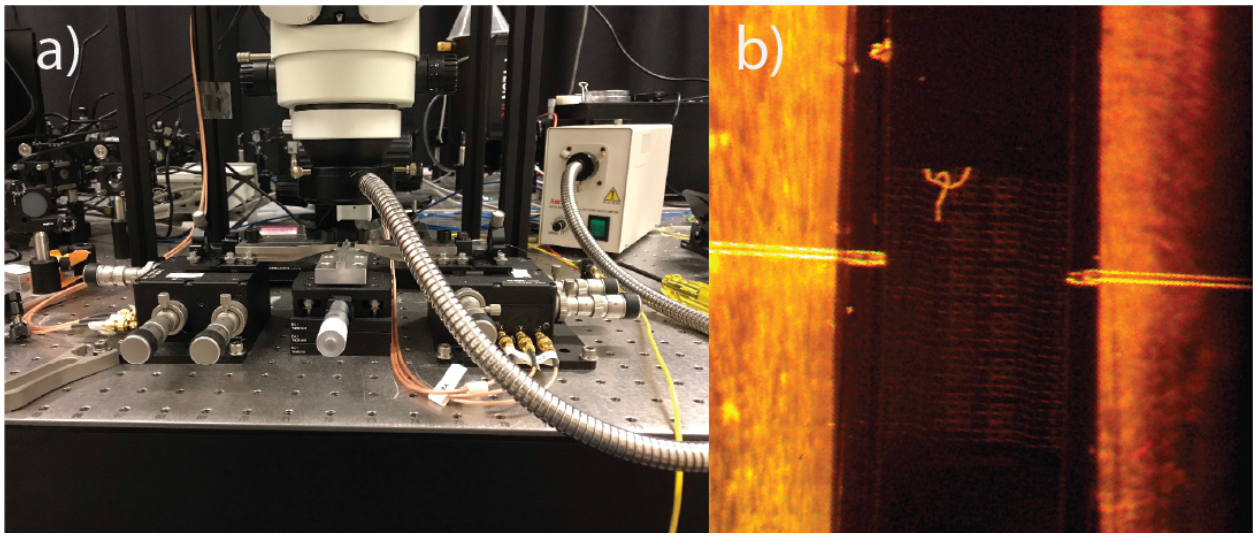

Figure 6.1: Edge coupling chip under test. (a) The edge coupling setup. Alignment is carried out with the aid of the overhead stereo microscope. The setup has two lensed fibers whose positions are controlled using individual three axes stages that have open-loop piezos for fine alignment. Between the two fiber stages there is a chip stage with a single axis stage and a custom chip holder. (b) A chip under test as seen by the stereo microscope. The two lensed fibers are visibly addressing a waveguide.

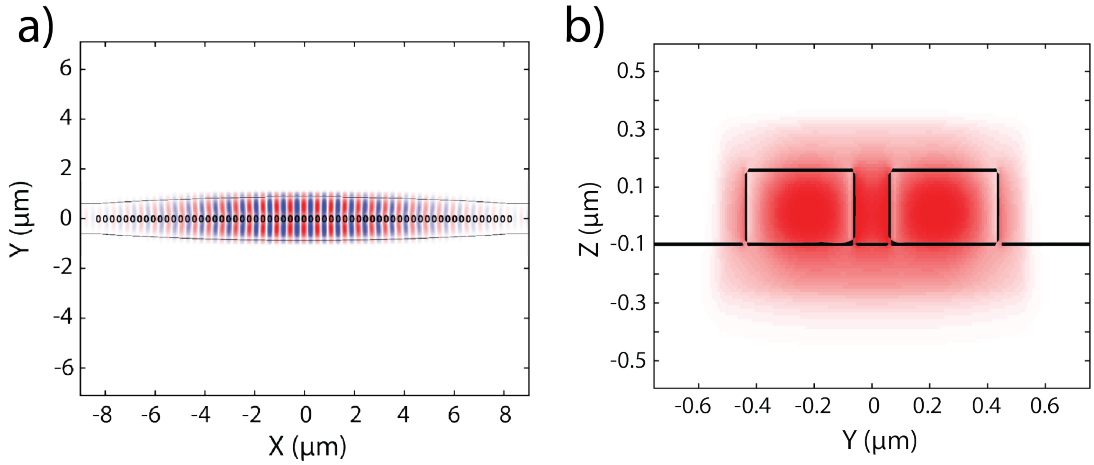

Figure 6.2: Nanobeam with improved coupling to the feeding waveguide. (a) A top-down view of the cavity mode. (b) Cross-section of the center of the cavity.

issue has been addressed by Quan et al. who presented a generic formalism for designing nanobeam resonators that are strongly coupled to the feeding waveguide [89] [88]. Using this formalism, we have begun designing such a nanobeam for use in cavity enhanced SHG from monolayer TMDs (Fig. 6.2). Thus far our design has reached a transmission of 55% which is a large improvement over the <1% for our previous designs. Furthermore, we have opted for an air-mode nanobeam to increase the intensity of light at the top surface where the TMDs will lay. The current design utilizes 220 nm thick SiN. The nanobeam has holes with 75 nm radii, at a periodicity of 275 nm throughout. The cavity is formed by quadratically varying the nanobeam width from 700 nm to 1000 nm. This is an intermediate design that requires more work to improve the quality factor and coupling to the waveguide.

6.2 SiN Ring Resonator SHG Platform

The ability to pattern the nonlinear material to achieve phase matching is appealing for small mode volume devices where phase matching is particularly challenging. However, ring resonators are also an interesting system to consider for patterning based phase-matching.

6.2.1 Demonstrating Doubly Resonant Ring Resonators

We followed the designs for phase matched ring resonators as presented in Chapter 2. Namely, we used waveguides that were 1.1 μm wide and 330 nm tall, resulting in the modes shown in the insets of Fig. 2.2a. While there are many viable sets of fundamental and harmonic modes that are suitable for ring-based SHG devices, this set does not require patterning to observe SHG, yet presents the opportunity for a 9-fold increase in SHG efficiency once patterned. This reduces the experimental difficulty by allowing the fabricated devices to be immediately tested rather than forced to pattern the TMDs prior to measurement, which may damage or otherwise negatively affect the device. Finally, one must consider the surface nonlinearities which have been utilized for resonator enhanced SHG in silicon nitride [61]. While these nonlinearities have been estimated to be very small, where the effective $\chi^{(2)}$ values are on the order of tens of fm/V [61], the amount of surface area that partakes makes

the effect non-negligible. To address this issue, one can slightly change the waveguide width such that the ring is still doubly resonant, but not phase-matched. Care must be taken to ensure the mode mismatch is not so large as to cause the nonlinear overlap to change signs over the extent of the monolayer. This will allow for maximally efficient unpatterned SHG while suppressing the surface nonlinearities.

We have began preliminary doubly resonant ring resonator fabrication and characterization. Our ring resonators are addressed by two bus waveguides (Fig. 6.3a): one to address the ring with 1550 nm light, and the other for 775 nm light. Each bus waveguide is attached to a pair of grating couplers to couple light onto and off the chip. We have demonstrated high quality factor resonances at both the fundamental (Fig. 6.3c) and harmonic (Fig. 6.3d) wavelengths. The 775 nm modes were measured in the same setup as the nanobeams. The 1550 nm modes were measured in a similar setup with 1550 nm optics and spectrometer (Princeton Instruments SpectraPro SP2750i with a PyLon-IR:1024). The profile of the spectra correspond to the wavelength-dependent efficiencies of the grating couplers, while the dips correspond to the cavity modes. The 1550 nm cavity modes have reached quality factors up to $\sim 10^5$ (high Qs were measured with a Santec TSL-510 and Newport 843-R power meter, for higher resolution), and the 775 nm resonances have reached a spectrometer-limited quality factors of $\sim 10^4$. Obtaining these high quality resonances was not only dependent on a high quality dry etching recipe, but also required an annealing step to repair defects in the SiN that cause excess absorption [44] [106]. We have found that annealing for four hours in an oxygen rich atmosphere at 1000 °C, then another four hours at the same temperature in a nitrogen rich atmosphere can improve the quality factor of the 1550 nm resonances by almost an order of magnitude. The most recent challenge has been transferring TMD flakes onto the resonators without also transferring unwanted bulk onto the photonic structures (Fig. 6.3b). These pieces of bulk material are excellent scatters and almost completely block the optical throughput in the waveguides they cover.

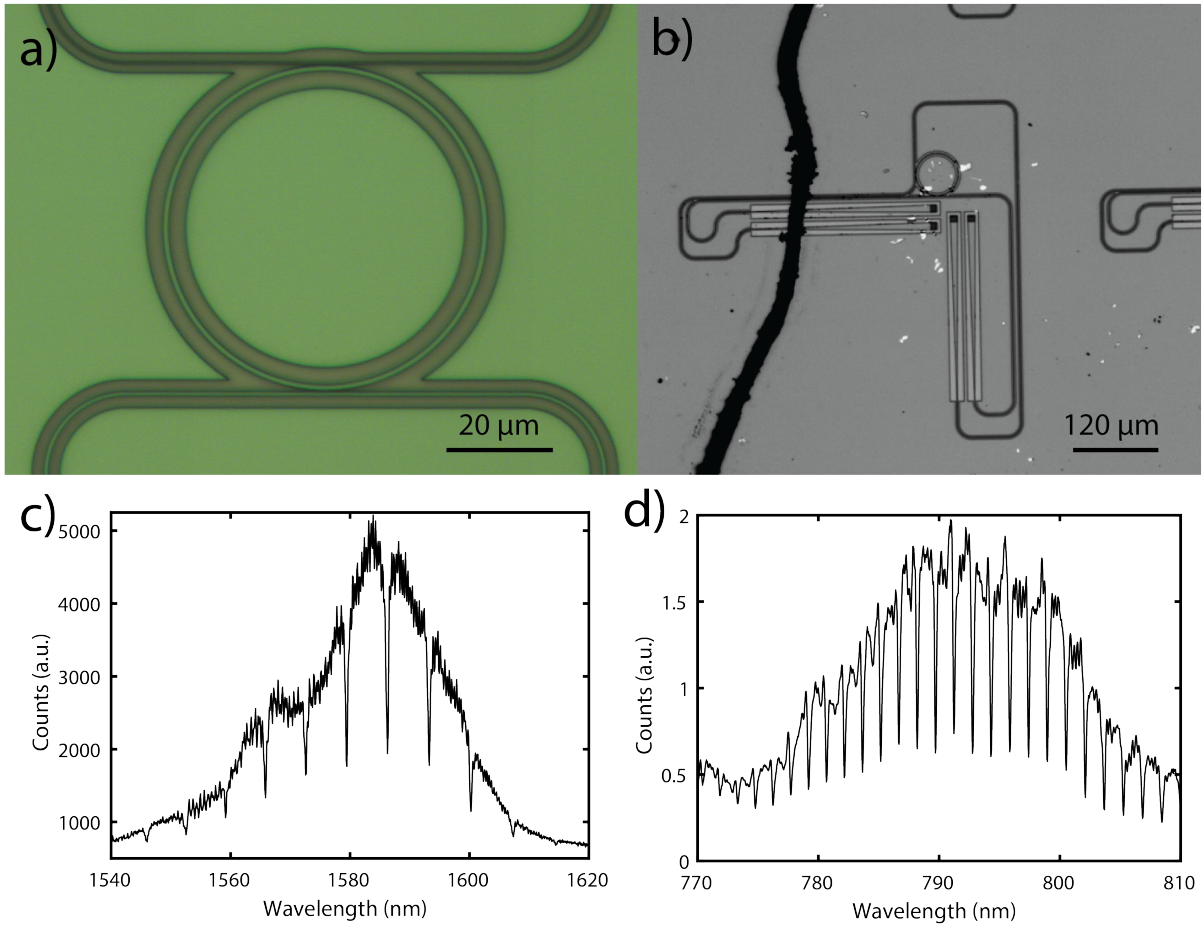

Figure 6.3: Preliminary bi-resonant ring resonator results. (a) Optical micrograph of a bi-resonant ring resonator with a 30 mum radius. The upper bus waveguide couples in 775 nm light, and the lower couples in 1550 nm light. (b) Optical micrograph of a bi-resonant ring resonator after material transfer using the transfer process outline in Section 4.3. The white material flakes are pieces of bulk WSe_2 that strongly scatter light out of the waveguides if placed on top of the waveguides. The thick black line was a strain of PC that was not fully dissolved after a chloroform bath. Transmission spectra of a bi-resonant ring of 30 μm radius near (c) 1550 nm and (d) 775 nm.

6.2.2 Improving Material Transfer

The creating of bulk is an avoidable consequence of mechanical exfoliation onto silicon substrates. Monolayers are almost always found within sections of the chip that have high densities of bulk pieces. As the dry transfer section outlined in Section 4.3 utilizes a relatively flat section of PC to transfer the materials, large sections of exfoliated materials tend to be transferred, rather than select monolayer flakes. Due to the compact nature of PhCCs this does not prove to be an issue for L3 cavities or nanobeams. However, our ring resonators need to have radii above 20 μm in order to avoid excessively low quality factors (Q ~100s) caused by bending and scattering losses. This results in devices that are much larger than the PhCCs, and more importantly, larger than the typical distance between pieces of bulk on an exfoliated chip.

To remedy this issue, we have improved upon the aforementioned dry transfer process to allow for selective transfer of single monolayers, even when located close to bulk samples. First, we form a dome shaped PDMS stamp by pipetting liquid PDMS onto a small piece of cured PMDS. The surface tension of the uncured PDMS causes the formation of a meniscus. The PDMS is then cured upside down to avoid breaking of the meniscus during curing. Once cured, a PC film is draped over the curved PDMS stamp and secured to a glass slide with office tape. Next, the tip of the PC film is drawn into a point. This is accomplished with the aid of the transfer stage shown in Fig. 4.1c. The stamp is affixed to the stage and positioned just above a clean silicon chip (Fig. 6.4i). The chip stage is then heated to 160 °C, which is above the glass-transition temperature of PC [79]. Next, the stamp is then lowered into contact with the stage and allowed to come to thermal equilibrium (Fig. 6.4ii). By lowering the stage temperature to 140 °C the stamp and chip contract drawing the PC into a tip (Fig. 6.4iii). Finally, the stamp is drawn away from the chip and is ready for use (Fig. 6.4iv).

The modified stamps have enabled a much more selective material transfer process. This is illustrated by our studies of material transfer onto an Archimedean spiral (Fig. 6.5a). As the structure is composed of tightly spaced waveguides, it is very sensitive to the transfer of

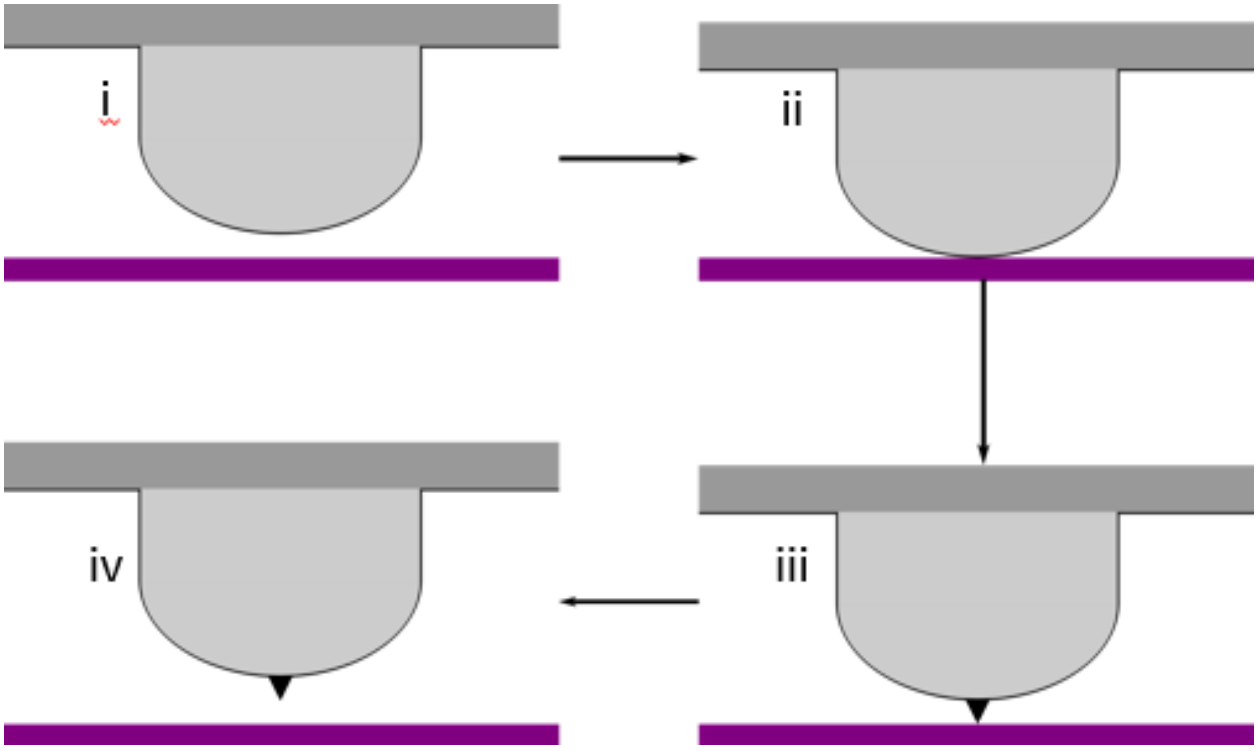

Figure 6.4: Creating the PC needle for the new dry transfer process. (i) The process starts with a dome-shaped PDMS stamp (light gray) attached to a glass slide (dark gray). A PC film is draped over the PDMS stamp (black outline) and held above a clean silicon chip (purple). (ii) The chip is heated to 160 °C and the stamp is lowered into contact. (iii) The chip is then cooled to 140 °C causing the stamp and chip to contract, pulling out a needle of PC (black). (iv) The final stamp is drawn away from the silicon surface and is ready for use.

peripheral bulk. We were able to successfully transfer a lone monolayer of WSe_2 onto the center of the spiral. The presence of the monolayer was confirmed through PL (Fig. 6.5b). Aside from visual inspection, we observed high transmission through the spiral after transfer (Fig. 6.5d), which resembled the pre-transfer transmission (Fig. 6.5c) indicating a bulk free transfer.

6.3 Conclusion

While we have yet to demonstrate silicon nitride nanobeam enhanced SHG from monolayer TMDs, we have identified the major hurdles and demonstrated significant progress towards overcoming them. Specifically we have shown promising results for an improved nanobeam design, and an edge coupling setup that will improve the overall pump and collection efficiency of our system. Furthermore, we have motivated, fabricated, and done preliminary testing of bi-resonant ring resonators for use in cavity enhanced SHG from monolayer TMDs. Bulk TMD material poses a major obstacle to these large resonators, as the scattering losses can completely destroy the guiding properties of waveguides. We have also presented a new transfer method that allows for the selective transfer of monolayers without the accompanying bulk, paving the way for future cavity enhancement of TMDs by ring resonators.

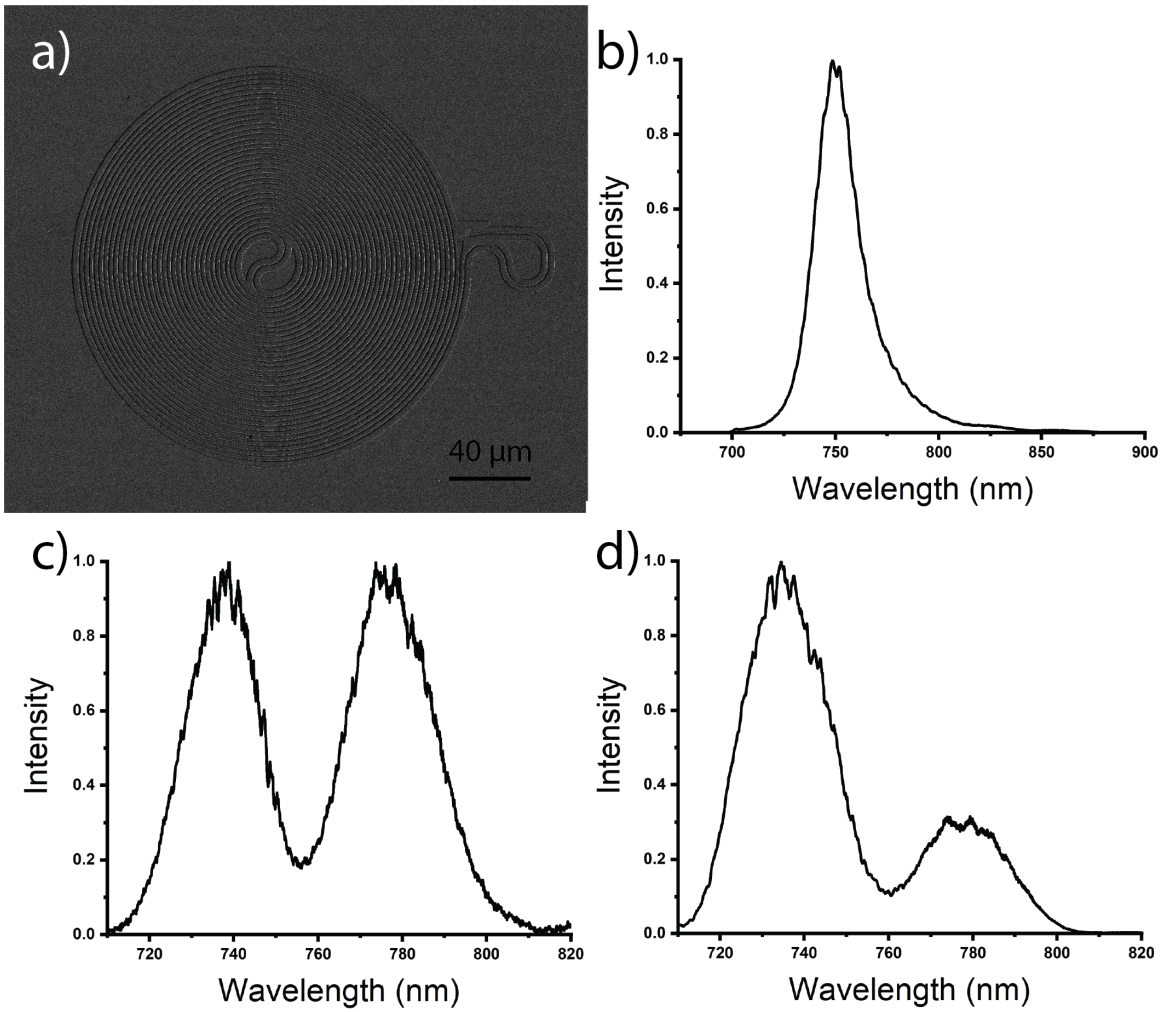

Figure 6.5: Demonstration of the improved transfer technique. (a) An Archimedean spiral we tested the transfer process on. (b) The PL spectra of the monolayer WSe_2 we transfered onto the center, confirming its presence. Transmission spectra (c) before and (d) after transferring the monolayer.

Chapter 7

OUTLOOK

In this thesis I presented a number of works varying from modeling $\chi^{(2)}$ enabled bistability, to cavity design. In this chapter I will outline where I see these contributions can be impactful to fields outside of 2D material nanophotonics.

7.1 Patterned Nonlinear Optics Arbitrary Nonlinear Media

In Chapter 2 I presented a formalism for maximizing the nonliearity of doubly resonant linear cavities clad with TMDs. The analysis of waveguides, large ring resonators, and microdisk resonators showed that TMD clad resonators provided a smaller nonlinearity than AlN or GaP platforms, but still had appreciable nonlinearities. More importantly, we were able to predict that such a platform can compensate for fabrication errors in the underlying passive platform that results in a momentum mismatch between the fundamental and harmonic modes. Furthermore, we predicted that the etching of the nonlinear cladding does not have stringent tolerances; there are large tolerances for both under- and over-etching the nonlinear cladding (Fig. 2.3b). This same set of attractive features applies to any sort of nonlinear cladding, not just TMDs. We envision that this patterning will be extended to other materials such as barium titanate which has an incredibly high susceptibility of $r_{42} = 923\ pm/V$ [3]. Furthermore, thin films of this material can be grown on silicon substrates[3], making it particularly appealing. In order to extend our formalism to new materials such a barium titanate, one simply has to account for the crystal symmetries at hand when choosing the desired modes and etching patterns as dictated by said modes and crystal symmetries.

7.2 SiN Nanobeams for Enhancing Emission from Solution Processed Materials

The encapsulated SiN nanobeams presented in Chapter 5 were designed for integration with TMDs, but are a valuable tool for enhancing the properties of other materials. One area where these nanobeams have already made an impact is in the Purcell enhancement of colloidal quantum dots (QDs) [20]. The encapsulated nature of these nanobeams lend themselves to this application as the QDs are deposited by spin-coating. By encapsulating the nanobeams with PMMA and selectively exposing holes over the cavity center, one can select where and how many QDs are coupled to the underlying photonic structure (Fig. 7.1). Figure 7.2a shows a SEM of one of the nanobeams with a red region exemplifying one of the PMMA window sizes. When we excited the QDs with 532 nm laser light, we were able to observe strong emission from the QDs (Fig. 7.2b). Finally, we compared the spectra of the QDs that were coupled to the cavities to those that were not coupled (Fig. 7.2c). We found that only the nanobeams with PMMA windows showed cavity coupling. For the QDs coupled to the nanobeams, we were able to show a Purcell enhancement by a factor of 1.26 [20]. This study shows the efficacy of these nanobeams for Purcell enhancement of colloidal QDs. We envision that these nanobeams will find further use in enhancing the light emission from other emergent materials such as perovskites, and enable the study of nonlinear effects beyond SHG such as saturable absorption.

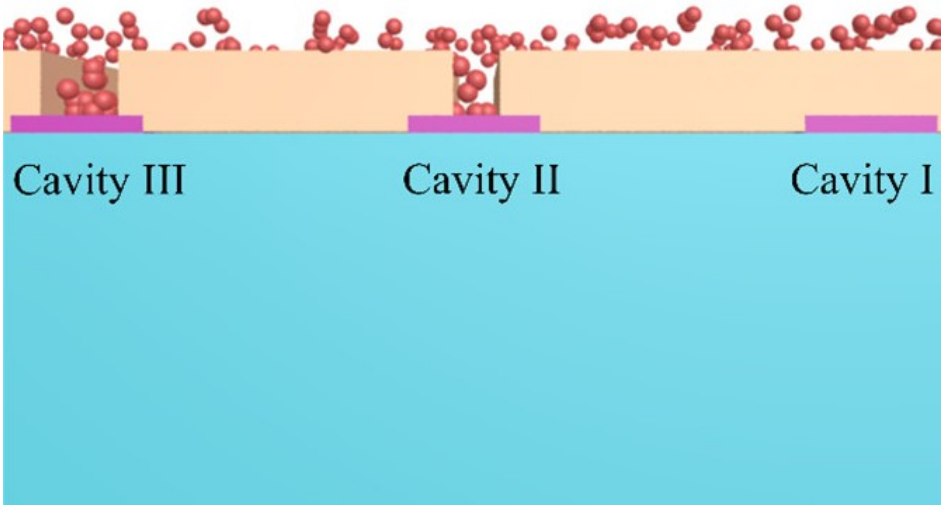

Figure 7.1: Schematic of the nanobeams (purple rectangles) coupled to QD (red circles). The QDs are deterministically coupled to selected nanobeams by lithographically opening holes in the cladding PMMA layer (orange), before the QDs are spun onto the sample. By varying the hole size one can control the number of QDs coupled to the nanobeam.

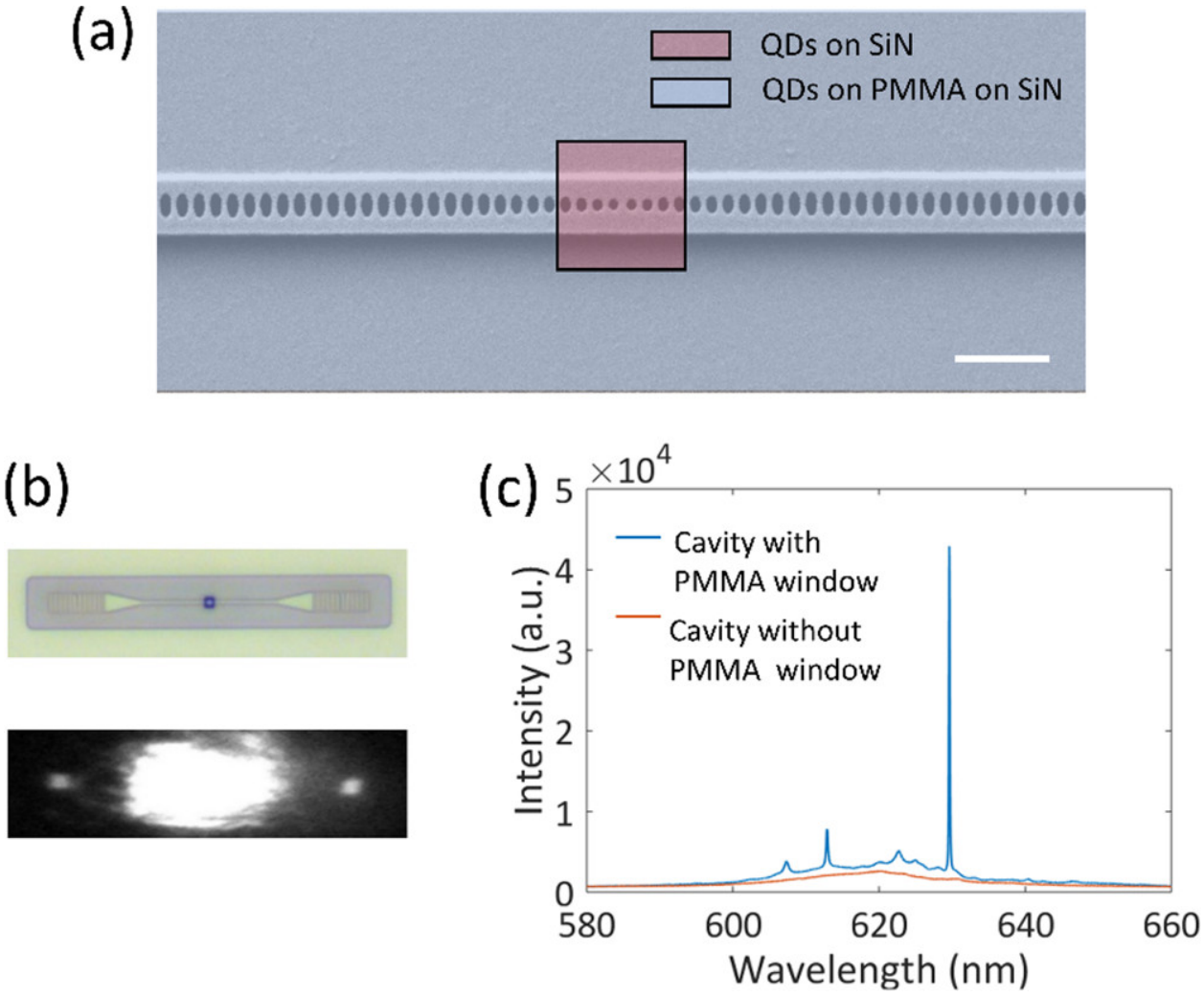

Figure 7.2: QD coupled to SiN nanobeams. (a) A SEM of one of the SiN nanobeams overlayed with a red square showing the exposure window for the cladding PMMA. (b) Optical micrograph of the SiN nanobeams with QDs in a PMMA window (top), and during a PL measurement (bottom). (c) Spectra of nanobeams with a PMMA window allowing for QDs to couple to the nanobeam (blue), and a nanobeam without a window preventing QD-nanobeam coupling.

BIBLIOGRAPHY

[1] FDTD Solutions lumerical inc. https://www.lumerical.com/.

[2] Mode Solutions lumerical inc. https://www.lumerical.com/.

[3] Stefan Abel, Felix Eltes, J. Elliott Ortmann, Andreas Messner, Pau Castera, Tino Wagner, Darius Urbonas, Alvaro Rosa, Ana M. Gutierrez, Domenico Tulli, Ping Ma, Benedikt Baeuerle, Arne Josten, Wolfgang Heni, Daniele Caimi, Lukas Czornomaz, Alexander A. Demkov, Juerg Leuthold, Pablo Sanchis, and Jean Fompeyrine. Large pockels effect in micro- and nanostructured barium titanate integrated on silicon. *Nature Materials*, 18(1):42–47, 2019.

[4] Obafunso A Ajayi, Jenny V Ardelean, Gabriella D Shepard, Jue Wang, Abhinandan Antony, Takeshi Taniguchi, Kenji Watanabe, Tony F Heinz, Stefan Strauf, X-Y Zhu, and James C Hone. Approaching the intrinsic photoluminescence linewidth in transition metal dichalcogenide monolayers. *2D Materials*, 4(3):031011, jul 2017.

[5] Vilson R. Almeida and Michal Lipson. Optical bistability on a silicon chip. *Opt. Lett.*, 29(20):2387–2389, Oct 2004.

[6] J. A. Armstrong, N. Bloembergen, J. Ducuing, and P. S. Pershan. Interactions between light waves in a nonlinear dielectric. *Phys. Rev.*, 127:1918–1939, Sep 1962.

[7] Takashi Asano, Yoshiaki Ochi, Yasushi Takahashi, Katsuhiro Kishimoto, and Susumu Noda. Photonic crystal nanocavity with a q factor exceeding eleven million. *Opt. Express*, 25(3):1769–1777, Feb 2017.

[8] Anton Autere, Henri Jussila, Yunyun Dai, Yadong Wang, Harri Lipsanen, and Zhipei Sun. Nonlinear optics with 2d layered materials. *Advanced Materials*, 30(24):1705963, 2018.

[9] Michael Barth, Josef Kouba, Johannes Stingl, Bernd Löchel, and Oliver Benson. Modification of visible spontaneous emission with silicon nitride photonic crystal nanocavities. *Opt. Express*, 15(25):17231–17240, Dec 2007.

[10] Michael Barth, Nils Nsse, Johannes Stingl, Bernd Lchel, and Oliver Benson. Emission properties of high-q silicon nitride photonic crystal heterostructure cavities. *Applied Physics Letters*, 93(2):021112, 2008.

[11] G. Beadie, Michael Brindza, Richard A. Flynn, A. Rosenberg, and James S. Shirk. Refractive index measurements of poly(methyl methacrylate) (pmma). *Appl. Opt.*, 54(31):F139–F143, Nov 2015.

[12] Zhuan-Fang Bi, Alejandro W. Rodriguez, Hila Hashemi, David Duchesne, Marko Loncar, Ke-Ming Wang, and Steven G. Johnson. High-efficiency second-harmonic generation in doubly-resonant $\chi(2)$ microring resonators. *Opt. Express*, 20(7):7526–7543, Mar 2012.

[13] P. Blake, E. W. Hill, A. H. Castro Neto, K. S. Novoselov, D. Jiang, R. Yang, T. J. Booth, and A. K. Geim. Making graphene visible. *Applied Physics Letters*, 91(6):063124, 2007.

[14] W. Bogaerts, P. De Heyn, T. Van Vaerenbergh, K. De Vos, S. Kumar Selvaraja, T. Claes, P. Dumon, P. Bienstman, D. Van Thourhout, and R. Baets. Silicon microring resonators. *Laser & Photonics Reviews*, 6(1):47–73, 2012.

[15] R.W. Boyd and D. Prato. *Nonlinear Optics*. Elsevier Science, 2008.

[16] Sonia Buckley, Marina Radulaski, Jingyuan Linda Zhang, Jan Petykiewicz, Klaus Biermann, and Jelena Vučković. Multimode nanobeam cavities for nonlinear optics: high quality resonances separated by an octave. *Opt. Express*, 22(22):26498–26509, Nov 2014.

[17] Ian B. Burgess, Alejandro W. Rodriguez, Murray W. McCutcheon, Jorge Bravo-Abad, Yinan Zhang, Steven G. Johnson, and Marko Lončar. Difference-frequency generation with quantum-limited efficiency in triply-resonant nonlinear cavities. *Opt. Express*, 17(11):9241–9251, May 2009.

[18] Andres Castellanos-Gomez. Why all the fuss about 2d semiconductors? *Nature Photonics*, 10:202 EP –, Mar 2016.

[19] Lin Chang, Andreas Boes, Xiaowen Guo, Daryl T. Spencer, M. J. Kennedy, Jon D. Peters, Nicolas Volet, Jeff Chiles, Abijith Kowligy, Nima Nader, Daniel D. Hickstein, Eric J. Stanton, Scott A. Diddams, Scott B. Papp, and John E. Bowers. Heterogeneously integrated gaas waveguides on insulator for efficient frequency conversion. *Laser & Photonics Reviews*, 12(10):1800149, 2018.

[20] Yueyang Chen, Albert Ryou, Max R. Friedfeld, Taylor Fryett, James Whitehead, Brandi M. Cossairt, and Arka Majumdar. Deterministic positioning of colloidal quantum dots on silicon nitride nanobeam cavities. *Nano Letters*, 18(10):6404–6410, 2018.

[21] Alexey Chernikov, Timothy C. Berkelbach, Heather M. Hill, Albert Rigosi, Yilei Li, Ozgur Burak Aslan, David R. Reichman, Mark S. Hybertsen, and Tony F. Heinz. Exciton binding energy and nonhydrogenic rydberg series in monolayer ws_2. *Phys. Rev. Lett.*, 113:076802, Aug 2014.

[22] M. Davano, S. Ates, Y. Liu, and K. Srinivasan. Si3n4 optomechanical crystals in the resolved-sideband regime. *Applied Physics Letters*, 104(4):041101, 2014.

[23] Jared K. Day, Meng-Hsi Chung, Yi-Hsien Lee, and Vinod M. Menon. Microcavity enhanced second harmonic generation in 2d mos2. *Opt. Mater. Express*, 6(7):2360–2365, Jul 2016.

[24] C. Doerr, L. Chen, D. Vermeulen, T. Nielsen, S. Azemati, S. Stulz, G. McBrien, X. . Xu, B. Mikkelsen, M. Givehchi, C. Rasmussen, and S. . Park. Single-chip silicon photonics 100-gb/s coherent transceiver. In *OFC 2014*, pages 1–3, March 2014.

[25] Marcus W. Doherty, Neil B. Manson, Paul Delaney, Fedor Jelezko, Jrg Wrachtrup, and Lloyd C.L. Hollenberg. The nitrogen-vacancy colour centre in diamond. *Physics Reports*, 528(1):1 – 45, 2013. The nitrogen-vacancy colour centre in diamond.

[26] Dirk Englund, Andrei Faraon, Ilya Fushman, Nick Stoltz, Pierre Petroff, and Jelena Vuckovic. Controlling cavity reflectivity with a single quantum dot. *Nature*, 450:857 EP –, Dec 2007.

[27] Valla Fatemi, Sanfeng Wu, Yuan Cao, Landry Bretheau, Quinn D. Gibson, Kenji Watanabe, Takashi Taniguchi, Robert J. Cava, and Pablo Jarillo-Herrero. Electrically tunable low-density superconductivity in a monolayer topological insulator. *Science*, 362(6417):926–929, 2018.

[28] P. A. Franken, A. E. Hill, C. W. Peters, and G. Weinreich. Generation of optical harmonics. *Phys. Rev. Lett.*, 7:118–119, Aug 1961.

[29] Taylor K. Fryett, Yueyang Chen, James Whitehead, Zane Matthew Peycke, Xiaodong Xu, and Arka Majumdar. Encapsulated silicon nitride nanobeam cavity for hybrid nanophotonics. *ACS Photonics*, 5(6):2176–2181, Jun 2018.

[30] Taylor K. Fryett, Christopher M. Dodson, and Arka Majumdar. Cavity enhanced nonlinear optics for few photon optical bistability. *Opt. Express*, 23(12):16246–16255, Jun 2015.

[31] Taylor K Fryett, Kyle L Seyler, Jiajiu Zheng, Chang-Hua Liu, Xiaodong Xu, and Arka Majumdar. Silicon photonic crystal cavity enhanced second-harmonic generation from monolayer wse2. *2D Materials*, 4(1):015031, Jul 2016.

[32] Taylor K. Fryett, Alan Zhan, and Arka Majumdar. Phase-matched nonlinear optics via patterning layered materials. *Opt. Lett.*, 42(18):3586–3589, Sep 2017.

[33] K.-M. C. Fu, C. Santori, P. E. Barclay, and R. G. Beausoleil. Conversion of neutral nitrogen-vacancy centers to negatively charged nitrogen-vacancy centers through selective oxidation. *Applied Physics Letters*, 96(12):121907, 2010.

[34] Xue-Tao Gan, Chen-Yang Zhao, Si-Qi Hu, Tao Wang, Yu Song, Jie Li, Qing-Hua Zhao, Wan-Qi Jie, and Jian-Lin Zhao. Microwatts continuous-wave pumped second harmonic generation in few- and mono-layer gase. *Light: Science &Amp; Applications*, 7:17126 EP –, Jan 2018. Article.

[35] C. W. Gardiner and P. Zoller. *Quantum Noise*. Springer-Verlag, 2005.

[36] Jian-Feng Ge, Zhi-Long Liu, Canhua Liu, Chun-Lei Gao, Dong Qian, Qi-Kun Xue, Ying Liu, and Jin-Feng Jia. Superconductivity above 100 k in single-layer fese films on doped srtio3. *Nature Materials*, 14:285 EP –, Nov 2014.

[37] A. K. Geim and I. V. Grigorieva. Van der waals heterostructures. *Nature*, 499:419 EP –, Jul 2013. Perspective.

[38] Roman V. Gorbachev, Ibtsam Riaz, Rahul R. Nair, Rashid Jalil, Liam Britnell, Branson D. Belle, Ernie W. Hill, Kostya S. Novoselov, Kenji Watanabe, Takashi Taniguchi, Andre K. Geim, and Peter Blake. Hunting for monolayer boron nitride: Optical and raman signatures. *Small*, 7(4):465–468, 2011.

[39] David Griffiths. *Introduction to Electrodynamics*. Cambridge University Press, 1999.

[40] Samantha M. Grist, Shon A. Schmidt, Jonas Flueckiger, Valentina Donzella, Wei Shi, Sahba Talebi Fard, James T. Kirk, Daniel M. Ratner, Karen C. Cheung, and Lukas Chrostowski. Silicon photonic micro-disk resonators for label-free biosensing. *Opt. Express*, 21(7):7994–8006, Apr 2013.

[41] Xiang Guo, Chang-Ling Zou, and Hong X. Tang. Second-harmonic generation in aluminum nitride microrings with 2500%/w conversion efficiency. *Optica*, 3(10):1126–1131, Oct 2016.

[42] Keliang He, Nardeep Kumar, Liang Zhao, Zefang Wang, Kin Fai Mak, Hui Zhao, and Jie Shan. Tightly bound excitons in monolayer wse_2. *Phys. Rev. Lett.*, 113:026803, Jul 2014.

[43] Yu-Ming He, Genevieve Clark, John R. Schaibley, Yu He, Ming-Cheng Chen, Yu-Jia Wei, Xing Ding, Qiang Zhang, Wang Yao, Xiaodong Xu, Chao-Yang Lu, and Jian-Wei Pan. Single quantum emitters in monolayer semiconductors. *Nature Nanotechnology*, 10:497 EP –, May 2015.

[44] Amir H. Hosseinnia, Amir H. Atabaki, Ali A. Eftekhar, and Ali Adibi. High-quality silicon on silicon nitride integrated optical platform with an octave-spanning adiabatic interlayer coupler. *Opt. Express*, 23(23):30297–30307, Nov 2015.

[45] Bevin Huang, Genevieve Clark, Efrén Navarro-Moratalla, Dahlia R. Klein, Ran Cheng, Kyle L. Seyler, Ding Zhong, Emma Schmidgall, Michael A. McGuire, David H. Cobden, Wang Yao, Di Xiao, Pablo Jarillo-Herrero, and Xiaodong Xu. Layer-dependent ferromagnetism in a van der waals crystal down to the monolayer limit. *Nature*, 546:270 EP –, Jun 2017.

[46] R. G. Hunsperger, A. Yariv, and A. Lee. Parallel end-butt coupling for optical integrated circuits. *Appl. Opt.*, 16(4):1026–1032, Apr 1977.

[47] A. Iqbal, W. B. Jackson, C. C. Tsai, J. W. Allen, and C. W. Bates. Electronic structure of silicon nitride and amorphous silicon/silicon nitride band offsets by electron spectroscopy. *Journal of Applied Physics*, 61(8):2947–2954, 1987.

[48] Corey Janisch, Yuanxi Wang, Ding Ma, Nikhil Mehta, Ana Laura Elías, Néstor Perea-López, Mauricio Terrones, Vincent Crespi, and Zhiwen Liu. Extraordinary second harmonic generation in tungsten disulfide monolayers. *Scientific Reports*, 4:5530 EP –, Jul 2014. Article.

[49] John D. Joannopoulos, Steven G. Johnson, Joshua N. Winn, and Robert D. Meade. *Photonic Crystals: Molding the Flow of Light (Second Edition)*. Princeton University Press, 2 edition, 2008.

[50] Sajeev John. Strong localization of photons in certain disordered dielectric superlattices. *Phys. Rev. Lett.*, 58:2486–2489, Jun 1987.

[51] Steven G. Johnson and J. D. Joannopoulos. Block-iterative frequency-domain methods for maxwell's equations in a planewave basis. *Opt. Express*, 8(3):173–190, Jan 2001.

[52] Mughees Khan, Thomas Babinec, Murray W. McCutcheon, Parag Deotare, and Marko Lončar. Fabrication and characterization of high-quality-factor silicon nitride nanobeam cavities. *Opt. Lett.*, 36(3):421–423, Feb 2011.

[53] M. Kitamura, S. Iwamoto, and Y. Arakawa. Enhanced light emission from an organic photonic crystal with a nanocavity. *Applied Physics Letters*, 87(15):151119, 2005.

[54] Nardeep Kumar, Sina Najmaei, Qiannan Cui, Frank Ceballos, Pulickel M. Ajayan, Jun Lou, and Hui Zhao. Second harmonic microscopy of monolayer mos2. *Phys. Rev. B*, 87:161403, Apr 2013.

[55] P. S. Kuo, W. Fang, and G. S. Solomon. 4-quasi-phase-matched interactions in gaas microdisk cavities. *Opt. Lett.*, 34(22):3580–3582, Nov 2009.

[56] Paulina S Kuo, Jorge Bravo-Abad, and Glenn S Solomon. Second-harmonic generation using 4-quasi-phasematching in a GaAs whispering-gallery-mode microcavity. *Nature communications*, 5:3109, 2014.

[57] Paulina S. Kuo and Glenn S. Solomon. On- and off-resonance second-harmonic generation in gaas microdisks. *Opt. Express*, 19(18):16898–16918, Aug 2011.

[58] Eiichi Kuramochi, Elan Grossman, Kengo Nozaki, Koji Takeda, Akihiko Shinya, Hideaki Taniyama, and Masaya Notomi. Systematic hole-shifting of l-type nanocavity with an ultrahigh q factor. *Opt. Lett.*, 39(19):5780–5783, Oct 2014.

[59] Chinh Tam Le, Daniel J. Clark, Farman Ullah, Velusamy Senthilkumar, Joon I. Jang, Yumin Sim, Maeng-Je Seong, Koo-Hyun Chung, Hyoyeol Park, and Yong Soo Kim. Nonlinear optical characteristics of monolayer mose2. *Annalen der Physik*, 528(7-8):551–559, 2016.

[60] Yi-Hsien Lee, Xin-Quan Zhang, Wenjing Zhang, Mu-Tung Chang, Cheng-Te Lin, Kai-Di Chang, Ya-Chu Yu, Jacob Tse-Wei Wang, Chia-Seng Chang, Lain-Jong Li, and Tsung-Wu Lin. Synthesis of large-area mos2 atomic layers with chemical vapor deposition. *Advanced Materials*, 24(17):2320–2325, 2012.

[61] Jacob S. Levy, Mark A. Foster, Alexander L. Gaeta, and Michal Lipson. Harmonic generation in silicon nitride ring resonators. *Opt. Express*, 19(12):11415–11421, Jun 2011.

[62] Yilei Li, Yi Rao, Kin Fai Mak, Yumeng You, Shuyuan Wang, Cory R. Dean, and Tony F. Heinz. Probing symmetry properties of few-layer mos2 and h-bn by optical second-harmonic generation. *Nano Letters*, 13(7):3329–3333, 2013. PMID: 23718906.

[63] Zin Lin, Xiangdong Liang, Marko Lončar, Steven G. Johnson, and Alejandro W. Rodriguez. Cavity-enhanced second-harmonic generation via nonlinear-overlap optimization. *Optica*, 3(3):233–238, Mar 2016.

[64] Chang-Hua Liu, Genevieve Clark, Taylor Fryett, Sanfeng Wu, Jiajiu Zheng, Fariba Hatami, Xiaodong Xu, and Arka Majumdar. Nanocavity integrated van der waals heterostructure light-emitting tunneling diode. *Nano Letters*, 17(1):200–205, 2017. PMID: 27936763.

[65] Hsiang-Lin Liu, Chih-Chiang Shen, Sheng-Han Su, Chang-Lung Hsu, Ming-Yang Li, and Lain-Jong Li. Optical properties of monolayer transition metal dichalcogenides probed by spectroscopic ellipsometry. *Applied Physics Letters*, 105(20):201905, 2014.

[66] R. Lo Savio, S. L. Portalupi, D. Gerace, A. Shakoor, T. F. Krauss, L. OFaolain, L. C. Andreani, and M. Galli. Room-temperature emission at telecom wavelengths from silicon photonic crystal nanocavities. *Applied Physics Letters*, 98(20):201106, 2011.

[67] A Lohrmann, B C Johnson, J C McCallum, and S Castelletto. A review on single photon sources in silicon carbide. *Reports on Progress in Physics*, 80(3):034502, jan 2017.

[68] Kevin Luke, Yoshitomo Okawachi, Michael R. E. Lamont, Alexander L. Gaeta, and Michal Lipson. Broadband mid-infrared frequency comb generation in a si3n4 microresonator. *Opt. Lett.*, 40(21):4823–4826, Nov 2015.

[69] Arka Majumdar, Christopher M. Dodson, Taylor K. Fryett, Alan Zhan, Sonia Buckley, and Dario Gerace. Hybrid 2d material nanophotonics: A scalable platform for low-power nonlinear and quantum optics. *ACS Photonics*, 2(8):1160–1166, Aug 2015.

[70] Arka Majumdar and Dario Gerace. Single-photon blockade in doubly resonant nanocavities with second-order nonlinearity. *Physical Review B 87*, 235319, 2013.

[71] Kin Fai Mak, Changgu Lee, James Hone, Jie Shan, and Tony F. Heinz. Atomically thin mos_2: A new direct-gap semiconductor. *Phys. Rev. Lett.*, 105:136805, Sep 2010.

[72] Leandro M. Malard, Thonimar V. Alencar, Ana Paula M. Barboza, Kin Fai Mak, and Ana M. de Paula. Observation of intense second harmonic generation from mos_2 atomic crystals. *Phys. Rev. B*, 87:201401, May 2013.

[73] I. H. Malitson. Interspecimen comparison of the refractive index of fused silica∗,. *J. Opt. Soc. Am.*, 55(10):1205–1209, Oct 1965.

[74] L. Martiradonna, F. Pisanello, T. Stomeo, A. Qualtieri, G. Vecchio, S. Sabella, M. De Vittorio, and P. P. Pompa. *Silicon nitride photonic crystal nanocavities for biochip applications*, pages 1–4. IEEE, June 2011.

[75] Luigi Martiradonna, Luigi Carbone, Aniwat Tandaechanurat, Masatoshi Kitamura, Satoshi Iwamoto, Liberato Manna, Massimo De Vittorio, Roberto Cingolani, and Yasuhiko Arakawa. Two-dimensional photonic crystal resist membrane nanocavity embedding colloidal dot-in-a-rod nanocrystals. *Nano Letters*, 8(1):260–264, 2008. PMID: 18095734.

[76] Murray W. McCutcheon, Darrick E. Chang, Yinan Zhang, Mikhail D. Lukin, and Marko Lončar. Broadband frequency conversion and shaping of single photons emitted from a nonlinear cavity. *Opt. Express*, 17(25):22689–22703, Dec 2009.

[77] David A B Miller. Are optical transistors the logical next step? *Nature Photonics*, 4:3–5, 2010.

[78] Momchil Minkov and Vincenzo Savona. Automated optimization of photonic crystal slab cavities. *Scientific Reports*, 4:5124 EP –, May 2014. Article.

[79] Ha Thi Hoang Nguyen, Pengxu Qi, Mayra Rostagno, Amr Feteha, and Stephen A. Miller. The quest for high glass transition temperature bioplastics. *J. Mater. Chem. A*, 6:9298–9331, 2018.

[80] K. S. Novoselov, A. K. Geim, S. V. Morozov, D. Jiang, Y. Zhang, S. V. Dubonos, I. V. Grigorieva, and A. A. Firsov. Electric field effect in atomically thin carbon films. *Science*, 306(5696):666–669, 2004.

[81] K. S. Novoselov, D. Jiang, F. Schedin, T. J. Booth, V. V. Khotkevich, S. V. Morozov, and A. K. Geim. Two-dimensional atomic crystals. *Proceedings of the National Academy of Sciences*, 102(30):10451–10453, 2005.

[82] Kengo Nozaki, Akihiko Shinya, Shinji Matsuo, Yasumasa Suzaki, Toru Segawa, Tomonari Sato, Yoshihiro Kawaguchi, Ryo Takahashi, and Masaya Notomi. Ultralow-power all-optical ram based on nanocavities. *Nature Photonics*, 6:248 EP –, Feb 2012. Article.

[83] Kengo Nozaki, Akihiko Shinya, Shinji Matsuo, Yasumasa Suzaki, Toru Segawa, Tomonari Sato, Yoshihiro Kawaguchi, Ryo Takahashi, and Masaya Notomi. Ultralow-power all-optical ram based on nanocavities. *Nature Photonics*, 6:248252, 2012.

[84] D. Panettieri, L. O'Faolain, and M. Grande. *Control of Q-factor in nanobeam cavities on substrate*, pages 1–4. IEEE, July 2016.

[85] W. H. P. Pernice, C. Xiong, C. Schuck, and H. X. Tang. Second harmonic generation in phase matched aluminum nitride waveguides and micro-ring resonators. *Applied Physics Letters*, 100(22):223501, 2012.

[86] Christopher V. Poulton, Ami Yaacobi, David B. Cole, Matthew J. Byrd, Manan Raval, Diedrik Vermeulen, and Michael R. Watts. Coherent solid-state lidar with silicon photonic optical phased arrays. *Opt. Lett.*, 42(20):4091–4094, Oct 2017.

[87] E. M. Purcell, H. C. Torrey, and R. V. Pound. Resonance absorption by nuclear magnetic moments in a solid. *Phys. Rev.*, 69:37–38, Jan 1946.

[88] Qimin Quan, Parag B. Deotare, and Marko Loncar. Photonic crystal nanobeam cavity strongly coupled to the feeding waveguide. *Applied Physics Letters*, 96(20):203102, 2010.

[89] Qimin Quan and Marko Loncar. Deterministic design of wavelength scale, ultra-high q photonic crystal nanobeam cavities. *Opt. Express*, 19(19):18529–18542, Sep 2011.

[90] Lord Rayleigh. The propagation of waves through a medium endowed with a periodic structure. *Philosopical Magazine*, 1887.

[91] G. T. Reed, G. Mashanovich, F. Y. Gardes, and D. J. Thomson. Silicon optical modulators. *Nature Photonics*, 4:518 EP –, Jul 2010. Review Article.

[92] J Ribeiro-Soares, C Janisch, Z Liu, A L Elias, M S Dresselhaus, M Terrones, L G Cancado, and A Jorio. Second harmonic generation in wse2. *2D Materials*, 2(4):045015, dec 2015.

[93] Pasqual Rivera, John R. Schaibley, Aaron M. Jones, Jason S. Ross, Sanfeng Wu, Grant Aivazian, Philip Klement, Kyle Seyler, Genevieve Clark, Nirmal J. Ghimire, Jiaqiang Yan, D. G. Mandrus, Wang Yao, and Xiaodong Xu. Observation of long-lived interlayer excitons in monolayer mose2-wse2 heterostructures. *Nature Communications*, 6:6242 EP –, Feb 2015. Article.

[94] Kelley Rivoire, Sonia Buckley, and Jelena Vučković. Multiply resonant photonic crystal nanocavities for nonlinear frequency conversion. *Opt. Express*, 19(22):22198–22207, Oct 2011.

[95] Alejandro Rodriguez, Marin Soljačić, J. D. Joannopoulos, and Steven G. Johnson. $\chi(2)$ and $\chi(3)$ harmonic generation at a critical power in inhomogeneous doubly resonant cavities. *Opt. Express*, 15(12):7303–7318, Jun 2007.

[96] S. Romero-Garca, B. Marzban, F. Merget, B. Shen, and J. Witzens. Edge couplers with relaxed alignment tolerance for pick-and-place hybrid integration of iiiv lasers with soi waveguides. *IEEE Journal of Selected Topics in Quantum Electronics*, 20(4):369–379, July 2014.

[97] Jason S. Ross, Philip Klement, Aaron M. Jones, Nirmal J. Ghimire, Jiaqiang Yan, D. G. Mandrus, Takashi Taniguchi, Kenji Watanabe, Kenji Kitamura, Wang Yao, David H. Cobden, and Xiaodong Xu. Electrically tunable excitonic light-emitting diodes based on monolayer wse2 p-n junctions. *Nature Nanotechnology*, 9:268 EP –, Mar 2014.

[98] Roland Schiek and Thomas Pertsch. Absolute measurement of the quadratic nonlinear susceptibility of lithium niobate in waveguides. *Opt. Mater. Express*, 2(2):126–139, Feb 2012.

[99] Jon A. Schuller, Sinan Karaveli, Theanne Schiros, Keliang He, Shyuan Yang, Ioannis Kymissis, Jie Shan, and Rashid Zia. Orientation of luminescent excitons in layered nanomaterials. *Nature Nanotechnology*, 8:271 EP –, Mar 2013.

[100] Hiroshi Sekoguchi, Yasushi Takahashi, Takashi Asano, and Susumu Noda. Photonic crystal nanocavity with a q-factor of 9 million. *Opt. Express*, 22(1):916–924, Jan 2014.

[101] Kyle L. Seyler, John R. Schaibley, Pu Gong, Pasqual Rivera, Aaron M. Jones, Sanfeng Wu, Jiaqiang Yan, David G. Mandrus, Wang Yao, and Xiaodong Xu. Electrical control of second-harmonic generation in a wse2 monolayer transistor. *Nature Nanotechnology*, 10:407 EP –, Apr 2015.

[102] Abdul Shakoor, Roberto LoSavio, Paolo Cardile, Simone L. Portalupi, Dario Gerace, Karl Welna, Simona Boninelli, Giorgia Franz, Francesco Priolo, Thomas F. Krauss, Matteo Galli, and Liam O'Faolain. Room temperature all-silicon photonic crystal nanocavity light emitting diode at sub-bandgap wavelengths. *Laser & Photonics Reviews*, 7(1):114–121, 2013.

[103] Marin Soljacic, Elefterios Lidorikis, Mihai Ibanescu, Steven G. Johnson, J.D. Joannopoulos, and Yoel Fink. Optical bistability and cutoff solitons in photonic bandgap fibers. *Opt. Express*, 12(8):1518–1527, Apr 2004.

[104] R. Soref and J. Larenzo. All-silicon active and passive guided-wave components for lambda = 1.3 and 1.6 um. *Quantum Electronics, IEEE Journal of*, 22(6):873–879, 1986.

[105] Andrea Splendiani, Liang Sun, Yuanbo Zhang, Tianshu Li, Jonghwan Kim, Chi-Yung Chim, Giulia Galli, and Feng Wang. Emerging photoluminescence in monolayer mos2. *Nano Letters*, 10(4):1271–1275, 2010. PMID: 20229981.

[106] Brian Stern, Xingchen Ji, Avik Dutt, and Michal Lipson. Compact narrow-linewidth integrated laser based on a low-loss silicon nitride ring resonator. *Opt. Lett.*, 42(21):4541–4544, Nov 2017.

[107] M. S. Stern. Semivectorial polarised finite difference method for optical waveguides with arbitrary index profiles. *IEE Proceedings J - Optoelectronics*, 135(1):56–63, Feb 1988.

[108] N. Sultanova, S. Kasarova, and I. Nikolov. Dispersion Properties of Optical Polymers. *Acta Physica Polonica A*, 116:585, October 2009.

[109] Kazunori Takada, Hiroya Sakurai, Eiji Takayama-Muromachi, Fujio Izumi, Ruben A. Dilanian, and Takayoshi Sasaki. Superconductivity in two-dimensional coo2 layers. *Nature*, 422:53 EP –, Mar 2003.

[110] Fryett Taylor, Zhan Alan, and Majumdar Arka. *nanoph*, volume 7, chapter Cavity nonlinear optics with layered materials, page 355. Walter de Gruyter GmbH, 2019 2017. 2.

[111] Ming-Chun Tien, Jared F. Bauters, Martijn J. R. Heck, Daryl T. Spencer, Daniel J. Blumenthal, and John E. Bowers. Ultra-high quality factor planar si3n4 ring resonators on si substrates. *Opt. Express*, 19(14):13551–13556, Jul 2011.

[112] Rahul Trivedi, Uday K. Khankhoje, and Arka Majumdar. Cavity-enhanced second-order nonlinear photonic logic circuits. *Phys. Rev. Applied*, 5:054001, May 2016.

[113] J. Vuckovic, M. Loncar, H. Mabuchi, and A. Scherer. Optimization of the q factor in photonic crystal microcavities. *IEEE Journal of Quantum Electronics*, 38(7):850–856, July 2002.

[114] Xiangang Wan, Jinming Dong, Meichun Qian, and Weiyi Zhang. Nonlinear optical properties of perovskite $ymno_3$ studied by real-space recursion method. *Phys. Rev. B*, 61:10664–10669, Apr 2000.

[115] Cheng Wang, Zhaoyi Li, Myoung-Hwan Kim, Xiao Xiong, Xi-Feng Ren, Guang-Can Guo, Nanfang Yu, and Marko Loncar. Metasurface-assisted phase-matching-free second harmonic generation in lithium niobate waveguides. *Nature Communications*, 8(1):2098, 2017.

[116] Jing Wang, Hideo Mabuchi, and Xiao-Liang Qi. Calculation of divergent photon absorption in ultrathin films of a topological insulator. *Phys. Rev. B*, 88:195127, Nov 2013.

[117] L. Wang, I. Meric, P. Y. Huang, Q. Gao, Y. Gao, H. Tran, T. Taniguchi, K. Watanabe, L. M. Campos, D. A. Muller, J. Guo, P. Kim, J. Hone, K. L. Shepard, and C. R. Dean. One-dimensional electrical contact to a two-dimensional material. *Science*, 342(6158):614–617, 2013.

[118] Qing Hua Wang, Kourosh Kalantar-Zadeh, Andras Kis, Jonathan N. Coleman, and Michael S. Strano. Electronics and optoelectronics of two-dimensional transition metal dichalcogenides. *Nature Nanotechnology*, 7:699 EP –, Nov 2012. Review Article.

[119] Kenji Watanabe, Takashi Taniguchi, and Hisao Kanda. Direct-bandgap properties and evidence for ultraviolet lasing of hexagonal boron nitride single crystal. *Nature Materials*, 3:404 EP –, May 2004. Article.

[120] F. Withers, O. Del Pozo-Zamudio, A. Mishchenko, A. P. Rooney, A. Gholinia, K. Watanabe, T. Taniguchi, S. J. Haigh, A. K. Geim, A. I. Tartakovskii, and K. S. Novoselov. Light-emitting diodes by band-structure engineering in van der waals heterostructures. *Nature Materials*, 14:301 EP –, Feb 2015.

[121] Chi Xiong, Wolfram Pernice, Carsten Schuck, and Hong X. Tang. Second harmonic generation in aluminum nitride waveguides on silicon substrates. In *Conference on Lasers and Electro-Optics 2012*, page QF3G.4. Optical Society of America, 2012.

[122] Chi Xiong, Wolfram H. P. Pernice, and Hong X. Tang. Low-loss, silicon integrated, aluminum nitride photonic circuits and their use for electro-optic signal processing. *Nano Letters*, 12(7):3562–3568, 2012. PMID: 22663299.

[123] Eli Yablonovitch. Inhibited spontaneous emission in solid-state physics and electronics. *Phys. Rev. Lett.*, 58:2059–2062, May 1987.

[124] Frits Zernike and John Midwinter. *Applied Nonlinear Optics*. Dover Publications, 2006.

[125] Weijie Zhao, Zohreh Ghorannevis, Leiqiang Chu, Minglin Toh, Christian Kloc, Ping-Heng Tan, and Goki Eda. Evolution of electronic structure in atomically thin sheets of ws2 and wse2. *ACS Nano*, 7(1):791–797, Jan 2013.

[126] Zhaoming Zhu and Thomas G. Brown. Full-vectorial finite-difference analysis of microstructured optical fibers. *Opt. Express*, 10(17):853–864, Aug 2002.

Appendix A

ESTIMATION OF SHG POWER FROM A MONOLAYER

The power generated by a TMD monolayer can be approximated by [48]:

$$P_{av2} = \frac{32(NA)^2 t_2 P_{av1}^2 \phi (\chi^{(2)})^2}{\epsilon_0 c \lambda_2^4 R t_1^2 (n_2+1)^2 (n_1+1)^4} \tag{A.1}$$

where:

$$\phi = 8\pi \int_0^1 |cos^{-1}(\rho) - \rho\sqrt{1-\rho^2}|^2 \rho d\rho \tag{A.2}$$

Equation A.1 relates the average power at the second harmonic frequency (P_{av2}) to the average pump power at the fundamental frequency (P_{av1}). The pump beam is further parameterized by the repetition rate of the pump (R) and the pulse duration (t_1). The free space wavelength of the harmonic light (λ_2) also appears in the equation along with the permittivity of free space (ϵ_0) and the speed of light (c). The effects of the substrate are taken into account by the refractive index of the substrate (n_2) and the index of the material above the monolayer (n_1), which was air in our case. The numeric aperture (NA) of the objective also plays a role, as well as the sheet susceptibility of the monolayer ($\chi^{(2)}$).

Our experiments were conducted away from the excitonic wavelength range of WSe_2 due to the difficulty of coupling resonances to the emission in those wavelength ranges. The underlying principles for this effect is still a subject of investigation. Here we will discuss the experiments conducted on bare WSe_2 with a pump beam centered at 805 nm. From previous literature we know that the material has an ultra-high bulk susceptibility of 5 nm/V in this wavelength range [92]. This translates to a sheet susceptibility of 3.5×10^{-15} m^2/V. The monolayer was placed on a SiN substrate ($n_2 \approx 2$) without a cladding layer ($n_1 = 1$). The laser had a repetition rate of 80 MHz and a pulse duration of 2 ps. The pump beam was

focused down by a 40X Olympus Plan Achromat Objective with a numeric aperature of 0.65. This results in $P_{av2} = 16\ nW$.